

High-resolution, two-dimensional vertical tomography of the central Pacific mantle using ScS reverberations and frequency-dependent travel times

Rafael Katzman, Li Zhao, and Thomas H. Jordan

Department of Earth, Atmospheric, and Planetary Sciences, Massachusetts Institute of Technology, Cambridge

Abstract. A vertical tomogram is constructed for the mantle between Tonga and Hawaii. Using a complete Gaussian-Bayesian approach, we inverted a data set comprising 304 ScS reverberation travel times with Fréchet kernels computed by the paraxial ray approximation and 1122 frequency-dependent phase delays of turning and surface waves with Fréchet kernels calculated by a normal-mode coupling algorithm. The model parameters include shear speed variations, perturbations to shear wave radial anisotropy in the uppermost mantle, and the topographies of the 410- and 660-km discontinuities. Tests demonstrate that the data set resolves lateral structures in the upper mantle with scale lengths of several hundred kilometers and greater. The most significant feature in our model is a well resolved regular pattern of high and low shear velocities in the upper mantle. These variations have a horizontal wavelength of 1500 km, a vertical dimension of 700 km, and an amplitude of about 3%, and they show a strong positive correlation with seafloor topography and geoid height variations. The geoid highs correspond to a series of northwest trending swells associated with the major hotspots of the Society, Marquesas, and Hawaiian Islands. Where these swells cross the corridor, they are underlain by high shear velocities throughout the uppermost mantle, so it is unlikely that their topographies are supported by thermal buoyancy. Although chemical buoyancy generated by basaltic volcanism and the formation of its low-density peridotitic residuum can explain the positive correlation between topography and velocity variation at the shallow depth, an additional mechanism is needed to account for the shear velocity pattern at depths greater than 200 km. It is therefore hypothesized that the central Pacific is underlain by a system of Richter-type convective rolls that are oriented subparallel to the absolute plate velocity, have unit aspect ratio transverse to this orientation, and are confined above the 660-km discontinuity. This convection pattern appears to be strongly correlated with the locations of the Tahitian, Marquesan, and Hawaiian hotspots, which raises interesting questions for Morgan's hypothesis that these hotspots are the surface manifestations of deep mantle plumes.

1. Introduction

The three-dimensional (3-D) images of deep Earth structure provided by seismic tomography have placed strong constraints on models of mantle dynamics [Hager and Clayton, 1989; Forte et al., 1993; Phipps Morgan and Shearer, 1993; Puster and Jordan, 1997; van der Hilst et al., 1997]. These successes have motivated seismologists to improve tomographic techniques [Nolet, 1990; Li and Romanowicz, 1995; Marquering and Snieder, 1995] and to collect new data sets with enhanced spatial resolution [Su et al., 1994; Zielhuis and Nolet, 1994; Grand et al., 1997; van der Hilst et al., 1997]. Attempts to resolve more of the details of the Earth's interior with better precision encounter several problems, however. The first is parameterization. Seismic wave propagation can be described to zeroth order by a spherically symmetric Earth model $m_0(r)$, such as the preliminary reference Earth model (PREM) of Dziewonski and Anderson [1981], plus a small aspherical perturbation $\delta m(r, \theta, \varphi)$. In most tomographic studies, the aspherical part

is restricted to only one, or at most a few, model parameters, such as the compressional wave speed perturbation $\delta\alpha$ or the shear wave speed perturbation $\delta\beta$. The details of wave propagation can depend on other effects, of course, such as lateral heterogeneity of upper mantle anisotropy [Forsyth, 1975; Tanimoto and Anderson, 1985; Nishimura and Forsyth, 1989; Montagner and Tanimoto, 1991; Silver, 1996] and the topography of the major transition zone discontinuities [Revenaugh and Jordan, 1989, 1991b; Shearer, 1991, 1993; Flanagan and Shearer, 1998]. Therefore attempts to improve the tomographic imaging of interior structure may require expanding the model parameterization.

A second problem concerns the way in which the measurements of seismic data are made. Seismograms, especially the broadband records from modern, high-performance instruments, encode an immense amount of information about the Earth, and seismologists have developed a diverse ensemble of techniques for extracting this information in the form of travel times, phase and group velocities, waveforms, decay rates, eigenfrequencies, splitting parameters, etc. Tomographic imaging is often sharpened if the data for a particular inversion come from measurement methods that are as uniform as possible, or at least mutually consistent. This can be challenging for studies directed at an

Copyright 1998 by the American Geophysical Union

Paper number 98JB00504.
0148-0227/98/98JB-00504\$09.00

assortment of wave types recorded on more than one component of ground motion.

A third and related problem is how the data are connected back to the Earth. In tomography, a datum is considered to be the value of some functional of an Earth model plus an error arising from ambient and signal-generated noise. The construction of the functional relationship, which is generally nonlinear, requires a wave propagation theory, and feasible algorithms always require some degree of theoretical approximation. Travel times of body phases like P and S are typically interpreted using geometrical optics where the influence of Earth structure is localized along the geometrical ray. This is adequate for high-frequency waves, but it begins to fail in high-resolution studies of heterogeneities having length scales comparable to the Fresnel scale of the waves [Nolet *et al.*, 1994; Vasco *et al.*, 1995]. In the case of intermediate-frequency body waves such as SS at 30 millihertz (mHz), the first Fresnel zone can have dimensions of hundreds of kilometers [Shearer, 1993, Figure 24], and proper interpretation requires an explicit consideration of the band-limited nature of the signals. The problem is particularly tough for body waves with P - SV polarizations, where the coupling among various phases is often strong and difficult to handle with ray theoretic methods. Similarly, the classical mode theoretic methods for the interpretation of the low-frequency, dispersed surface waves and their overtones commonly make approximations that may be inadequate for high-resolution studies (e.g., the mode group is isolated from other modes; it averages structure uniformly along its path).

The measurement and interpretation techniques introduced in this paper have been specifically designed to address these issues. The framework for the methodology is the theory of generalized seismological data functionals (GSDF) presented by Gee and Jordan [1992], which casts seismic information in terms of spectral parameters describing the deviation of an observed waveform from one obtained with a reference Earth model \mathbf{m}_0 . The synthetic waveform is called an isolation filter, and the measurement procedure involves the windowing and narrow-band filtering of its cross correlation with the data. It yields four bias-corrected GSDF parameters, and one of these, loosely referred to here as the "frequency-dependent travel time residual" and denoted by $\delta\tau(\omega)$, is especially suitable for tomographic work. The theory specifies the linearized functional relationships, i.e., the Fréchet kernel [Backus and Gilbert, 1967], between $\delta\tau(\omega)$ and the model perturbation $\delta\mathbf{m}$ for arbitrary isolation filters, including complex waveforms comprising many rays or mode branches.

The power of this technique lies in its generality: the same analysis code can be applied to body waves, surface waves, and complex interference packets (e.g., oceanic G_1 groups, Sa and shear-coupled PL phases, triplicated arrivals) on all three components of ground motion, and in the precision with which it automatically characterizes the model-data functional relationship, accounting for both the band-limited nature of the signals and the interferences among the various wave constituents. Previous applications of the GSDF technique [Gaherty and Jordan, 1995; Gaherty *et al.*, 1996; M. Kato and T.H. Jordan, Seismic structure of the upper mantle beneath the western Philippine Sea, submitted to *Physics of the Earth and Planetary Interiors*, 1997, hereinafter cited as Kato and Jordan, submitted manuscript, 1997] have been based on a path-averaged, 1-D approximation, but in this work we have used an extension developed by Zhao and Jordan [1998] that calculates

2-D Fréchet kernels for $\delta\tau(\omega)$ by mode-coupling theory [Woodhouse, 1980, 1983; Li and Tanimoto, 1993]. The mode-coupling scheme in this implementation is made computationally efficient by taking advantage of the modal structure used in the synthesis of the isolation filter.

The GSDF technique provides a uniform methodology for measuring frequency-dependent travel times for all of the interesting wave groups in the direct-phase interval; i.e., that part of the seismogram extending from the P wave to the surface waves. In this study, which is focused on the shear velocity structure of the Tonga-Hawaii corridor ($\Delta = 39^\circ$ - 57°), we have analyzed only the shear-dominated wave groups beginning with the direct S phase and including sS , SS , sSS , SSS , Sa , R_1 , and G_1 , recovering their phase delays in the band 10-45 mHz (section 4). The waveforms in this interval have been a principal data source for much previous work, including a number of tomographic studies on both global [e.g., Woodhouse and Dziewonski, 1984; Su *et al.*, 1994; Masters *et al.*, 1996; Li and Romanowicz, 1996] and regional scales [e.g., Grand, 1987, 1994; Zielhuis and Nolet, 1994; Marquering *et al.*, 1996; Zielhuis and van der Hilst, 1996; van der Lee and Nolet, 1997], and our analysis confirms the efficacy of this type of data in delineating upper mantle structure.

We have supplemented the frequency-dependent travel times with an extensive set of observations from a largely untapped source, the ScS reverberations, which arrive in a richly structured interval of the seismogram following the surface waves and preceding the long-arc arrivals. Multiply-reflected ScS_n phases (where n is the core reflection number) have been extensively used to investigate mantle attenuation [Jordan and Sipkin, 1977; Nakanishi, 1979; Sipkin and Jordan, 1980b; Lay and Wallace, 1983] and in some reconnaissance studies of mantle heterogeneity [Sipkin and Jordan, 1976, 1980a], but they have not been thus far employed in mantle tomography. The primary ScS_n and $sScS_n$ phases lie in a sea of higher-order reverberations generated by their interactions with mantle discontinuities, and synthetics-based migration methods have been developed to stack these data and obtain path-averaged reflectivity profiles for the entire mantle [Revenaugh and Jordan, 1989, 1991b]. Some of the first-order reflections from the transition zone discontinuities are large and isolated enough for their travel times to be measured as individual phases, however [Revenaugh and Jordan, 1987]. As discussed in section 3, we have used ray theoretical isolation filters to obtain differential reflection times from both topsides and bottomsides of the 410- and 660-km discontinuities (hereinafter referred to as the 410 and 660 discontinuities, respectively). These times have been measured at a center frequency of 25 mHz; hence, they sample the mantle over a broad zone transverse to their ray paths, and their interpretation cannot be based on geometrical optics. We have instead constructed "fat ray" Fréchet kernels using a paraxial ray approximation, which we have validated by comparing them with kernels computed by coupled-mode summation.

For corridors like Tonga-Hawaii with good sources at appropriate distances, a large number of data, up to 60 ScS reverberation times and frequency-dependent times of surface and turning waves, can be extracted from a single, three-component seismogram, and the multiplicity of wave paths is sufficient to construct a high-resolution vertical tomogram in the plane of the corridor [Katzman *et al.*, 1997]. This type of image construction differs from most mantle tomography, in

which the horizontal resolution is obtained primarily from wave paths crossing on differing great circles. In addition to shear velocity perturbations, the model includes lateral variations of upper mantle anisotropy and the topographies of the 410 and 660 discontinuities. The topographic parameters are constrained by a combination of first-order ScS reverberations and the dispersion of shear-dominated waves that turn in the transition zone. The restriction of this study to a single corridor precludes the recovery of the azimuthal dependence of anisotropy [Montagner and Tanimoto, 1991; Silver, 1996], but the dependence of the phase delays on polarization provides good constraints on the lateral and radial differences between the apparent SH and SV velocities, $\beta_H - \beta_V$.

In section 5, we invert the Tonga-Hawaii data for an image of the vertical plane of the corridor. The resulting tomogram, TH2, differs only in details from a preliminary version (TH1) presented by Katzman *et al.* [1997]. The model accounts for most of the variance in the travel time residuals but, like any other seismological inversion, is nonunique. We have therefore attempted to substantiate the main features of the model by a combination of data-based inversion, numerical tests, and resolving-power calculations, which are summarized in section 5 and Appendices A and B. The tomogram reveals an intriguing pattern of shear speed highs and lows that are well resolved by the data and appear to reflect small-scale convective processes in the central Pacific upper mantle. The geodynamic implications of these results are discussed in section 6.

2. Heterogeneity in Tonga-Hawaii Corridor

The corridor between the Tonga-Kermadec subduction zone and the Global Seismic Network (GSN) stations KIP and HON on the island of Oahu, Hawaii, was chosen for several reasons. It traverses the central Pacific Ocean nearly perpendicular to the plate motion across a series of island chains and ocean plateaus in a region of nearly uniform (100-125Ma) crustal age (Figure 1). The intense seismicity of the Tonga arc provides a dense array of large earthquakes extending to depths exceeding 600 km that write beautiful seismograms at Oahu, with high-amplitude direct phases and well-excited ScS reverberations. The quality of these records has made this corridor a target for many previous studies [Jordan and Sipkin, 1977; Sipkin and Jordan, 1979; Revenaugh and Jordan, 1987], and much is known about its radial structure. In particular, Gaherty *et al.* [1996] have recently inverted the reflectivity results of Revenaugh and Jordan [1991a,b,c] together with a large set of frequency-dependent travel times from GSDF analysis for a radially anisotropic, 1-D model, PA5 (Figure 2).

PA5 is notable because all of its discontinuities are confined by measurements of shear wave reflection travel times and impedance contrasts, and the gradients between discontinuities are constrained by turning-wave data. Its features include a shallow G discontinuity (lid/low-velocity zone boundary) at 68 km; shear anisotropy of 2-3% extending to 166 km, where the average shear speed reaches its minimum value of $4.26 \text{ km}\cdot\text{s}^{-1}$; a steep gradient to the discontinuity at 415 km; a small discontinuity at 507 km; and a large upper

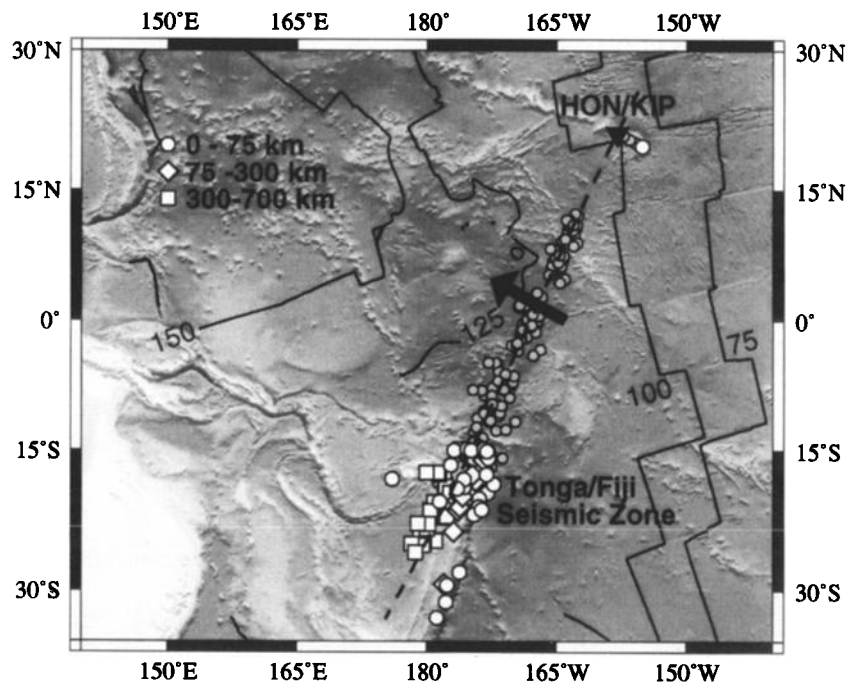


Figure 1. Mercator projection of the central Pacific showing the study corridor from the Tonga-Fiji seismic zone to the stations HON and KIP on Oahu, Hawaii (solid triangle). The axis of the corridor (dashed line) samples a uniform old ocean basin with seafloor age ranging from 100 to 125 Ma (isochrons, marked by solid contours, are taken from Mueller *et al.* [1993]) and is roughly perpendicular to the current plate motion relative to the hotspot reference frame (solid arrow, from Gripp and Gordon [1990]). Epicenters of the 77 Tonga-Fiji events and one Hawaiian event used in this study are shown as open symbols (circles, shallow focus; diamonds, intermediate focus; squares, deep focus). Shaded circles are surface bounce points of ScS_n phases (core reflection numbers $n = 2-4$) from 28 events. Bathymetric variations are shown by illuminated gray shading in the map.

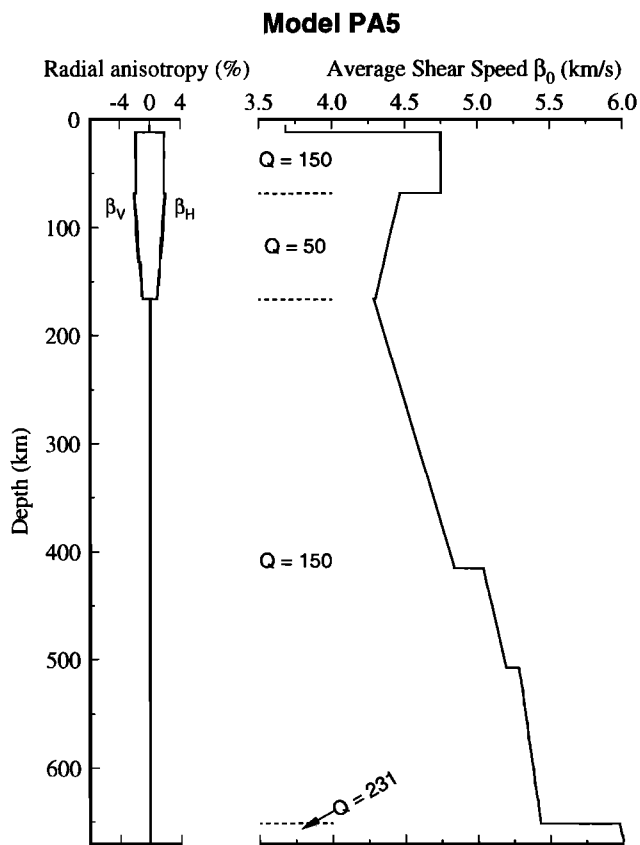


Figure 2. The shear wave structure and the Q structure of model PA5, our reference model for the upper mantle. Mean shear wave speeds and quality factors are plotted on the right, and the anisotropic velocity perturbations relative to these mean velocities are plotted on the left. Below 800 km the model is the same as PREM at a reference frequency of 35 mHz, with a quality factor of $Q_{LM} = 231$. PA5 is a path-average, radially anisotropic model that was obtained for the Tonga-Hawaii corridor by *Gaherty et al.* [1996]. It is based on a joint inversion of frequency-dependent travel times of surface and turning waves (such as R_1 , G_1 , SSS , sSS , SS , and S) together with travel times and impedance contrasts for mantle discontinuities, obtained from the ScS reverberation study of *Revenaugh and Jordan* [1991a,b,c]. The inversion included mineralogical constraints for density and bulk sound velocity.

mantle discontinuity at 651 km (see J.B. Gaherty et al., Seismic structure of the upper mantle: A regional comparison of seismic layering, submitted to *Physics of the Earth and Planetary Interiors*, 1997, hereinafter cited as Gaherty et al., submitted manuscript, 1997, for comparisons with other regions and a discussion of the structural implications). Because it is based on the (nonlinear) inversion of the same types of data considered here, PA5 is the ideal upper mantle reference model for our tomographic inversions.

The most compelling motivation for the study of this particular region is the prima facie evidence for along-path heterogeneity observed in the $ScS_n - ScS_m$ differential travel times (Figure 3). Their residuals relative to the PA5/PREM reference model are very large and systematic, with a range of about 8 s, and cannot be explained by near-source or near-receiver structure. This high, along-path variability was first observed by *Sipkin and Jordan* [1980a], who speculated that it might be diagnostic of small-scale, upper mantle convection rolls oriented by plate motion, as proposed by *Richter* [1973]

and *Richter and Parsons* [1975]. *Gee and Romanowicz* [1992] collected more data that revealed the strong, nearly linear gradients of the residuals with epicentral distance evident in Figure 3, and they also argued that these data require significant along-path structure, presumably in the upper mantle. The magnitude of variation in two-way travel time in this part of the Pacific is almost as large as, for example, the $ScS_2 - ScS$ differences observed across the major tectonic transition from the Tertiary Arctic Ocean basin to the Precambrian Siberian craton [cf. *Sipkin and Jordan*, 1976, Figure 14]. Hence despite its apparent tectonic uniformity, the central Pacific mantle is strongly heterogeneous.

Because they used only vertically propagating ScS_n waves, neither of the earlier studies by *Sipkin and Jordan* [1980a] and *Gee and Romanowicz* [1992] was able to demonstrate conclusively that the locus of the heterogeneity was in the upper mantle. Global tomographic models, as well as higher-resolution regional studies of the Pacific upper mantle [*Zhang and Tanimoto*, 1989], have thus far revealed no indications of structural variations in the upper mantle with the magnitude and scale needed to explain the data in Figure 3. Evidence has also accumulated for significant heterogeneity in the D" layer at the base of the mantle beneath this region [*Dziewonski et al.*, 1996; *Garnero and Helmberger*, 1996; *Wyssession*, 1996], raising the possibility of a deep mantle origin. Based on our preliminary work, however, it appears that the residuals in Figure 3 are an expression of small-scale (~1500-km wavelength) heterogeneities several percent in amplitude located within the upper mantle and transition zone [*Katzman et al.*, 1997]. We document this conclusion in this paper using an expanded data set and a more detailed exposition of the analysis techniques and inversion results.

3. ScS Reverberation Travel Times

At the epicentral distances in this corridor, the reverberative interval is populated by the primary ScS_n and $sScS_n$ phases with core reflection numbers n ranging from 2 to 4 and a series of reflections and multiple reflections from internal mantle discontinuities (Figure 4a). The waves that reflect only once from an internal discontinuity are called first-order reverberations [*Revenaugh and Jordan*, 1987]; in a spherically symmetric structure, they occur in dynamic families [*Hron*, 1971, 1972] that arrive with the same amplitude at the same time to form discrete phases which are significantly larger (by a factor of n or $n+1$) than the individual reflections. We denote such an arrival by the phase symbols $ScS_n^{d\pm}$ or $sScS_n^{d\pm}$, where n is the number of core reflections of the parent ScS or $sScS$, d is the nominal discontinuity depth and \pm indicates topside or bottomside reflections, respectively. The ray paths for the dynamic families $ScS_2^{660\pm}$ and $sScS_2^{660\pm}$ are illustrated in Figure 4b.

3.1. Synthetic Seismograms, Isolation Filters, and Fréchet Kernels

In a spherically symmetric Earth, ScS reverberations do not experience critical phenomena such as turning points and caustics, and diffractions are unimportant; hence geometrical ray theory is usually adequate for computing synthetic seismograms [*Revenaugh and Jordan*, 1987]. This expectation can be confirmed by comparing ray theoretical synthetics for the reverberative interval with those computed by complete

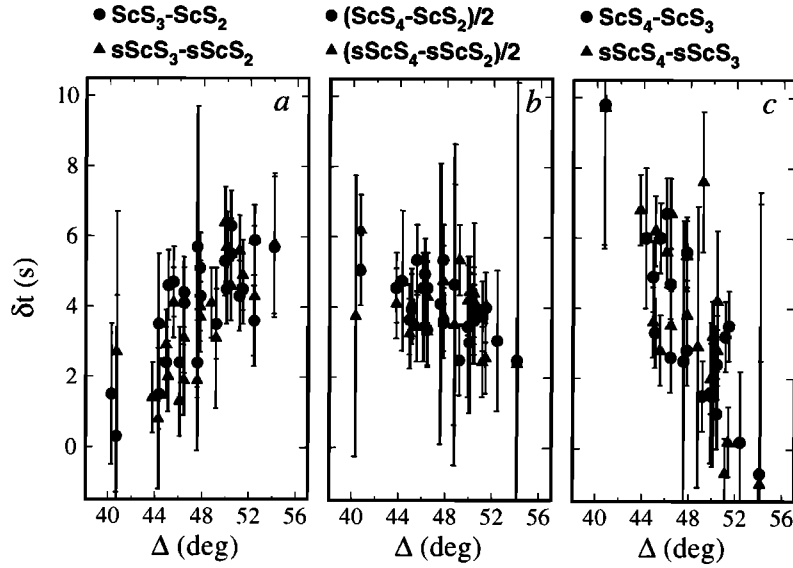


Figure 3. Plots of $ScS_n - ScS_m$ observed travel time residuals relative to the PA5/PREM reference model. The $ScS_4 - ScS_2$ residuals in the middle have been divided by two to normalize them to a two-way time. The positive offset of the data indicates a generally slow lower mantle in this region of the Pacific [Su *et al.*, 1994; Masters *et al.*, 1996]. However, the large variation of differential times from individual events [Sipkin and Jordan, 1980a] and the systematic variation with distance [Gee and Romanowicz, 1992] cannot be explained by a spherically symmetric Earth model or by changing the source location and/or origin time.

mode summation (Figure 4a). Since the former were summed only over the zeroth- and first-order reverberations, the good agreement also demonstrates that the second- and higher-order reverberations from the transition zone can be safely ignored (see Revenaugh and Jordan [1987] for comparisons with ray theoretic seismograms computed to second order).

We have adopted this first-order approximation throughout our analysis, except that all reverberations within the crust were included for every phase via a Haskell propagator. For each data record, a complete synthetic seismogram was calculated for the PA5/PREM reference model by summing over the zeroth-order phases and the first-order reverberations from the G, 410, and 660 discontinuities. All rays that contribute to the reverberative interval at these epicentral distances have nearly vertical paths through the uppermost mantle, so that in a radially anisotropic (transversely isotropic) Earth model like PA5, the appropriate shear wave speed is β_V . Prior to summation, the travel time along each ray path was corrected for ellipticity and bounce point bathymetry; the latter was obtained by an appropriate spatial averaging of DBDB5 bathymetric model. Dynamic families were then summed, each pulse was causally attenuated assuming the Q structure of PA5/PREM (Figure 2) to be frequency independent, and the resulting record was convolved with the instrument response.

The isolation filters used in the measurement of the differential phase delays $\delta\tau(\omega)$ were constructed by summing only the contributions for the target wave group, which was either a single phase or a group of nearly coincident arrivals (see below). We disregarded the differential dispersion within a given arrival (which should be small for reflections from sharp discontinuities) and recovered the phase delays at a single center frequency $f = \omega/2\pi \approx 25$ mHz. To first order, the relationship between $\delta\tau$ and the relative perturbation to the vertical shear velocity $\delta\beta_V/(\beta_V)_0$ in the ray plane (r, θ) can be written as

$$\delta\tau(\omega) = \int_{r_c}^R \int_0^\pi K_{\beta_V}(\omega, r, \theta) \frac{\delta\beta_V(r, \theta)}{[\beta_V(r)]_0} d\theta r dr + \sum_{i=1}^M \int_0^\pi K_i(\omega, \theta) \delta r_i(\theta) d\theta. \quad (1)$$

In this expression, r_c is the core radius, R is the Earth radius, $[\beta_V(r)]_0$ is the vertical shear velocity in the reference model, $K_{\beta_V}(\omega, r, \theta)$ is the Fréchet kernel for the areal relative perturbation $\delta\beta_V(r, \theta)/[\beta_V(r)]_0$, and $K_i(\omega, \theta)$ is the kernel for the along-path topography $\delta r_i(\theta)$ of the i th discontinuity at reference radius r_{0i} . The Fréchet kernel for an isolation filter comprising N undispersed, narrowband wavelets with model-predicted amplitudes $\{a_j\}$ and travel times $\{\tau_j\}$ is the weighted sum of the kernels for the individual wavelets; e.g.,

$$K_{\beta_V} = \sum_{j=1}^N c_j K_{\beta_V}^{(j)}. \quad (2)$$

Expressions for the coefficients $\{c_j\}$ can be derived from the general perturbation equations given by Gee and Jordan [1992, section 4.7]; the results are

$$c_j = \frac{a_j}{C} \sum_{k=1}^N a_k \exp[-\sigma^2(\tau_k - \tau_j)^2/2] \cos[\omega(\tau_k - \tau_j)], \quad (3)$$

where σ is the half-bandwidth and C is a normalization constant given by

$$C = \sum_{j=1}^N \sum_{k=1}^N a_j a_k \exp[-\sigma^2(\tau_k - \tau_j)^2/2] \cos[\omega(\tau_k - \tau_j)]. \quad (4)$$

The content of (2)-(4) can be elucidated by considering some special cases. For members of a dynamic ray family, a_j and τ_j are constants for all j , and c_j reduces to $1/N$. In the case of N phases with identical travel times, the kernels are just weighted by their amplitudes,

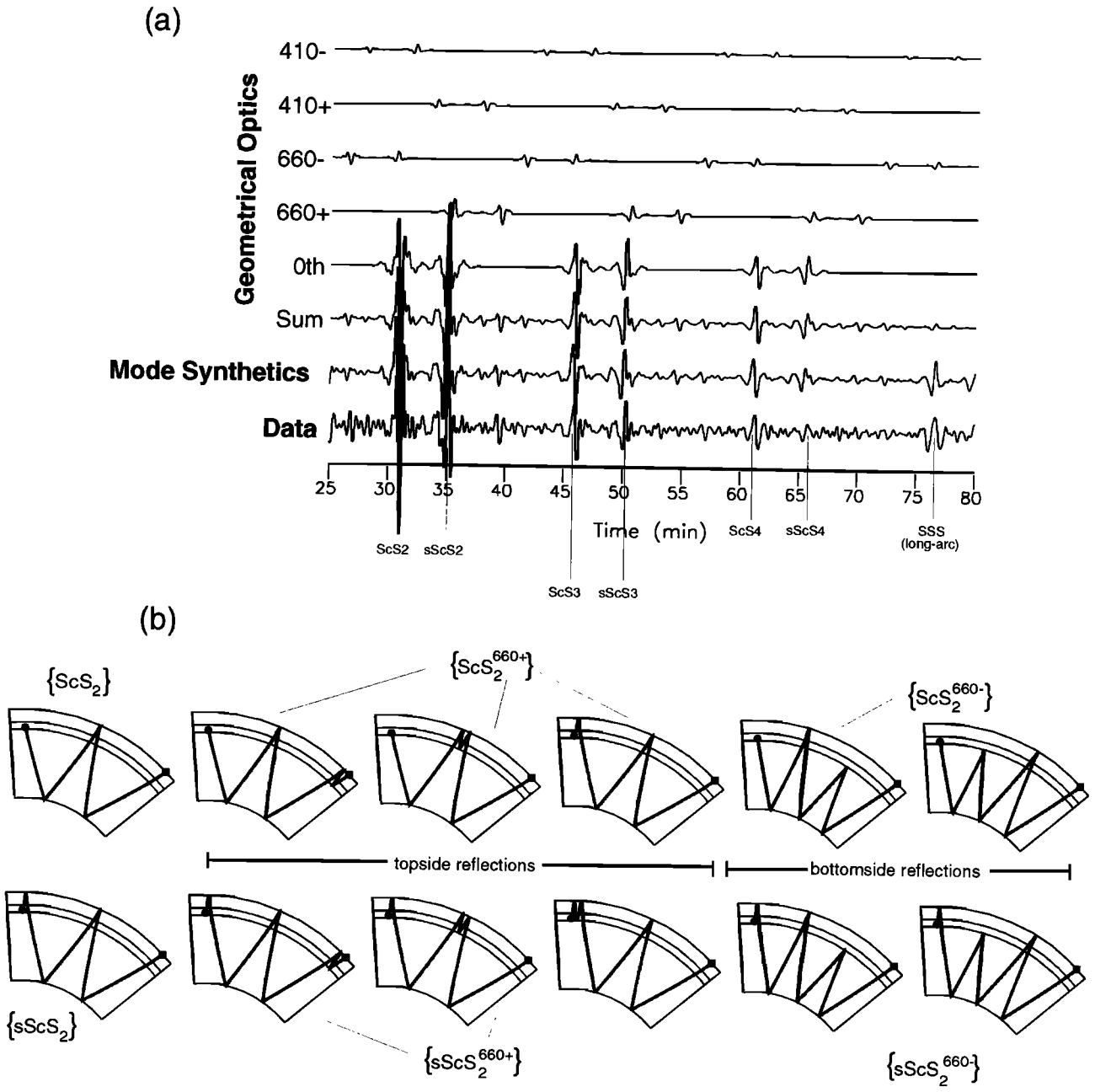


Figure 4. (a) An example of the reverberative interval for a deep-focus earthquake ($h = 590$ km, $\Delta = 46.4^\circ$). Bottom two traces are the data and the complete synthetic seismogram generated by normal-mode summation; others are synthetics computed by geometrical optics (an excellent approximation for the reverberative interval), with a Haskell propagator for crustal reverberations. Trace labeled 0th comprises the zeroth-order ScS_n and $sScS_n$ phases (classified by their CMB reflection number n); those labeled 410⁻, 410⁺, 660⁻, 660⁺ are the first-order bottomside and topside reflections from the 410-km and 660-km discontinuities, respectively. Time is minutes after the origin time. (b) The ray paths for the $n = 2$ zeroth-order and first-order reverberations from the 660-km discontinuity. The topside and bottomside reflections in each row constitute a dynamic family of rays with the same amplitude and phase that constructively interfere to form the first-order arrivals seen on the seismograms. The families of first-order reverberations are denoted by $ScS_n^{d\pm}$, where n is the number of core reflections of the parent ScS_n or $sScS_n$, d is the discontinuity depth, and \pm indicates a topside/bottomside reflection.

$$c_j = a_j / \sum_{k=1}^N a_k.$$

$$c_j = a_j^2 / \sum_{k=1}^N a_k^2.$$

When the separation in travel time is large compared to σ^{-1} , the coupling terms in (3) are small, and the weighting is proportional to the squared amplitude,

In general, the coupling can be either positive or negative, depending on the sign of $\cos[\omega(\tau_k - \tau_j)]$. For dispersed signals, such as those considered in section 4, equations (3)

and (4) must be generalized to include other parameters, such as the group delay and the rate of change of the logarithmic amplitude with frequency [Gee and Jordan, 1992].

According to the geometrical optics approximation usually employed in seismic tomography, the kernels $K_{\beta\nu}^{(j)}$ are concentrated in δ functions along the ray paths. The propagation distances L for the ScS reverberations are very large, however, reaching 25,000 km for ScS_4 , and their wavelengths λ at 25 mHz are ~ 200 km; hence the radius of the first Fresnel zone, $r_F \approx \sqrt{\lambda L}/2$, can exceed 1000 km. We have therefore calculated a "fat ray" Fréchet kernel by distributing the geometrical optics sensitivity of $-\beta\nu^{-1}$ per unit path length around the ray, weighted by a cosine bell of radius $r_F/2$. To account for ray curvature, we computed the first Fresnel zone by the paraxial ray approximation [Červeny and Soares, 1992]. Plates 1a and 1b compare the Fréchet kernel for ScS_2 derived by this ad hoc method with one calculated by the formal mode-coupling scheme of Zhao and Jordan [1998]. The kernels from these two very different theories are similar, although the mode-based kernel is more diffuse near the source and receiver, where the paraxial approximation is known to fail.

One advantage of the fat ray kernel over the mode kernel is its computational efficiency, requiring orders of magnitude less computer time than the heavy calculations needed for the coupled mode summation. A second is that it can be separated into a component for each reflection in a dynamic family, which can then be individually corrected for ellipticity and seafloor topography, as discussed above. We used the fat ray kernels to make these corrections and in all inversions.

3.2. Sampling Properties

The tomographic power of the ScS reverberations derives from their multiplicity. Because of their nearly vertical ray paths, the times of the zeroth-order reflections are essentially insensitive to radial variations other than the mantle average, but they sample along-path heterogeneity in unique ways. For example, their surface reflection points are distributed such that the $ScS_3 - ScS_2$ and $ScS_4 - ScS_3$ differential times are particularly sensitive to lateral variations in the upper mantle near the center of the path having horizontal wavelengths of about one-third of the epicentral distance (Plates 1c and 1d). Therefore, if the heterogeneity responsible for the large residuals in Figure 3 resides in the upper mantle, we expect it to contain significant power at wavelengths near $\Delta/3 \approx 15^\circ$. As we shall see, this is indeed the case.

The first-order reverberations from transition zone discontinuities do depend on the vertical structure; for example, times of the topside reflections from 660 are more sensitive to upper mantle shear speeds and the bottomside reflections are more sensitive to lower mantle speeds, owing to the extra peg-leg reflections in these two regions, respectively. Because the travel time observations average over the dynamic family of reflected rays, this differential sensitivity is distributed uniformly with respect to the reflection points, and we cannot take advantage of the lateral differences among members of the same family. (Such differences give rise to a splitting of the reverberation multiplet, however; assuming the 660 to be sharp, *Revenaugh and Jordan* [1989, 1991b] used frequency-dependent observations of the multiplet broadening to constrain its root-mean-square topography at the sampling wavelength.

obtaining an estimate of 5-10 km for the central and western Pacific, which was consistent with their observations of interpath topography and the results presented in section 5.4).

As expected, the first-order reverberations are also much more sensitive to the locations of the reflecting discontinuity than the parent zeroth-order phase (Plates 1e and 1f). Since the sign of this sensitivity is opposite for the topside and bottomside reflections, their combination can be used to separate volumetric heterogeneity from discontinuity topography. For example, a topographic depression on a discontinuity will cause a time delay for the topside reverberations and a time advance for the bottomside reverberations, while a velocity perturbation situated either above or below the discontinuity will affect the travel time of only one of these phases.

3.3. Data for the Tonga-Hawaii Corridor

We measured the travel times of zeroth- and first-order reverberations on transverse component seismograms from 27 earthquakes in the Tonga-Fiji seismic zone recorded at KIP or HON during the period 1973-1993 and one shallow-focus Hawaii earthquake (April 26, 1973) recorded at KIP (Figure 1). The Tonga-Fiji events were moderate in magnitude ($5.7 \leq M_w \leq 7.2$) with hypocentral depths ranging from 48 to 614 km and epicentral distances of 40° to 54° . For the older events (1973-1976), the focal mechanisms were taken from *Richter* [1979] and *Butler* [1982]; all the subsequent events had well-determined CMT solutions in the Harvard catalog. The horizontal components with a 1-s sampling interval were rotated, and the transverse components were prewhitened with a damped least squares deconvolution algorithm and zero-phase filtered around a center frequency of 25 mHz. We kept only the records with a good signal-to-noise ratio (snr) that showed well-excited reverberation phases from the 410 and/or 660 discontinuities.

The overlap among the phases within the reverberative interval depends strongly on source depth, which must be taken into account when constructing the isolation filters. At intermediate focal depths, for example, the topside reflections ScS_n^{660+} and ScS_n^{410+} arrive at nearly the same time, as do the corresponding bottomside reflections (Figure 5a). In such cases, we summed the contributions from both dynamic families to obtain a single isolation filter (Figure 5b). This example shows that two first-order arrivals, ScS_n^{410+} and $sScS_n^{410-}$, fall within the side lobes of the primary $sScS_n$ and ScS_{n+1} phases, respectively. Since their times could not be measured without large interference corrections, we removed them from the data set. For deep-focus events, the same problem arises for ScS_n^{660+} and $sScS_n^{660-}$ (Figure 6), and their times were also deleted. Nevertheless, up to 6 zeroth-order and 12 first-order reverberation times could be measured from the single record of a deep-focus event.

The concatenation of two or more reverberation phases was used to increase the snr even in cases where the individual phases were well isolated, especially for earthquakes with shallower focal depths where near-surface reverberations caused high noise levels. (Events above 70 km were always too noisy to measure first-order reverberations.) To retain sensitivity to discontinuity topographies, only topside or bottomside reflections were combined in this manner, e.g., groupings such as $\{sScS_n^{410+} + ScS_n^{660+} + sScS_n^{660+}\}$ and $\{ScS_n^{410-} + sScS_n^{410-} + ScS_n^{660-}\}$. Our procedure was to cross-

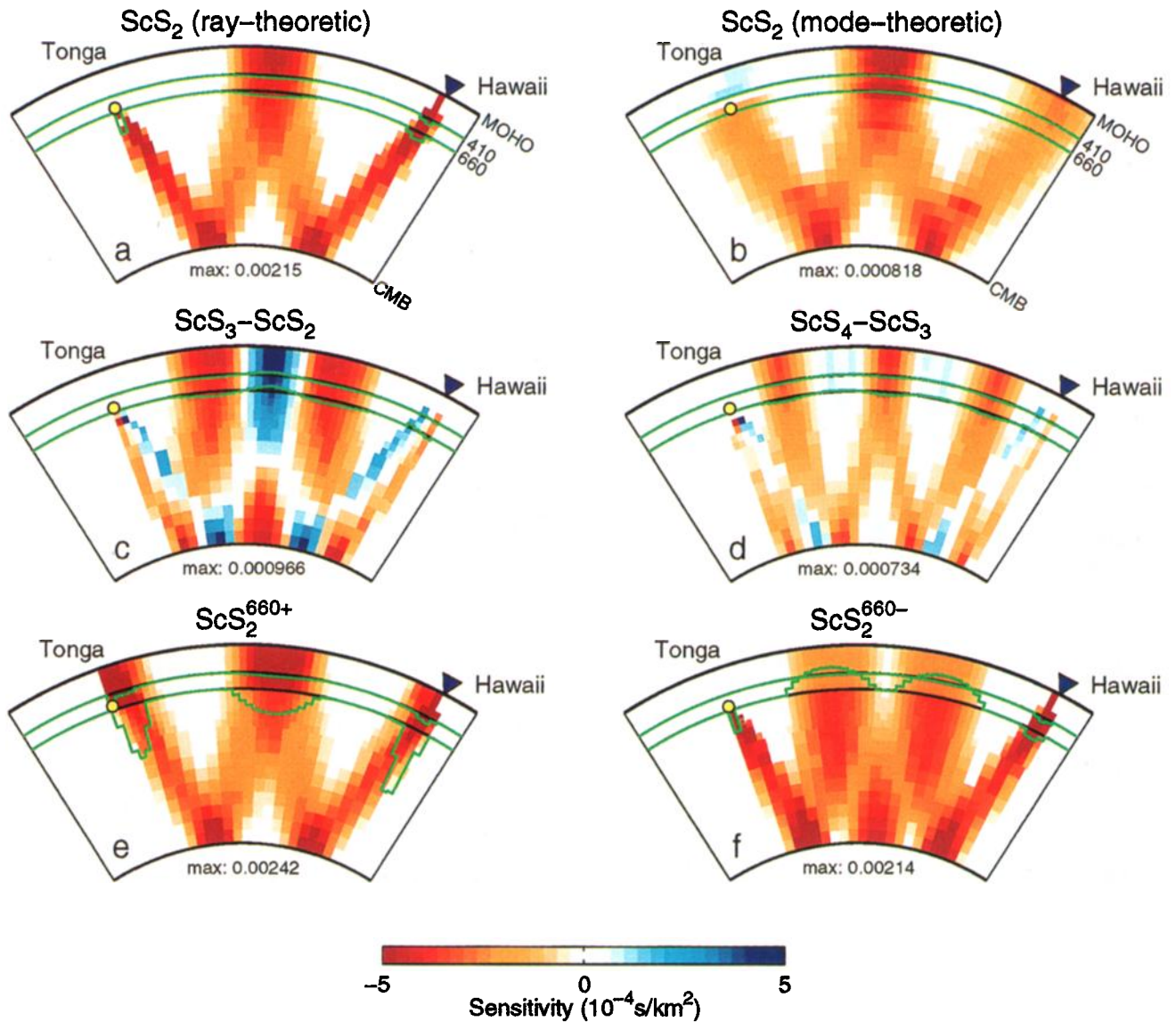


Plate 1. Examples of the Fréchet kernels for ScS reverberations. The wave type is indicated at the top of each panel. Warm colors correspond to negative sensitivity (phase delay increase for velocity decrease), cool colors correspond to positive sensitivity, and the green lines show the sensitivity to perturbations in the radii of 410 and 660 discontinuities; yellow circles and blue triangles show the locations of the source and receiver, respectively. All kernels except for the one in Plate 1b are fat ray kernels, which were calculated using the paraxial-ray approximation (see text). (a) and (b) Comparison between a fat ray kernel and a mode theoretic kernel for ScS_2 . The latter was calculated by the mode-coupling scheme of *Zhao and Jordan* [1998], which is employed later in the paper for calculating the kernels for the turning and surface wave data. Despite the very different theories, the resulting kernels are quite similar except near the source and the receiver, where the paraxial-ray approximation breaks down. (c) and (d) Differential kernels for $ScS_3 - ScS_2$ and for $ScS_4 - ScS_3$. (e) and (f) First-order-reverberation kernels for ScS_2^{660+} (topside reverberation) and ScS_2^{660-} (bottomside reverberation).

correlate a series of single-phase and concatenated isolation filters with the observed seismogram, to maximize the cross correlogram (resampled at 0.1 s) to obtain the phase delay, and to correct the time for interference with other phases by subtracting the phase delay computed for a complete synthetic seismogram. Each resulting time was then graded according to the snr and magnitude of the interference corrections, and low-scoring measurements were discarded. The final step was to remove redundant measurements from the data set. If good times were obtained for both ScS_n^{410-} and $sScS_n^{660-}$, for

example, then the phase delay for the concatenated filter $\{ScS_n^{410-} + sScS_n^{660-}\}$ was dropped.

Table 1 displays the distribution of the 304 reverberation times obtained in this study, classified according to source depth, core reflection number, and the concatenation scheme used in constructing the isolation filters. With the exception of the Hawaiian event, this data set is identical to that used in our preliminary study [Katzman *et al.*, 1997]. When normalized to a two-way lower mantle path, the Tonga-Hawaii times have an average delay relative to the PA5/PREM

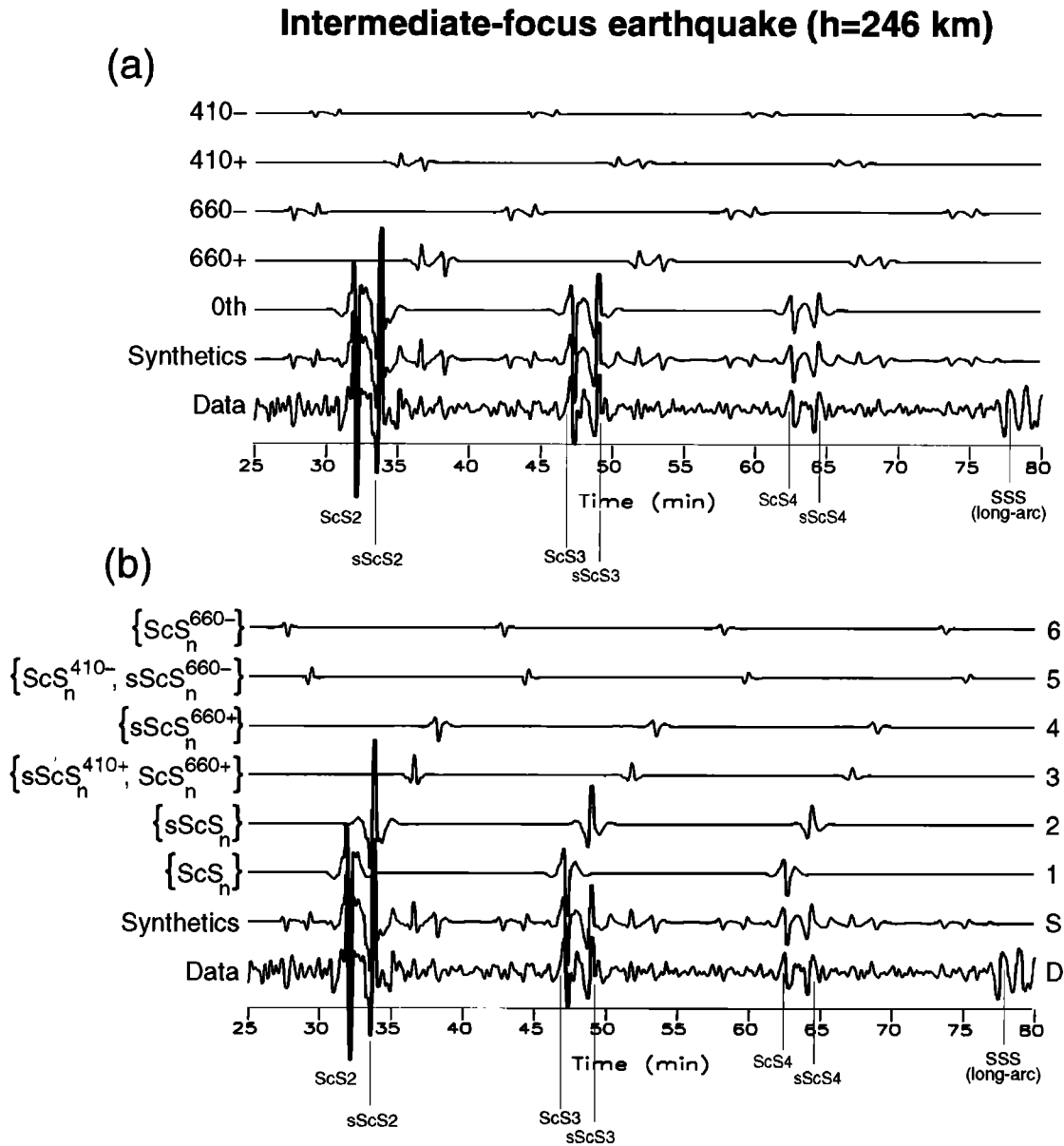


Figure 5. Decomposition of a reverberative interval for an intermediate-focus earthquake ($h = 246$ km, $\Delta = 45.5^\circ$). (a) For reference, the data and the synthetics (bottom two traces) are shown as a summation of families of dynamic analogs corresponding to the zeroth-order reverberations and the first-order topside and bottomside reverberations from the 660 and 410 discontinuities (top five traces); traces are labeled the same as in Figure 4a. (b) All the isolation filters that can be employed for this reverberative interval are shown together with the synthetic sum and the data; the traces are numbered on the right (S, synthetics, D, data). The zeroth-order phases ScS_n and $sScS_n$ are used individually as isolation filters (traces 1 and 2). For the first-order reverberations, the topside phases $sScS_n^{410+}$ and ScS_n^{660+} , which arrive at nearly the same time, are combined to create one isolation filter (trace 3); the bottomside reflections ScS_n^{410-} and $sScS_n^{660-}$ are also combined into one isolation filter (trace 5), for the same reason. The topside phase $sScS_n^{660+}$ and the bottomside phase ScS_n^{660-} do not interfere with any other arrival and are used individually as isolation filters if their signal-to-noise ratio is sufficiently high (traces 4 and 6, respectively). The ScS_n^{410+} and $sScS_n^{410-}$ arrivals, on the other hand, are too close to the primary $sScS_n$ and ScS_{n+1} phases, respectively, and cannot be measured separately without significant interference.

reference model of about +4 s, which agrees with global tomographic studies that find an anomalously slow lower mantle in this part of the central Pacific [Su *et al.*, 1994; Dziewonski *et al.*, 1996; Masters *et al.*, 1996].

More interesting, however, is the steep gradient in $ScS_3 - ScS_2$ and $ScS_4 - ScS_3$ differential times with epicentral

distance displayed in Figure 3. As discussed in section 2, these times require substantial lateral heterogeneity within the mantle of the Tonga-Hawaii corridor. We also note that the mean value of $ScS_n - ScS_m$ residual for the 1973 Hawaiian earthquake ($\Delta = 3^\circ$) is -0.2 s relative to the reference model, indicating that the average shear velocity of the sub-Hawaiian

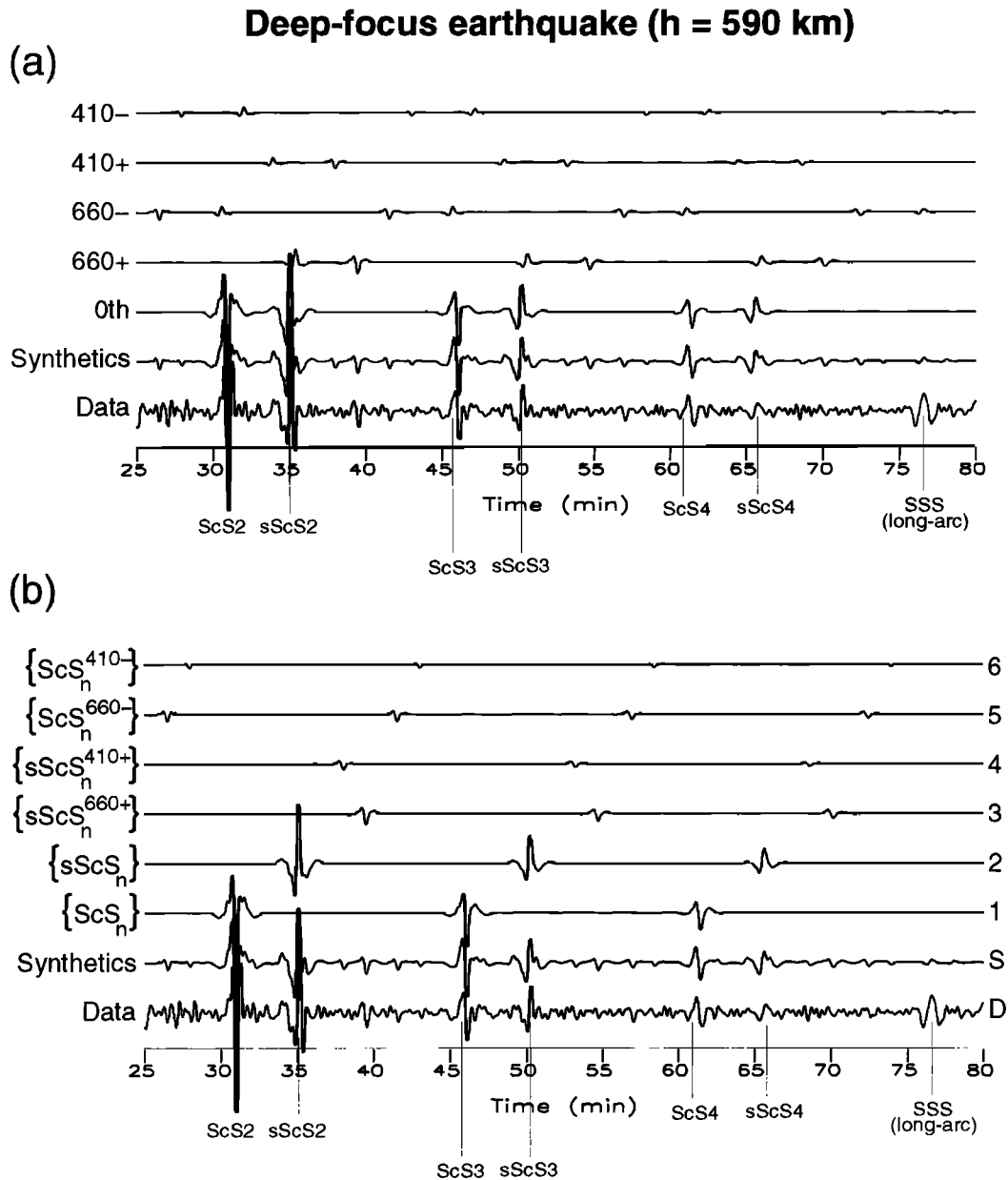


Figure 6. (a) Decomposition of a reverberative interval for a deep-focus earthquake ($h = 590$ km, $\Delta = 46.4^\circ$), organized and labeled the same as in Figure 5. (b) Isolation filters for the zeroth-order reverberations (traces 1 and 2) and for the first-order reverberations, whose only well-isolated phases are the topside $sScS_n^{660+}$ and $sScS_n^{410+}$ (traces 3 and 4) and the bottomside ScS_n^{660-} and ScS_n^{410-} (traces 5 and 6).

mantle is significantly higher than along the Tonga-Hawaii corridor. This is consistent with the $ScS_n - ScS_m$ travel times observed by *Sipkin and Jordan* [1980b], who also analyzed the amplitudes of ScS_n phases from the 1973 earthquake to show that the sub-Hawaiian mantle was less attenuating than the region between Tonga and Hawaii.

4. Frequency-Dependent Travel Times of Turning and Surface Waves

The ScS reverberations yield valuable data regarding along-path heterogeneity and discontinuity topography, but owing to their poor vertical resolution, they alone are insufficient to resolve the corridor structure at the level needed for a robust

geodynamical interpretation. Their times have therefore been combined with measurements of frequency-dependent travel times from a diverse assemblage of shear-dominated turning and surface waves registered in the direct-phase interval of the seismogram. These arrivals include the direct S phase and its surface reflection sS , the first-orbit surface waves R_1 and G_1 , and several dispersed wave groups that include the surface reflected SS , sSS , and SSS . At the epicentral distances available for the Tonga-Hawaii corridor, the ray theoretic turning points for the latter set lie in the upper mantle or top part of the lower mantle. While the ray theoretic phase notation supplies convenient designations, it does not really characterize the essential nature of these waves, which are formed through a complex series of interactions with the free

Table 1. Summary of the ScS Reverberation Measurements

Depth, km	Isolation Filter	Number of Observations for Core Reflection Number n			
		1	2	3	4
Shallow	{ ScS _n }		1	1	
	{ sScS _n }		1	1	
$h \leq 70$	{ ScS _n + sScS _n }	1	1	1	1
Intermediate $70 \leq h \leq 320$	{ ScS _n }		7	6	6
	{ sScS _n }		7	6	7
	{ ScS _n ⁴¹⁰⁺ + sScS _n ⁴¹⁰⁺ + ScS _n ⁶⁶⁰⁺ + sScS _n ⁶⁶⁰⁺ }				
	{ sScS _n ⁴¹⁰⁺ + ScS _n ⁶⁶⁰⁺ + sScS _n ⁶⁶⁰⁺ }		2	2	4
	{ sScS _n ⁴¹⁰⁺ + ScS _n ⁶⁶⁰⁺ }		5	5	3
	{ sScS _n ⁶⁶⁰⁺ }		5	4	3
	{ ScS _n ⁴¹⁰⁻ + sScS _n ⁴¹⁰⁻ + ScS _n ⁶⁶⁰⁻ + sScS _n ⁶⁶⁰⁻ }			1	1
	{ ScS _n ⁴¹⁰⁻ + ScS _n ⁶⁶⁰⁻ + sScS _n ⁶⁶⁰⁻ }	1	2		
	{ ScS _n ⁴¹⁰⁻ + sScS _n ⁶⁶⁰⁻ }	2	4	2	1
	{ ScS _n ⁶⁶⁰⁻ }		3	5	5
Intermediate/deep $290 \leq h \leq 520$	{ ScS _n }		9	8	8
	{ sScS _n }		9	8	7
	{ sScS _n ⁴¹⁰⁺ + ScS _n ⁶⁶⁰⁺ + sScS _n ⁶⁶⁰⁺ }		1	2	3
	{ sScS _n ⁴¹⁰⁺ + sScS _n ⁶⁶⁰⁺ }		2		
	{ sScS _n ⁴¹⁰⁺ + ScS _n ⁶⁶⁰⁺ }		1	2	
	{ ScS _n ⁶⁶⁰⁺ + sScS _n ⁶⁶⁰⁺ }			2	3
	{ sScS _n ⁶⁶⁰⁺ }		3	3	1
	{ ScS _n ⁶⁶⁰⁺ }		1		
	{ sScS _n ⁴¹⁰⁺ }		2	1	
	{ ScS _n ⁴¹⁰⁻ + ScS _n ⁶⁶⁰⁻ + sScS _n ⁶⁶⁰⁻ }		3	2	1
	{ ScS _n ⁴¹⁰⁻ + ScS _n ⁶⁶⁰⁻ }		1		
	{ ScS _n ⁴¹⁰⁻ + sScS _n ⁶⁶⁰⁻ }			1	4
	{ ScS _n ⁶⁶⁰⁻ + sScS _n ⁶⁶⁰⁻ }			2	
	{ ScS _n ⁶⁶⁰⁻ }		2	3	2
{ sScS _n ⁶⁶⁰⁻ }		1			
{ ScS _n ⁴¹⁰⁻ }		1	2		
Deep $h \geq 520$	{ ScS _n }		10	9	9
	{ sScS _n }		10	8	6
	{ sScS _n ⁴¹⁰⁺ + sScS _n ⁶⁶⁰⁺ }		4	4	
	{ sScS _n ⁶⁶⁰⁺ }		3	3	4
	{ sScS _n ⁴¹⁰⁺ }		3	2	
	{ ScS _n ⁴¹⁰⁻ + ScS _n ⁶⁶⁰⁻ }		1	3	3
	{ ScS _n ⁶⁶⁰⁻ }		3	4	3
{ ScS _n ⁴¹⁰⁻ }		2	2	2	

surface and upper mantle discontinuities and are better described as upper mantle guided waves. In fact, at these distances, the oceanic Love wave G_1 is itself an interference group comprising the fundamental and several higher modes [Thatcher and Brune, 1969; Gaherty et al., 1996].

Unlike the ScS reverberations, these arrivals are not very amenable to a ray theoretic analysis, especially in two and three dimensions. Waves with P - SV polarizations are

notorious in this respect, but this appraisal applies even to those in the simpler SH system. Here interconversions can usually be ignored, and the number of relevant ray paths is far less, but the importance of diffraction effects dictates the use of the rather cumbersome apparatus of generalized ray theory [Gilbert and Helmberger, 1972; Helmberger, 1983]; while methods like the Cagniard-de Hoop technique have been successfully applied in one dimension [e.g., Helmberger and

Wiggins, 1971; Grand and Helmberger, 1984], they are difficult to extend to higher dimensions [Hong and Helmberger, 1978]. Much work has been done in recent years to remedy this problem by devising generalized waveform analysis and inversion methodologies based on mode summation [e.g., Lerner-Lam and Jordan, 1983; Woodhouse and Dziewonski, 1984; Nolet, 1990; Li and Tanimoto, 1993; Marquering and Snieder, 1995].

4.1. GSDF Measurements and 2-D Fréchet Kernels

The GSDF technique of Gee and Jordan [1992] is particularly suitable for the type of tomography attempted in this study. It is based on observables that arise naturally in matched-filtering analysis, where synthetic waveforms (isolation filters) are cross-correlated with data seismograms. One of these observables, the phase-delay functional $\delta\tau(\omega)$, extends the concept of a differential travel time to a frequency-dependent measure of waveform dispersion (here we drop the subscript from Gee and Jordan's [1992] notation, $\delta\tau_p$). In GSDF analysis, the cross correlation between the isolation filter and the data seismogram is windowed to localize in time and narrowband filtered to localize in frequency; $\delta\tau(\omega)$ is measured as the phase shift between this cross correlagram, which can be approximated as a Gaussian wavelet, and a similar Gaussian wavelet obtained with a complete synthetic

for the reference model \mathbf{m}_0 . Figure 7 shows some examples of the results obtained from two seismograms used in this study. If \mathbf{m}_0 is a good starting model, in particular, one that properly represents the discontinuity structure of the mantle, then the isolation filter will be a reasonably good representation of the target wavegroup, and a linearized relationship between $\delta\tau(\omega)$ and the model perturbation $\delta\mathbf{m}$ will be adequate in posing the inverse problem. As emphasized by Gee and Jordan [1992], a principal advantage of the GSDF technique is that the linearity of this functional relationship does not require $\delta\tau(\omega)$ to be small compared to the wave period $T = 2\pi/\omega$, which is the requirement in waveform-inversion methods that linearize the relationship between the differential seismogram and $\delta\mathbf{m}$.

In this study, as in previous applications of the GSDF technique [Gaherty and Jordan, 1995; Gaherty et al., 1996; Kato and Jordan, submitted manuscript, 1997], complete synthetic seismograms were calculated by summing the normal modes with frequencies less than 50 mHz for a spherically symmetric, radially anisotropic model (in this case, PA5/PREM); all toroidal modes were summed for the transverse components of displacement, and all spheroidal modes were summed for vertical and radial components. The isolation filters were constructed by weighting each mode according to the target arrival's group and phase velocities, as well as its partitioning between compressional and shear

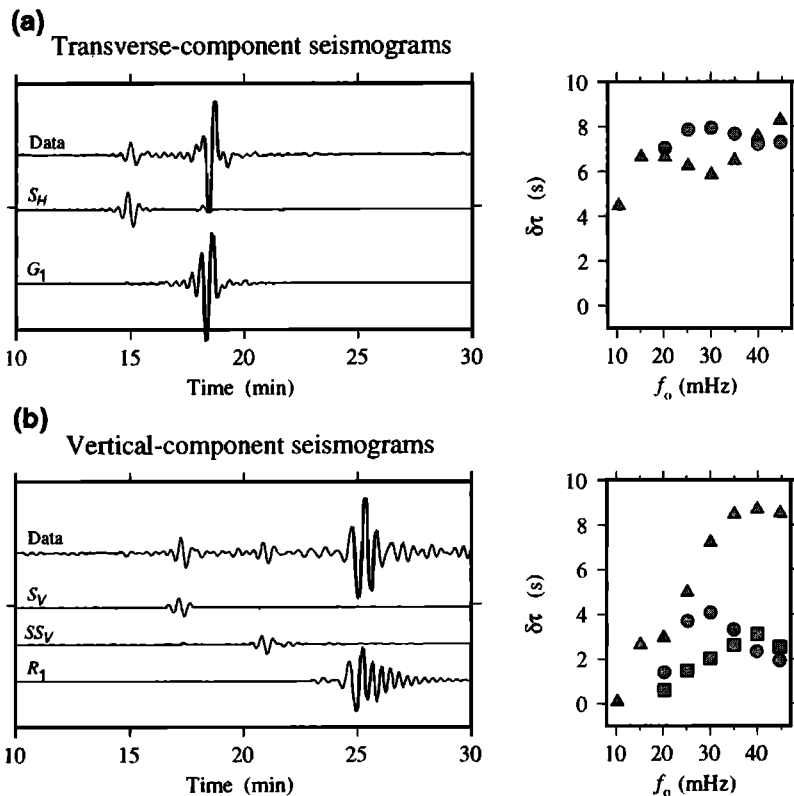


Figure 7. An example of the GSDF processing. (left) Transverse and vertical component seismograms recorded at HON from two shallow-focus Tonga ($h = 19$ km, $\Delta = 44^\circ$) and Kermadec ($h = 54$ km, $\Delta = 54^\circ$) events, respectively. Observed seismogram and the synthetic isolation filters (a) for S_H and G_1 and (b) for S_V , SS_V and R_1 . Timescale is relative to the origin time. (right) Frequency-dependent travel times, relative to the PA5/PREM reference model, measured from the seismograms on the left by the GSDF processing described in the text. The travel time measurements are shown at 5-mHz intervals for S_H and S_V (circles), SS_V (squares), and G_1 and R_1 (triangles). Examples of 2-D Fréchet kernel for some of these measurements are shown in Plate 2.

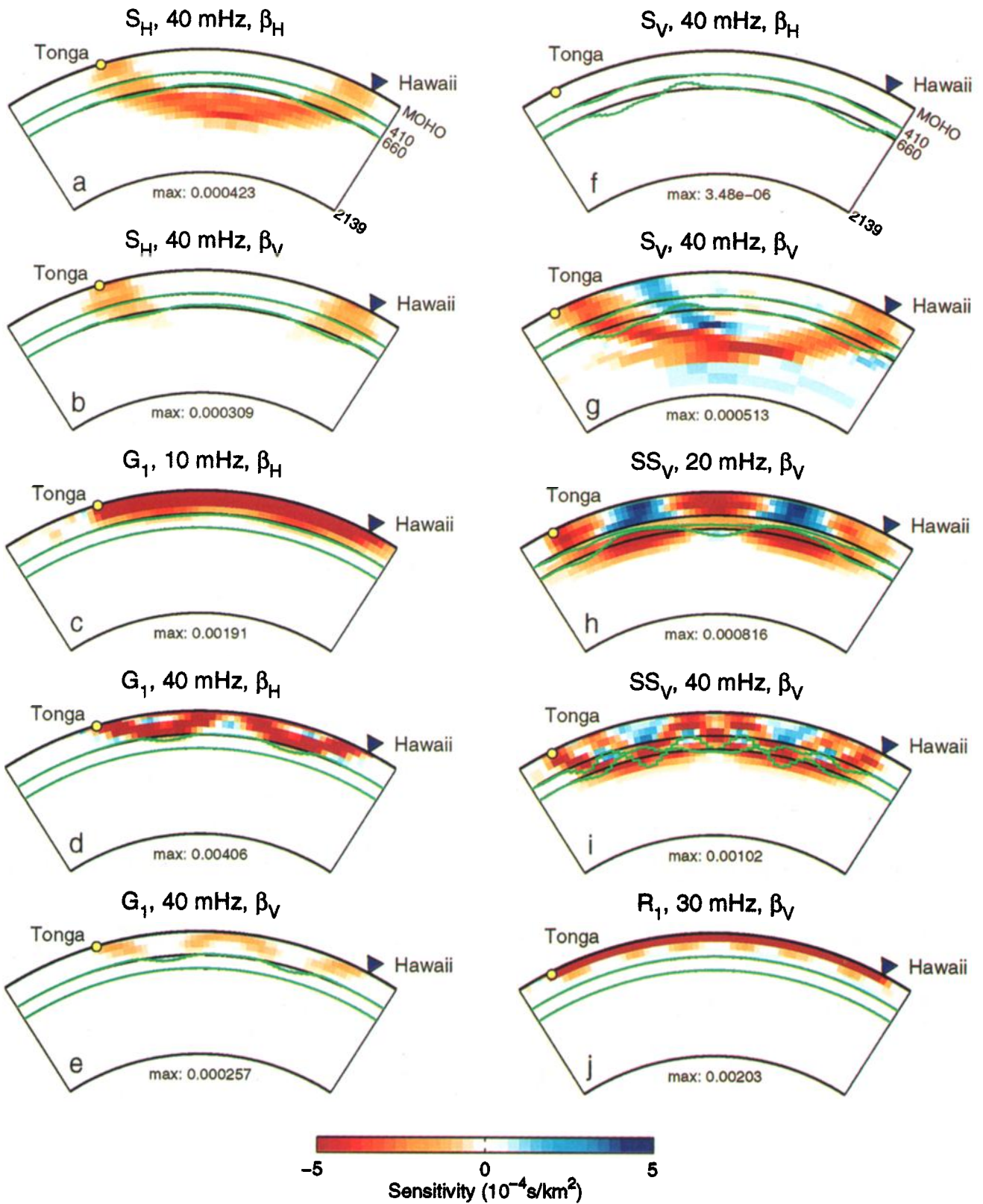


Plate 2. Examples of 2-D Fréchet kernel computed by coupled-mode summation for some of the measurements in Figures 7a and 7b. The wave type, frequency, and velocity type (β_H for horizontal and β_V for vertical shear velocity) are indicated at the top of each panel. As in Plate 1, warm colors correspond to negative sensitivity (phase delay increase for velocity decrease), cool colors correspond to positive sensitivity, and the green lines show the sensitivity to perturbations in the radii of 410 and 660 discontinuities (with twice the vertical exaggeration as that in Plate 1); yellow circles and blue triangles show the locations of the source and receiver, respectively. See text for discussion of these kernels.

energies. The weights obtained in this construction form a set of structure coefficients $\{0 \leq \alpha_k \leq 1, \text{ where } k \text{ is mode index}\}$ that relate the isolation filter to \mathbf{m}_0 , and they also specify the Fréchet kernel for $\delta\tau(\omega)$ as a sum over the kernels for individual modes [Gee and Jordan, 1992]. Examples of these structural factors are shown in Figure 8.

The GSDF theory thus yields a general procedure for constructing Fréchet kernels for essentially arbitrary isolation filters in either the *SH* or *P-SV* system, which allows the same measurement technique to be applied to a variety of waveforms on any component of ground motion. In previous applications, the phase delays have been iteratively inverted using 1-D kernels to obtain corridor-averaged structures, such as the PA5 model. In the present study, we have utilized the 2-D kernels for $\delta\tau(\omega)$ calculated by a coupled-mode algorithm that accounts for wave interactions in the vertical source-receiver plane [Zhao and Jordan, 1998]. The algorithm is based on first-order normal-mode perturbation theory [Woodhouse, 1980, 1983], and the heavy computational labor required for a full implementation of the theory has been reduced in two ways. First, we have followed Li and Tanimoto [1993] in approximating the angular functions by their asymptotic forms and performing a stationary-phase integration in the direction transverse to the source-receiver plane, which reduces the kernel from 3-D to 2-D and decouples the toroidal and spheroidal modes. Second, we have summed the coupling terms only over modes whose structure coefficients α_k were nonzero. (To keep this set as small as possible, we employed cosine tapers in our weighting scheme rather than the Gaussian factors used by Gee and Jordan [1992] and Gaherty et al. [1996].)

Such kernels properly represent the sampling of Earth structure by the band-limited observations of $\delta\tau(\omega)$ and account for all of the interactions among the various waves that contribute to the target wave group. They do not, however, include the effects of perturbations to extraneous phases that interfere with the target wave group. In cases where *ScS* interferes with *SS*, for example, the GSDF expressions for the *SS* kernels should include *ScS* contributions because perturbations to the latter phase by, say, velocity variations in the lowermost mantle, will affect the apparent phase delay of *SS* [Gee and Jordan, 1992]. Although this type of effect has been incorporated in the 1-D modeling (see Figures 5 and 6 of Gaherty et al. [1996] for a clear example), we have not attempted to do so here. Therefore we have restricted our measurements to cases where the interference by extraneous phases was small.

4.2. Sampling Properties

Zhao and Jordan [1998] give explicit expressions for 2-D Fréchet derivatives of $\delta\tau(\omega)$ with respect to mass density ρ , discontinuity topography h_i and the five elastic parameters ($\alpha_H, \alpha_V, \beta_H, \beta_V, \eta$) of a radially anisotropic Earth model. However, the residuals of the shear-dominant phases used here are sensitive mostly to the unknown lateral variations in h_i, β_H , and β_V , and we have thus limited the model perturbations to these quantities. This approximation should be especially good for the Tonga-Hawaii corridor because the residuals have been referenced to the radially anisotropic PA5 model, in which the discontinuity depths and all six volumetric parameters were derived by a nonlinear inversion of data from this particular corridor [Gaherty et al., 1996].

A selection of the Fréchet kernels for the transverse component data of Figure 7a are displayed in Plates 2a-2e and for the vertical component data of Figure 7b in Plates 2f-2j. At 40 mHz, the sensitivity of the S_H travel time to β_H is highest near its turning point in the lower mantle where it travels more horizontally (Plate 2a), and its sensitivity to β_V is highest near the source and receiver, where it travels more vertically (Plate 2b). The S_V travel time is independent of β_H (Plate 2f), but its dependence on β_V is complicated (Plate 2g). In this particular example, the sP_nS phase arrives in the *S* window, which introduces a region of positive sensitivity (blue color) above the near-source leg of the *S* path; i.e., a delay in sP_nS will actually advance the *S* arrival. To see this, consider two narrowband phases with amplitudes $a_1 > a_2 > 0$ that arrive with a relative phase delay of magnitude

$$|\tau_1 - \tau_2| \approx (2n-1)\pi/\omega \ll 1/\sigma, \quad (5)$$

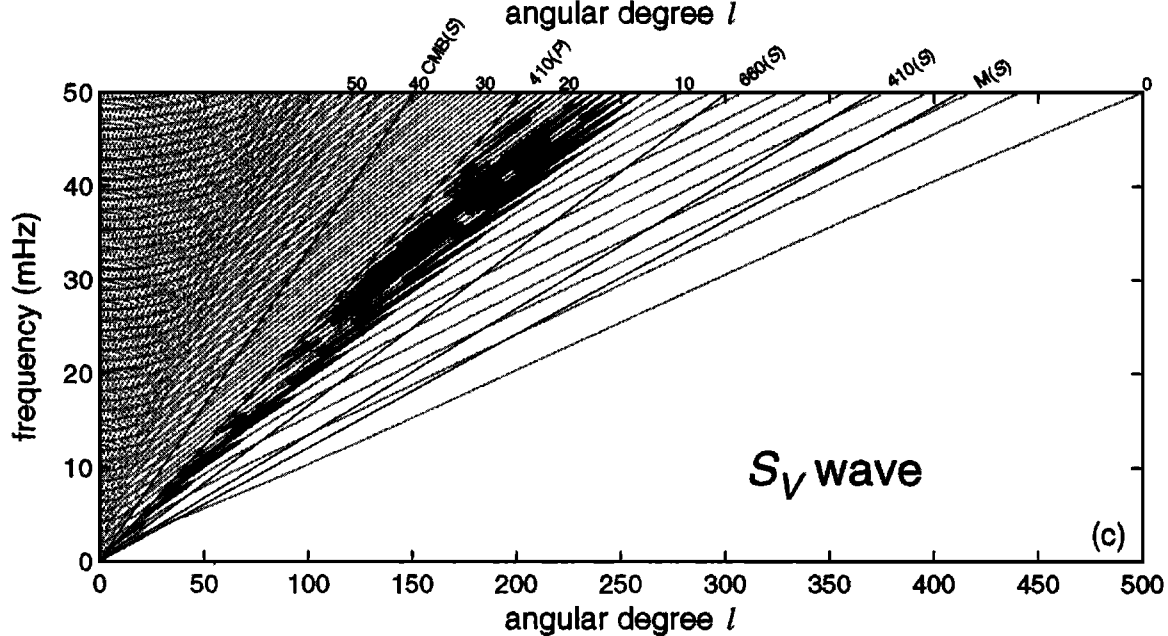
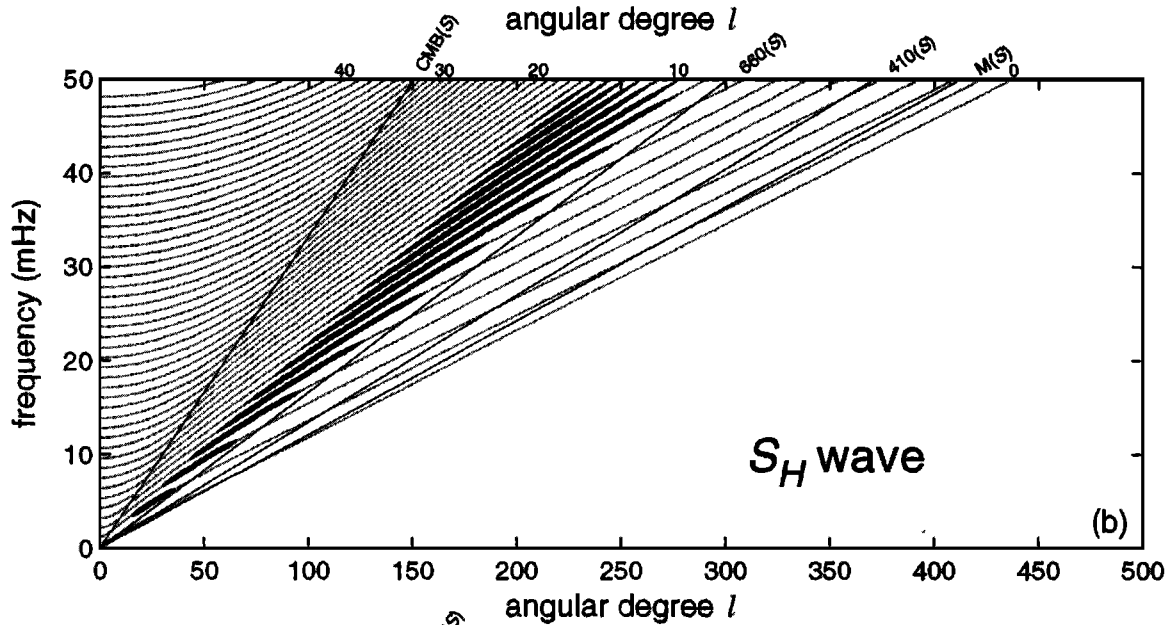
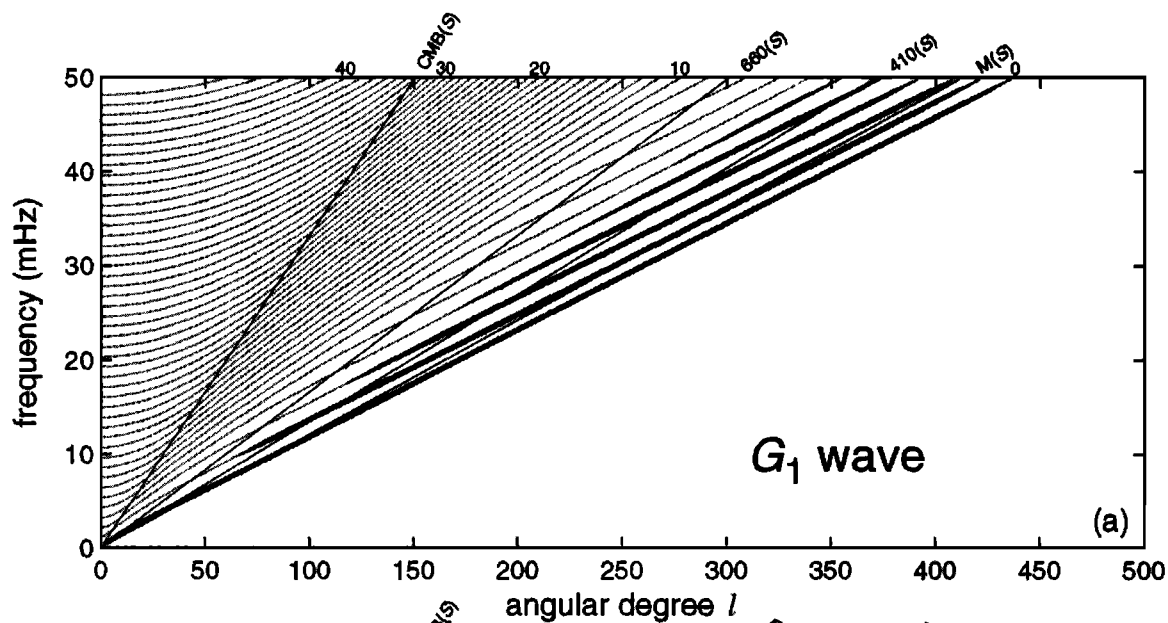
where ω is the center angular frequency of the pulses, σ is their half bandwidth and n is an integer; equations (2)-(4) then show that the Fréchet kernel of the phase delay for the combined wave group is

$$K \approx \frac{a_1 K_1 - a_2 K_2}{a_1 - a_2}. \quad (6)$$

In this example, the sP_nS phase is delayed relative to *S* by 25 s, which at 40 mHz satisfies criterion (5) for $n = 1$.

The frequency dependence of the narrowband phase delays provides considerably more information than a single broadband travel time. This can be illustrated by the phase delays of a Love wave at low and high frequencies. At 10 mHz, the G_1 group is dominated by the fundamental-mode surface wave with a kernel that averages β_H fairly uniformly over the

Figure 8. (opposite) Toroidal-mode dispersion diagrams for model PA5/PREM showing the weighting factors in the partial normal-mode summations for the isolation filters of (a) the G_1 and (b) the S_H waves in Figure 7a. (c) Spheroidal-mode dispersion diagram for PA5/PREM showing the weighting factors in the partial normal-mode summation for the isolation filter of the S_V wave in Figure 7b. The sizes of the open circles are proportional to the values of the weighting factors for the corresponding modes. The four straight diagonal lines in Figures 8a and 8b correspond to the ray parameter values at which the *S* wave grazes, counterclockwise from the right, the Moho, the 410 and 660 discontinuities, and the CMB, respectively. The five lines in Figure 8c also include the ray parameter at which the *P* wave grazes the 410 discontinuity (fourth straight diagonal line, counterclockwise from the right). The branch numbers $n = 0, 10, 20, 30$ and 40 are indicated at the top of each diagram. Note that the isolation filter for the G_1 wave group in Figure 8a is dominated by the fundamental-mode branch only at low frequencies, while at high frequencies, it includes contributions from higher modes corresponding to *S* waves which graze around and above the 410 discontinuity. Note also the complicated structure of the partial normal-mode summation for the S_V wave group. These features are discussed in the text and are reflected in Plate 2.



crust and the top few hundred kilometers of the mantle (Plate 2c). At 40 mHz, however, the same group is dominated by the higher modes (Figure 8a; see also Figure 12 of *Gaherty et al.* [1996]), and its travel time samples β_H and β_V along a trajectory that porpoises through the upper mantle, with one upper reflection at the free surface between two turning points near the 410 discontinuity (Plates 2d and 2e). This *SS*-like sensitivity comes from the cross coupling between the overtone branches [*Li and Tanimoto*, 1993], and it illustrates the limitation of the path-averaging assumption for guided waves.

The along-path sampling by the *SS_V* wave group also varies substantially with its center frequency (Plates 2h and 2i), owing to frequency-dependent interactions with other arrivals such as *sSS*, *SPS*, and *SSP*. At 20 mHz, the negative regions (red colors) outline its character as an *SS* wave with a surface reflection and turning points at the top of the lower mantle, but the upper mantle above the turning points show positive sensitivity (blue colors) not expected from ray theory. Like the *ScS_n - ScS_m* examples in Plates 1c and 1d, this data functional is particularly sensitive to harmonic variations in upper mantle structure, in this case, at horizontal wavelengths of the order of $\Delta/2$, rather than $\Delta/3$. The kernel at 40 mHz, on the other hand, fluctuates in a complicated pattern rich with shorter wavelengths. For example, the topography kernel for the 410 has its power concentrated at $\Delta/6$.

Plate 2 displays the kernels for only 6 of the 34 data obtained from the two seismograms in Figure 7. By combining them with similar measurements from sources at different hypocentral depths and distances, we can obtain a data set with excellent upper-mantle resolution, as documented in Appendices A and B.

4.3. Data for the Tonga-Hawaii Corridor

The data set comprised 1122 frequency-dependent phase delays from 179 waveforms on 115 long-period seismograms (49 vertical, 15 radial, and 51 transverse components). The seismograms were recorded at either KIP or HON from 63 Tonga-Fiji earthquakes at epicentral distances ranging from 39° to 57° and focal depths from 10 to 663 km (Figure 1). The earthquakes were of moderate size ($5.9 \leq M_w \leq 7.2$) with well-determined Harvard centroid moment tensor (CMT) solutions. Many of the seismograms were analyzed previously in the 1-D study by *Gaherty et al.* [1996], and a number of the transverse

components were the source of the data for the *ScS* reverberations data discussed in section 3. The same measurements were used in our preliminary 2-D study of this corridor [*Katzman et al.*, 1997].

Prior to measurement, the data seismograms and their corresponding synthetics were low-passed with a zero-phase filter having a corner frequency of 45 mHz. Isolation filters were constructed for candidate wave groups, and the data were downgraded or eliminated if the agreement was poor either because of low snr or interference by phases not included in the isolation filter (e.g., *ScS*). The isolation filters were cross-correlated with the data seismograms, and the resulting time series were windowed and filtered in 5-mHz bands between 10 and 45 mHz. The phase delays recovered by fitting Gaussian wavelets to the narrowband cross correlagrams were corrected for windowing and filtering effects and interference with other wave groups using the procedures discussed by *Gee and Jordan* [1992]. Table 2 summarizes the data distribution by wave type.

5. Vertical Tomograms

The *ScS* reverberation times and frequency-dependent phase delays have been inverted for 2-D structure in the vertical plane of the Tonga-Hawaii corridor using the model parameterization and the linear Gaussian-Bayesian inversion scheme described in this section.

5.1. Parameterization

The along-path structure was represented by a perturbation vector $\delta\mathbf{m}$ to the PA5/PREM reference model \mathbf{m}_0 of dimension $M = 1375$. It was organized into three parts:

1. There are 985 blocks representing the relative variations in isotropic shear velocity, $\delta\beta/\beta_0$, over the entire length of the corridor (65°) and depth of the mantle (2890 km). Blocks with a lateral dimension of 1° and an average vertical dimension of about 110 km were used in four layers above the 410 discontinuity, two in the transition zone, and five in the lower mantle from 651 to 1200 km (715 blocks total). Below 1200 km, where the data resolution was substantially lower, we coarsened the grid to nine layers of 30 blocks each ($\sim 2.2^\circ \times 250$ km) extending to the core-mantle boundary. The grid is depicted in Plate 3a.

Table 2. Summary of the Inversion Results for Model TH2

Phase	Number of Data	Data Importance	χ^2 / D			Variance Reduction
			Reference Model	After Denuisancing*	After Inversion	
Rayleigh	168	4.17	12.90	2.81	2.09	0.84
Love	113	3.79	12.79	1.43	1.35	0.89
<i>S_V</i>	285	6.68	6.00	1.74	0.73	0.88
<i>S_H</i>	292	6.19	7.01	2.79	0.59	0.91
<i>SS_V</i>	133	7.07	4.60	1.74	0.80	0.83
<i>SS_H</i>	59	3.26	8.07	1.66	1.91	0.76
<i>SSS_V</i>	66	2.23	16.30	2.48	1.73	0.89
<i>SSS_H</i>	6	0.04	0.78	0.34	0.56	0.28
Zeroth-order reverberations	148	5.70	245.11	12.50	1.41	0.99
First-order reverberations	156	7.76	164.73	9.91	3.63	0.98
All phases	1426	46.90	50.15	4.09	1.41	0.97

* This column shows the χ^2 estimates (normalized by the number of data) after projecting the errors in source origin time (and depth for the reverberative interval) out of the original data.

2. There are 260 blocks representing the relative variations in shear velocity anisotropy, $(\delta\beta_H - \delta\beta_V)/\beta_0$, in the four upper mantle layers above the 410 discontinuity; here $\delta\beta_H$ and $\delta\beta_V$ are the perturbations to the radially anisotropic shear velocities in PA5, $(\beta_H)_0$ and $(\beta_V)_0$, and β_0 is the average $[(\beta_H)_0 + (\beta_V)_0]/2$.

3. Two sets of 65 segments represent the topographic variations, δr_{410} and δr_{660} , for the two major transition zone discontinuities.

The perturbation was assumed to satisfy the linear system

$$\mathbf{A}\delta\mathbf{m} + \mathbf{B}\delta\mathbf{n} + \mathbf{e} = \delta\mathbf{d}, \quad (7)$$

where $\delta\mathbf{d}$ is the data residual vector of dimension $D=1426$ (1122 frequency-dependent phase delays and 304 ScS reverberation times). \mathbf{A} is the $D \times M$ partial derivative matrix whose general element A_{ij} is the integral over the j th model cell of the Fréchet kernels for the i th datum, calculated for \mathbf{m}_0 . The data error vector \mathbf{e} is assumed to have a zero mean, $\langle \mathbf{e} \rangle = \mathbf{0}$, and a diagonal covariance matrix, $\mathbf{C}_{ee} = \langle \mathbf{e}\mathbf{e}^T \rangle = \text{diag}[\sigma_1^2, \sigma_2^2, \dots, \sigma_D^2]$. The vector $\delta\mathbf{n}$ comprises the "nuisance parameters", i.e., unknown quantities not contained in the model that could possibly contaminate the data, such as source statics. In this study, $\delta\mathbf{n}$ contained only two types of source parameters: a perturbation to the centroid time for each earthquake, and an apparent shift in centroid depths for each ScS reverberation seismogram. Since we are using only two colocated stations, the single-station static is redundant with the source statics and therefore does not have to be explicitly included in $\delta\mathbf{n}$.

5.2. Bayesian Inversion

For the 2-D inversions considered here, the dimension of the linear system (7) is sufficiently small that we could afford to invert the data and to evaluate the resulting model using a complete Bayesian methodology [Tarantola and Valette, 1982; Tarantola, 1987]. The difference between the actual Earth structure and the 1-D reference model \mathbf{m}_0 was represented as a realization of an a priori Gaussian probability density function with expectation $\overline{\delta\mathbf{m}}$ and a positive-definite covariance matrix $\overline{\mathbf{C}}_{mm}$. The prior model, $\overline{\mathbf{m}} = \mathbf{m}_0 + \overline{\delta\mathbf{m}}$, was taken to be the path-averaged structure, obtained by inverting the data for a 1-D, depth-dependent perturbation. The prior covariance $\overline{\mathbf{C}}_{mm}$ was specified according to the amplitude, smoothness, and correlation criteria discussed in section 5.3. The nuisance parameter vector was assumed to have zero expectation and prior covariance $\overline{\mathbf{C}}_{nn}$. In this Gaussian case, the Bayesian estimates minimize the quadratic form

$$\begin{aligned} \epsilon^2 = & (\delta\mathbf{d} - \mathbf{A}\delta\mathbf{m} - \mathbf{B}\delta\mathbf{n})^T \mathbf{C}_{ee}^{-1} (\delta\mathbf{d} - \mathbf{A}\delta\mathbf{m} - \mathbf{B}\delta\mathbf{n}) \\ & + (\delta\mathbf{m} - \overline{\delta\mathbf{m}})^T \overline{\mathbf{C}}_{mm}^{-1} (\delta\mathbf{m} - \overline{\delta\mathbf{m}}) + \delta\mathbf{n}^T \overline{\mathbf{C}}_{nn}^{-1} \delta\mathbf{n}. \end{aligned} \quad (8)$$

The expressions can be simplified by normalizing the fixed quantities in (8) by the standard deviation matrix for the data, $\delta\mathbf{d}' = \mathbf{C}_{ee}^{-1/2} \delta\mathbf{d}$, $\mathbf{A}' = \mathbf{C}_{ee}^{-1/2} \mathbf{A}$, $\mathbf{B}' = \mathbf{C}_{ee}^{-1/2} \mathbf{B}$. In this notation, the posterior estimate of the model perturbation becomes

$$\delta\mathbf{m} = \overline{\delta\mathbf{m}} + (\mathbf{A}'^T \mathbf{Q}_B \mathbf{A}' + \overline{\mathbf{C}}_{mm}^{-1})^{-1} \mathbf{A}'^T \mathbf{Q}_B (\delta\mathbf{d}' - \mathbf{A}' \overline{\delta\mathbf{m}}), \quad (9)$$

where

$$\mathbf{Q}_B = \mathbf{I} - \mathbf{B}' (\mathbf{B}'^T \mathbf{B}' + \overline{\mathbf{C}}_{nn}^{-1})^{-1} \mathbf{B}'^T. \quad (10)$$

To avoid any overinterpretation of the data, we assumed total prior ignorance of the source parameters contained in

$\delta\mathbf{n}$. In this limiting case ("exact denuisancing"), $\overline{\mathbf{C}}_{nn} \rightarrow \infty$ and $\mathbf{Q}_B \rightarrow \mathbf{I} - \mathbf{B}' (\mathbf{B}'^T \mathbf{B}')^{-1} \mathbf{B}'^T$, the projection operator onto the null space of \mathbf{B}'^T (i.e., $\mathbf{Q}_B \mathbf{B}' = \mathbf{0}$ and $\mathbf{Q}_B \mathbf{Q}_B = \mathbf{Q}_B$). In terms of the transformed partial derivative matrix $\mathbf{A}' = \mathbf{Q}_B \mathbf{A}'$ and data vector $\delta\mathbf{d}' = \mathbf{Q}_B \delta\mathbf{d}'$, the estimate becomes

$$\delta\mathbf{m} = \overline{\delta\mathbf{m}} + (\mathbf{A}'^T \mathbf{A}' + \overline{\mathbf{C}}_{mm}^{-1})^{-1} \mathbf{A}'^T (\delta\mathbf{d}' - \mathbf{A}' \overline{\delta\mathbf{m}}). \quad (11)$$

This projection completely removes any constraints on the Earth structure that could otherwise be explained by adjusting the source parameters [Pavlis and Booker, 1980; Spencer and Gubbins, 1980].

The posterior covariance of the model estimate can be written

$$\mathbf{C}_{mm} = (\mathbf{A}'^T \mathbf{A}' + \overline{\mathbf{C}}_{mm}^{-1})^{-1}. \quad (12)$$

The diagonal elements of this matrix $C_{mm}(i,i)$ give the posterior marginal variances of the model parameters, and the off-diagonal terms specify the posterior correlations between the i th and the j th parameters:

$$\rho(i,j) = \frac{C_{mm}(i,j)}{\sqrt{C_{mm}(i,i)C_{mm}(j,j)}}. \quad (13)$$

A strong posterior correlation ($\rho \rightarrow 1$) or anticorrelation ($\rho \rightarrow -1$) implies that the two parameters cannot be resolved independently by the data [Tarantola, 1987]. In general, a particular parameter is well resolved by the data if its variance reduction is large. For any direction $\hat{\mathbf{m}}$ in the model space, the variance reduction is

$$R(\hat{\mathbf{m}}) = \mathbf{I} - (\hat{\mathbf{m}}^T \mathbf{C}_{mm} \hat{\mathbf{m}}) / (\hat{\mathbf{m}}^T \overline{\mathbf{C}}_{mm} \hat{\mathbf{m}}). \quad (14)$$

$R(\hat{\mathbf{m}})$ will be larger in directions where the data information dominates over the prior information. Equations (12)-(14) were used in error analysis discussed in Appendix B.

5.3. Specification of the Correlation Matrices

The standard deviations of the travel time residuals, $\{\sigma_i\}$, varied from 1 s for high-quality observations to more than 8 s for low-quality observations. These errors were assigned according to the snr on the raw seismogram (including unmodeled interference with other phases), and the center frequency and bandwidth of the observation (low-frequency, narrowband times being less precise, especially for the direct turning waves). They were calibrated by comparing the same types of observations from sources having nearby hypocenters. The procedures taken to insure the data quality included careful choice of the time windows, remeasurement of large outliers, and rejection of any observation judged to have substandard quality; consequently, over 50% of the 1426 times have standard deviations of less than 2 s.

The prior covariance matrix $\overline{\mathbf{C}}_{mm}$ was specified in terms of the prior standard deviations $\overline{C}_{mm}^{1/2}(i,i)$ and the prior correlations $\overline{\rho}(i,j)$ among model elements. Table 3 summarizes the parameters adopted for the various tomographic inversions shown in Plates 3 and 4 and Figure 9. The prior standard deviations were assumed to be constant in the uppermost mantle above the 410 discontinuity ($\overline{C}_{mm}^{1/2}(i,i) = \overline{\sigma}_{UM}$), in the transition zone between the 410 and the 660 ($\overline{\sigma}_{TZ}$), and in the lower mantle below the 660 ($\overline{\sigma}_{LM}$). Global and regional tomographic studies [e.g., Grand, 1994; Su et al., 1994; Dziewonski et al., 1996; Masters et al., 1996;

Table 3. Summary of the Inversion Tests Corresponding to the Models in Plates 3 and 4

Model	σ_{UM} %	σ_{TZ} %	σ_{LM} %	σ_{AN} %	σ_{410} km	σ_{660} km	χ^2_{GSDF} D	χ^2_{REV} D	χ^2_{TOT} D	Remarks
TH1	2	1	0.5	0.5	10	10	1.11	2.58	1.42	
TH2	2	1	0.5	0.5	10	10	1.09	2.58	1.41	
TH2.a	2	1	0.5	0.5	10	10	1.00	-----	1.00	ScS reverberation data excluded
TH2.b	2	1	0.5	1	10	10	1.06	2.57	1.38	
TH2.c	2	1	0.5	0	0	0	1.14	3.01	1.53	
TH2.d	2	1	0.5	0.5	8.4	5.6	1.12	2.80	1.48	equilibrium-olivine model enforced*
TH2.e	2	1	0.1	0.5	10	10	1.18	2.63	1.49	
TH2.f	1	1	1	0.5	10	10	1.09	2.56	1.40	

* The enforcement of an equilibrium-olivine model through the prior covariance matrix is described in the text.

Li and Romanowicz, 1996] have shown that shear velocity heterogeneities at midmantle depths are weak, with a root-mean-square (rms) variability of about 0.5% (or less in the case of Grand's model), and their magnitude increases through the transition zone toward a maximum of about 2% in the thermal and chemical boundary layers near the surface [cf. Li and Romanowicz, 1996, Figure 10; Puster and Jordan, 1997, Figure 6]. Our preferred model (TH2) was constructed using values consistent with global tomography: $\bar{\sigma}_{UM} = 2\%$, $\bar{\sigma}_{TZ} = 1\%$, and $\bar{\sigma}_{LM} = 0.5\%$. For the anisotropic parameter $(\delta\beta_H - \delta\beta_V)/\beta_0$, we chose a standard deviation of $\bar{\sigma}_{AN} = 0.5\%$ in the uppermost mantle down to 166 km, where we reduced it to 0.1% and tapered to zero from below 300 km where the radial anisotropy appears to be weaker [Regan and Anderson, 1984; Cara and Lévesque, 1988; Nishimura and Forsyth, 1989]. Gaherty et al. [submitted manuscript, 1997] tested the depth extent of anisotropy for the Tonga-Hawaii corridor and concluded that below about 200 km the radial anisotropy is weak (< 1%), and models that allow deeper anisotropy do not fit the data significantly better.

The preferred values for the discontinuity topographies were $\bar{\sigma}_{410} = \bar{\sigma}_{660} = 10$ km, which are comparable to the variability estimated on a larger scale for the central and western Pacific by Revenaugh and Jordan [1991b] or obtained in the global model of Shearer [1993] and Flanagan and Shearer [1998]. Recent estimates for the Clapeyron slopes of the exothermic transition from α - to β -olivine at the 410 discontinuity and the endothermic transition from γ -olivine to perovskite+ferropicicase at the 660 discontinuity are 3.0 and -2.3 MPa \cdot K $^{-1}$, respectively [Bina and Helffrich, 1994], which imply $\partial r_{410}/\partial T \approx -0.084$ km \cdot K $^{-1}$ and $\partial r_{660}/\partial T \approx 0.056$ km \cdot K $^{-1}$. When anelastic effects are taken into account, the temperature derivative of relative shear velocity in the transition zone is estimated to be $(\partial \ln \beta / \partial T)_{TZ} \approx -10^{-4}$ K $^{-1}$ [Karato, 1993]. This simple "equilibrium-olivine" thermal model derived from laboratory-based mineral physics data predicts that a temperature decrease of 100 K in the transition zone would induce a 1% velocity increase, an 8.4-km elevation of the 410, and a 5.6-km subsidence of the 660, which are fairly consistent with the adopted values of $\bar{\sigma}_{TZ}$, $\bar{\sigma}_{410}$, and $\bar{\sigma}_{660}$. However, it ignores potentially important phase changes in the garnet component of mantle composition. [Weidner and Wang, 1998].

A Gaussian form was chosen for the prior correlation function [e.g., Tarantola and Nercessian, 1984]:

$$\bar{\rho}(i, j) = s_{ij} \exp\left[-(r_i - r_j)^2 / 2l_i^2 - (\theta_i - \theta_j)^2 / 2l_\theta^2\right], \quad (15)$$

where r_i and θ_i are the coordinates at the center of the i th block, $s_{ij} = s_{ji}$ is a selection coefficient, and l_i and l_θ are

radial and angular correlation lengths, respectively. For most of the inversion runs, we adopted $l_r = 250$ km and $l_\theta = 5^\circ$. The latter yields a horizontal correlation length of about 300 km at the base of the mantle and 550 km near its top. In all but one of the inversions listed in Table 3, the selection coefficients s_{ij} were taken to be unity if both the i th and j th model parameters were of the same type (e.g., $\delta\beta/\beta_0$, $(\delta\beta_H - \delta\beta_V)/\beta_0$, δr_{410} , or δr_{660}) and zero otherwise; i.e., no prior correlation among parameters of different types. The exception was for an experiment in which we adopted the equilibrium-olivine thermal model of transition zone structure (TH2.d), for which we assumed $s_{ij} = 1$ if $i \in \delta r_{410}$ and $j \in \delta\beta/\beta_0$, and $s_{ij} = -1$ if $i \in \delta r_{660}$ and $j \in [\delta\beta/\beta_0 \cup \delta r_{410}]$; this correlates the 410 and 660 topographies negatively with each other and positively and negatively, respectively, with their nearby shear-velocity perturbations.

5.4 Model TH2

The preferred model for the Tonga-Hawaii corridor, TH2, is shown as a perturbation to the PA5/PREM reference model in Plate 3b. This inversion used a parameterization identical to our previous TH1 model [Katzman et al., 1997] (Plate 3a) and a data set that differed primarily by the inclusion of the near-vertical ScS_n times from the 1973 Hawaiian earthquake (13 phase delays with low-quality Fréchet kernels were also downweighted relative to the TH1 inversion). For both data sets, a 1-D, spherically symmetric perturbation $\delta\bar{\mathbf{m}}$ to the PA5/PREM reference model $\bar{\mathbf{m}}_0$ was constructed by inverting the entire data set for a path-averaged structure, which was then used as the prior model in the subsequent 2-D inversions. Not surprisingly, PA5 turned out to be an excellent representation of the path-averaged structure for the Tonga-Hawaii upper mantle, and the perturbations in this region were small (only 1.5 km for the 660-km discontinuity, for example). They were also very small in the midmantle, so that the only region where $\delta\bar{\mathbf{m}}$ was significantly different from zero was the lowermost mantle, where the perturbation was negative, reaching about 1.5% in D". This result is consistent with previous global and regional studies that indicate the lowermost mantle beneath this corridor is slow relative to the average Earth [Dziewonski et al., 1996; Masters et al., 1996; Garnero and Helmberger, 1996; Wysession, 1996].

The primary feature in both models is the alternating series of highs and lows in upper mantle shear velocity with wavelength of 1500 km and amplitude of about 3% between the northern end of the Tonga trench and the island of Oahu. Both models also exhibit a large high-velocity region in the lower mantle below the Tonga subduction zone extending to about 1200 km, anticorrelated topography on the 410 and 660

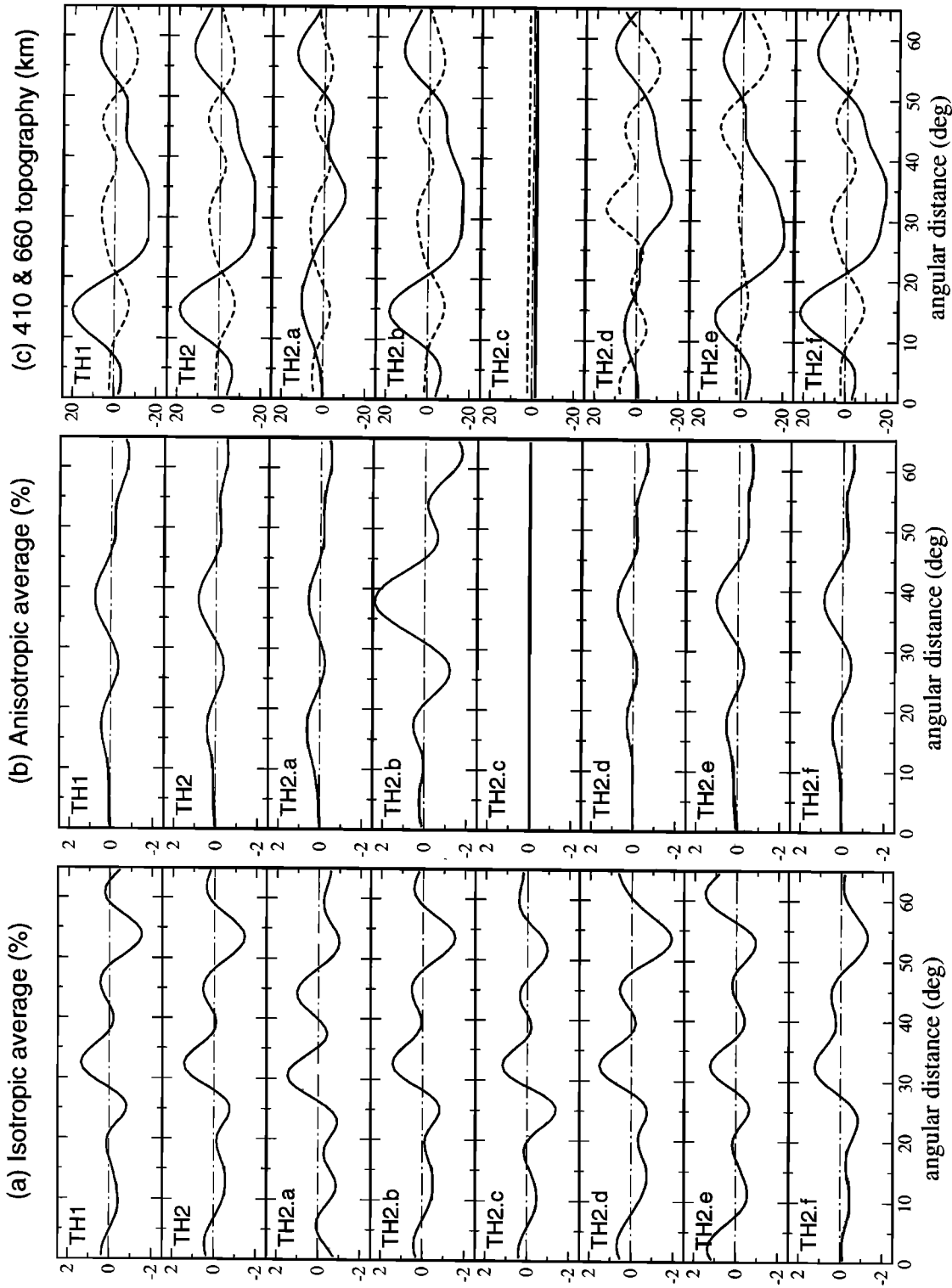


Figure 9. (a) Relative shear velocity perturbation, averaged over the upper 651 km of the mantle (upper six grid layers); (b) relative perturbation in radial anisotropy, averaged over the upper 166 km of the mantle (upper two grid layers); and (c) topographic perturbation of the 410 (dashed line) and 660 (solid line) discontinuities for the eight models in Table 3 and in Plates 3 and 4. The corresponding model names are indicated. The angular distance is measured from the edge of the corridor near Tonga. Note the robustness of the pattern for the upper mantle isotropic anomalies and the anticorrelation between the 410 and 660 discontinuity topographies.

discontinuities (Figure 9c), and small lateral variations in radial anisotropy. The main difference between the two models is that TH2 has higher shear velocities in the transition zone and lower mantle directly below Hawaii, dictated by the relatively fast $ScS_n - ScS_m$ residuals from the 1973 event [Sipkin and Jordan, 1980b]. The distribution of the high velocities below Hawaii is uncertain, however, because the resolving power of the data set for the vertical structure of this near-receiver region is relatively low; it is possible, for example, that this high-velocity anomaly might be concentrated more toward the upper mantle (see below).

TH2 gives a good overall fit to the data, with a normalized chi-square of $\chi^2/D = 1.4$ and a total variance reduction of 97% (Table 2). Much of this reduction is ascribable to the source statics and the 1-D perturbation to the starting model, however; the variance reduction that results from the 2-D perturbation alone is only 53%. The model satisfies the general trends in the $ScS_n - ScS_m$ differential travel times (Figure 10), although it tends to underpredict the steep slope in the variation of $ScS_4 - ScS_3$ residuals with epicentral distance. The feature primarily responsible for these trends is the nearly harmonic variation of shear velocity in the upper mantle, which has about the same horizontal wavelength (~1500 km) as the kernels for the $ScS_n - ScS_m$ differential travel times (compare Plates 1c and 1d). Increasing the horizontal correlation length l_θ above the 5° value used in this inversion gives a smoother structure and degrades the fit to these data.

The resolving power of the TH2 inversion has been investigated through a series of checkerboard inversions and other tests (Appendix A). In all inversion tests using synthetic data, Gaussian noise with standard deviations similar to the error estimates for the real data (up to ~8 s) was added to the synthetic data. Patterns with horizontal

wavelengths of 1500 km are well resolved in the upper mantle but not in the lower mantle (Plate 6). The resolution at lower mantle depths is decreased because the turning point depths for most of the frequency-dependent phase delays are confined to the upper mantle or the top part of the lower mantle (Plate 2). The checkerboard tests indicate that the vertical resolving lengths are of the order of 200 km or less in the upper mantle, so that it is unlikely that depth extent of the upper mantle anomalies, which persist well into the transition zone, is the result of vertical smearing of, say, lithospheric heterogeneities.

In Appendix B, we have examined the statistical significance of various features in the TH2 model using the posterior covariance matrix for the model perturbation available from the Bayesian analysis. The results for the 10 regions of Figure B1 are summarized in Table B1. The five regions of high and low velocity in the upper mantle between the northern end of the Tonga trench and Oahu (regions 1 to 5) have high variance reductions (>94%), and each is statistically significant from zero at the 90% confidence level. Other features have lower variance reductions and larger correlations with other model parameters, indicating that their statistical significance is lower. One example is a region of small positive topography on the 410 discontinuity near the center of the grid (region 9), where the mean amplitude (+3.6 km) is less than the posterior error (± 5.3 km).

5.5 Other Inversion Experiments

As noted above, TH2 satisfies the steep gradients in the $ScS_n - ScS_m$ times because the horizontal wavelength of the upper mantle variations is closely matched to the dominant $\Delta/3$ wavelength in the sensitivity kernels for the differential times. This coincidence raises the issue of whether the modeling procedure is biased in a way that amplifies the

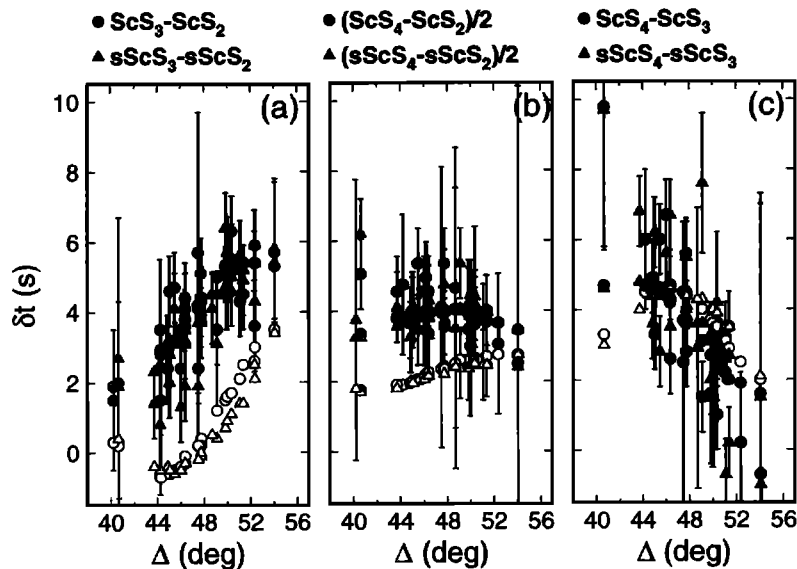


Figure 10. Plots of $ScS_n - ScS_m$ travel time residuals relative to the PA5/PREM reference model, comparing the observations (solid symbols with error bars, Figure 3) to those predicted by the TH2 model (shaded symbols) and the TH2.a model of Plate 4a (resulted from inverting only the turning and surface wave data, open symbols). The $ScS_4 - ScS_2$ residuals in Figure 10b have been divided by two to normalize them to a two-way time. The strong trend in the data is well predicted by both models. The constant baseline shift of the data relative to the prediction from TH2.a, which is discussed in the text, reflects an inaccurate path-averaged lower mantle which is not resolved by the turning wave data.

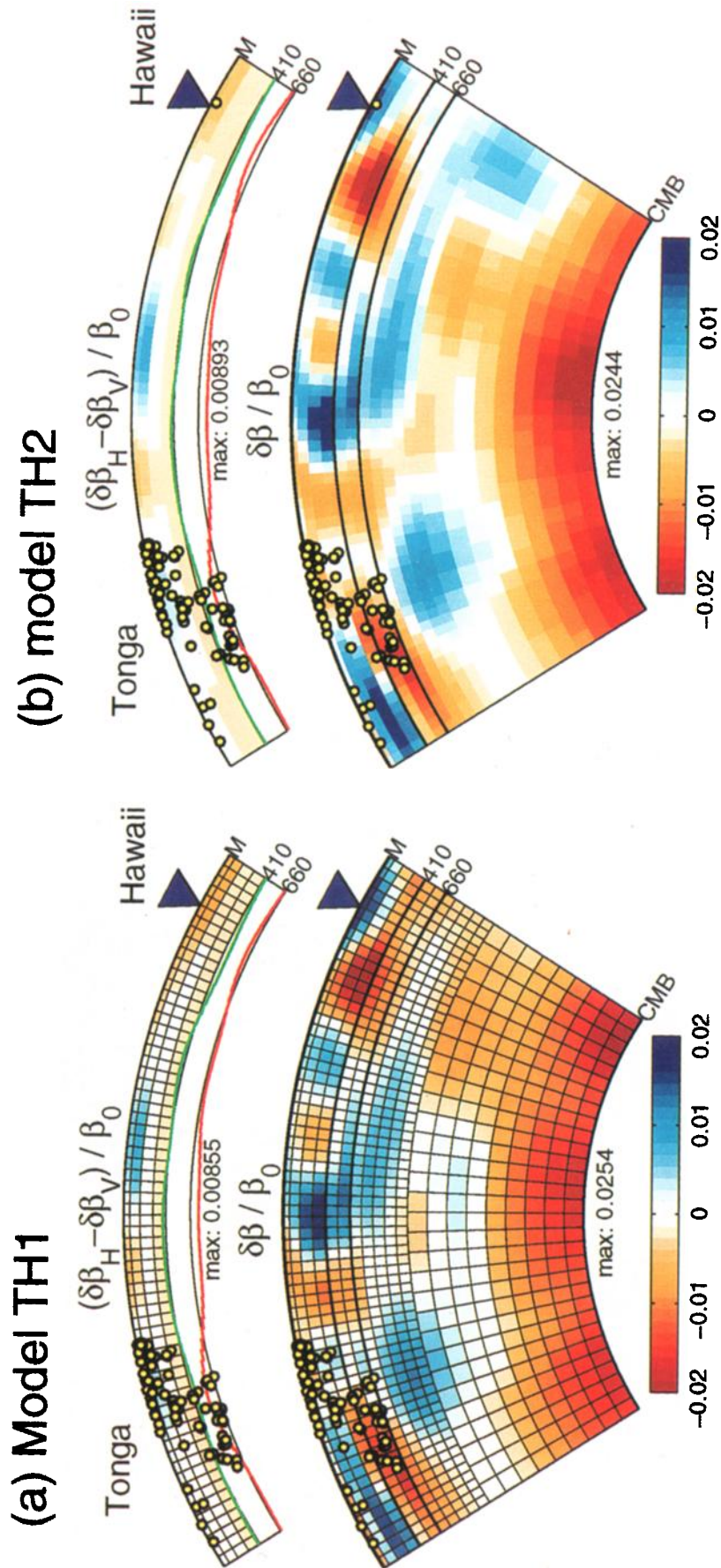


Plate 3. (a) Model TH1 of *Katzman et al.* [1997], shown over the grid that was used for all the inversions. (b) Model TH2 of this study. The two models were obtained by the same procedure, but the data set for the latter included the ScS_n times from a 1973 Hawaiian earthquake. The models are displayed as relative shear velocity perturbations to the PAS/PREM reference model in a cross section through the mantle from Tonga (left) to Hawaii (right). Bottom panel in each figure shows the relative perturbation in isotropic velocities extending from the Moho discontinuity (M) to the core-mantle boundary (CMB); negative perturbations are in red; positive are in blue. Top panels use same color scale to show the relative perturbation in radial anisotropy and green and red lines to represent the perturbations to 410 and 660 discontinuities, respectively (5 \times vertical exaggeration; the topographies are displayed more clearly in Figure 9c). Yellow circles are earthquakes used as sources; blue triangles mark locations of the receivers.

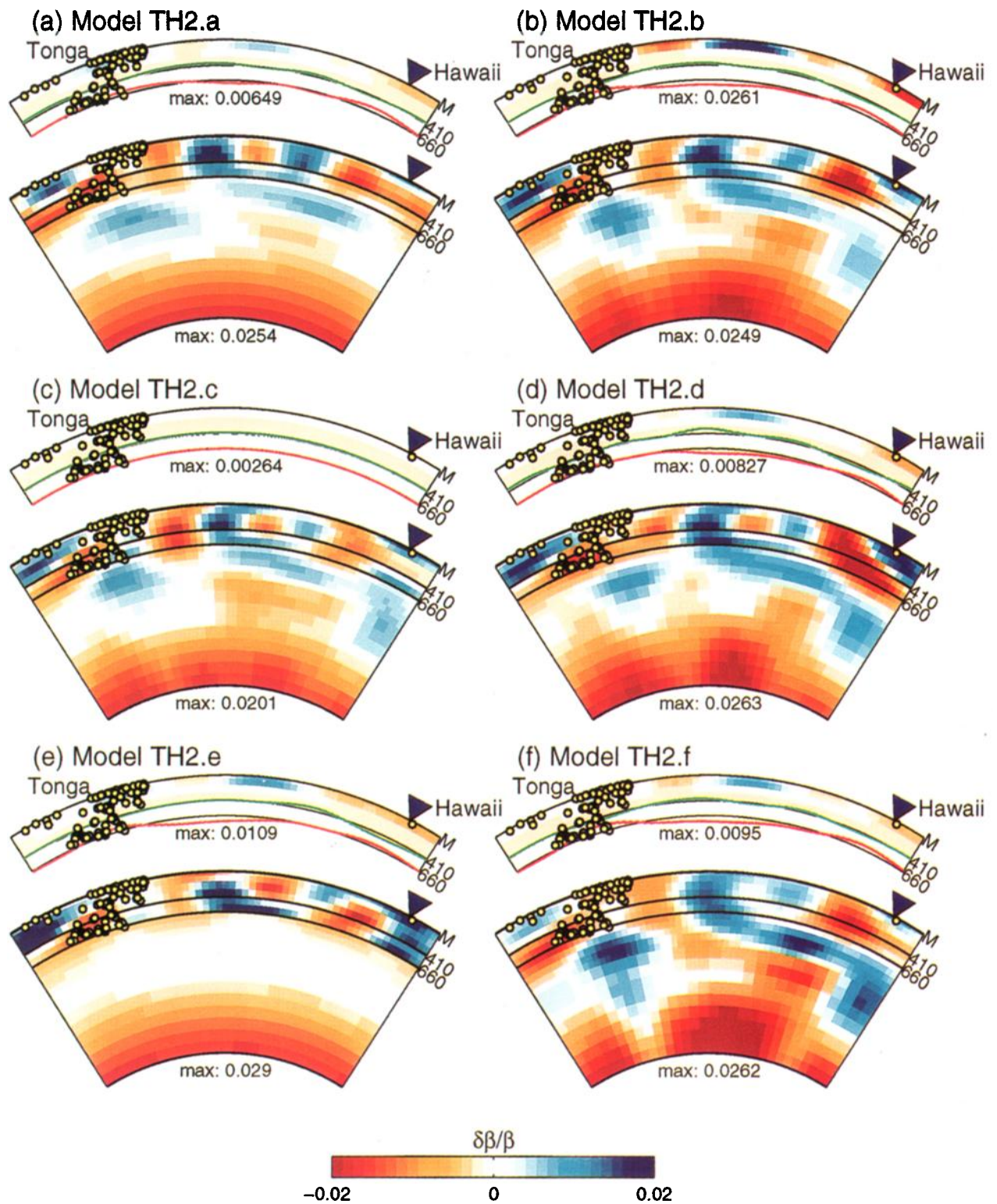


Plate 4. The models obtained from the data inversion tests summarized in Table 3. The models are displayed the same as in Plate 3, and their designated names are indicated at the top of each panel. (a) Model TH2.a, obtained from a 2-D inversion of only the surface and turning wave data. This model correctly predicts the trends in the multiple- ScS differential travel times (see Figure 10), although no ScS data were used to constrain its lateral variations. (b)-(f) Results from full data set inversions where the prior covariance matrix was modified, according to Table 3 and the text, by increasing the prior uncertainty for radial anisotropy in the uppermost mantle (model TH2.b); by completely suppressing the topographies on the 410 and 660 discontinuities and the anisotropic perturbations in the uppermost mantle (model TH2.c); by enforcing an equilibrium-olivine thermal model (model TH2.d); by reducing the lower-mantle prior uncertainty (model TH2.e); and by enforcing a uniform prior uncertainty for the whole mantle (model TH2.f).

heterogeneity at this wavelength over others that might be present in the upper mantle ("kernel resonance bias"). To evaluate this possibility, we excluded all of the ScS reverberation data from the data set and inverted only the phase delays of the surface and turning waves, obtaining a model designated TH2.a (Plate 4a), which depends on the ScS data only through the 1-D prior $\delta\bar{m}$ (taken to be the same in all inversions). The resulting tomogram is very similar to TH2, except beneath Hawaii, where TH2.a is poorly constrained by the reduced data set, which excludes the vertical ScS_n times from the Hawaiian earthquake. The upper mantle variations remain well defined; in fact, the amplitude of the 1500-km variation is increased slightly (Figure 9a). Except for a baseline shift due to the differences in lower mantle structure, TH2.a does almost as well as TH2 in satisfying the $ScS_n - ScS_m$ observations, despite the fact that they were not used in the inversions (Figure 10). Therefore the phase delays of the surface and turning waves independently corroborate the 1500-km variation indicated by the ScS_n data. Because the kernels for the former are distributed over a much wider range of horizontal wavelengths (Plate 2), we conclude that the kernel resonance bias is small.

Moreover, since the phase delays were measured from waves that turn in the upper half of the mantle and are completely insensitive to the lowermost mantle, they indicate that the contribution of the lowermost mantle to the $ScS_n - ScS_m$ trends is relatively minor. TH2 does display some lateral structure at the base of the mantle that may be significant, however: the shear velocities in the lowermost mantle are about 0.5% lower near the middle of the corridor, which slows the ScS_3 and ScS_4 phases relative to ScS_2 and accounts for the offsets between the TH2 and TH2.a predicted times in Figure 10. This feature is qualitatively consistent with the study of *Garnero and Helmberger* [1996].

More consistent, however, are the variations in the upper part of the lower mantle, such as the high-velocity region at 800-1400 km depth beneath the Tonga subduction zone, which appears in both TH2 and TH2.a and is dictated mostly by the times of the direct S phases. This feature corresponds to a region of high velocities seen in the P wave residual spheres from deep-focus Tonga earthquakes analyzed by *Fischer et al.* [1991]. They attribute this anomaly to the subduction of the Tonga slab, but this interpretation disagrees with the tomographic study by *van der Hilst* [1995], who puts the locus of the lower mantle slab anomalies farther to the west. We also note that such a feature is not evident in the global P wave model of *van der Hilst et al.* [1997]. The structure in this complex tectonic environment is no doubt highly three dimensional, and our 2-D model may be biased beneath Tonga by the inclined distribution of earthquakes transverse to the plane of the corridor. Within the source array, the perturbation to the average shear velocity in TH2, TH2.a, and all other models in Plate 4 varies from positive near the surface to negative in the transition zone, consistent with the notion that the rays from the shallow and intermediate-focus events sample the descending slab in the uppermost mantle and then penetrate low-velocity material underlying the slab in the transition zone. The 660 topography is elevated and the 410 topography is depressed in the region of low transition zone velocities in the manner expected from the equilibrium-olivine thermal model, despite the lack of any a priori correlation among these parameters imposed by the inversion. Lacking a fully 3-D inversion, however, we remain cautious about this interpretation.

We performed a number of additional inversions to test the sensitivity of the TH2 model to its Bayesian prior, five of which are shown in Plates 4b-4f. In each of these inversions, the full data set was inverted with the same 1-D prior $\delta\bar{m}$ as TH2, and only the parameters of the prior covariance \bar{C}_{mm} were modified. In the TH2.b inversion, the prior standard deviation for the radial anisotropy in the uppermost mantle was increased by a factor of 2 ($\bar{\sigma}_{AN} = 1\%$). The resulting anisotropic variation was larger, more than 3.5% peak-to-trough compared to 1.2% for TH2 (Figure 9b), but the basic features of the TH2 profile were preserved. In particular, the anisotropy perturbation peaks near the center of the corridor ($\theta = 38^\circ$) and declines to its minimum value near Oahu. This gradient is consistent with S20A, a radially anisotropic, 3-D global model complete to angular degree 20 [*Ekstrom and Dziewonski*, 1998], which shows a distinct minimum in $(\beta_H - \beta_V)/\beta_0$ in the center of the Pacific plate near Hawaii. The total variation in this parameter along the Tonga-Hawaii corridor in S20A is about 2.5%, larger than TH2 but smaller than TH2.b. TH2.b fits the data somewhat better than TH2 (Table 3), but an F test demonstrates that the decrease in χ^2/D from 1.41 to 1.38 is not significant at the 95% confidence level; that is, our data are consistent with the amplitude of the anisotropic heterogeneity in S20A. TH2 and TH2.b thus provide reasonable bounds on the variation of $(\beta_H - \beta_V)/\beta_0$ at horizontal wavelengths of 1000-3000 km. Moreover, the isotropic shear velocity perturbations (Figure 9a) and the discontinuity topographies (Figure 9c) are not at all sensitive to the magnitude of this anisotropy (see also Plate 7c, regions B and C).

In the TH2.c inversion, the topographies on the 410 and 660 discontinuities and the anisotropy perturbations in the uppermost mantle were completely suppressed by setting $\bar{\sigma}_{410}$, $\bar{\sigma}_{660}$, and $\bar{\sigma}_{AN}$ to zero. This restriction that the perturbation be isotropic and volumetric (which is typical of many previous tomographic studies) significantly increased the misfit of the data ($\chi^2/D = 1.53$), particularly the residuals of the first-order ScS reverberations that are most sensitive to the locations of the discontinuities. Again, however, this change in modeling assumptions did not substantially alter the isotropic shear velocity perturbations, demonstrating that any coupling of the latter to radial anisotropy and transition zone topographies was very weak (compare Plate 7c).

Similar topographies were recovered from all inversions in which the locations of the 410 and 660 discontinuities were allowed to vary independently along the corridor. The main feature is a broad depression of the 660 discontinuity toward the center of the profile, flanked by elevated regions beneath Tonga and Hawaii, with a peak-to-trough amplitude of just less than 40 km. The 410 discontinuity perturbation is a factor of 2 smaller and tends to be anticorrelated with 660 discontinuity. As indicated by the poor performance of TH2.c in fitting the ScS reverberation data, the times of the first-order reverberations dominated the determination of the transition zone topographies. This was expected, of course, given the sensitivity of these reflection measurements to discontinuity structure (Plate 1). We note, however, that the run which excluded all ScS data, TH2.a, gave the same basic structure, albeit lower in amplitude, showing that the phase delays of the waves turning in and near the transition zone are generally compatible with the reflection times. The depression of the 660 discontinuity between Tonga and Hawaii is correlated with higher shear velocities in the transition zone and uppermost part of the lower mantle, while its elevation near both ends of

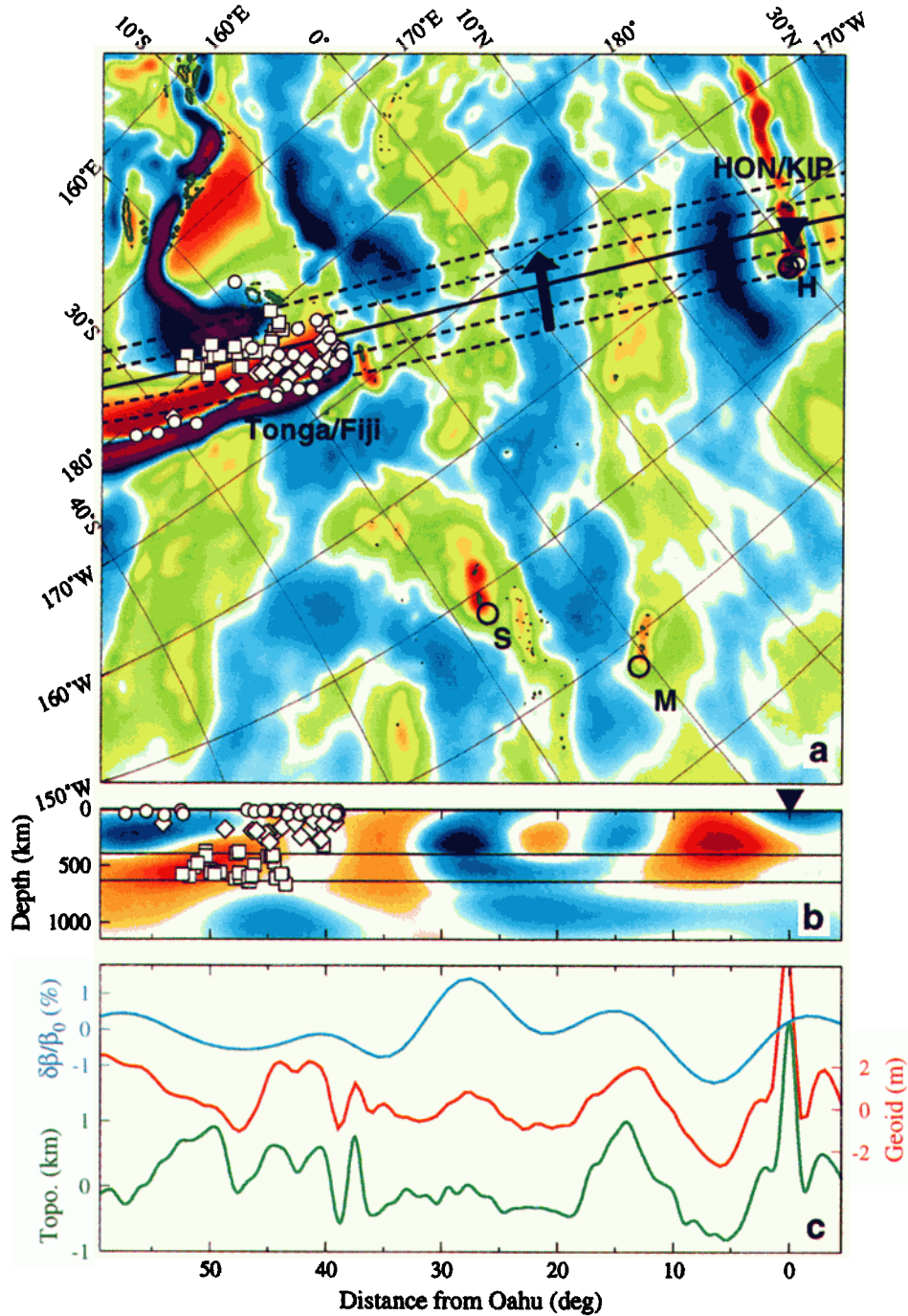


Plate 5. Comparison of shear velocity model with geoid and topography observations. (a) Oblique, rotated Mercator projection of the central south Pacific, showing the linear, NW trending geoid anomalies that correlate with the variations in the upper-mantle shear velocities (Plate 5b). The pole of the oblique Mercator projection is at 52°N, 84°W, and the map has been rotated clockwise by 90°. Geoid is the degree 360 NASA/DMA Joint Geopotential Model [Lemoine *et al.*, 1996], filtered to intermediate wavelengths by cosine tapering the spherical harmonic coefficients between degrees 15 and 20 and between degrees 80 and 360. White is zero anomaly; warm colors indicate positive anomalies (red > 2 m), cool colors negative anomalies (blue < -2 m). Large open circles show approximate locations of the Society Islands (S), Marquesas (M), and Hawaii (H) hotspots; arrow indicates Pacific plate motion in the hotspot reference frame [Gripp and Gordon, 1990], which is subparallel to the average trend of the geoid anomalies. Thick solid line is the axis of the Tonga-Hawaii corridor; earthquake and station symbols are the same as in Figure 1. (b) Top 1200 km of TH2, shown with the same color scale as in Plate 3. (c) Plot of shear velocity perturbation of TH2 averaged over the upper mantle (blue line), filtered geoid averaged over the five dashed and solid profiles in Plate 5a (red line), and seafloor topography band-pass filtered like the geoid and averaged over the same profiles (green line). Note the excellent positive correlation among these three profiles between the north end of the Tonga seismic zone and Hawaii.

the corridor is correlated with lower velocities, as predicted by the equilibrium-olivine thermal model.

In the TH2.d inversion, we enforced the equilibrium-olivine thermal model of the transition zone by specifying the prior correlation matrix according to the procedure described previously (Table 3). The resulting 410 discontinuity topography was somewhat larger in amplitude, and the 660 discontinuity topography was somewhat smaller than in TH2, but the difference between the two (the transition-zone thickness) has a similar along-path structure: a positive perturbation near the center ($25^\circ < \theta < 50^\circ$) and negative perturbations near the two ends (Figure 9c). The two discontinuities are anticorrelated, although not exactly, owing to their radial separation, which lowers the Gaussian factor (15). In particular, the 410 discontinuity topography mimics the harmonic upper mantle variation, which has a slightly larger amplitude in TH2.d than in TH2, while the 660 discontinuity correlates with the smoother variation of the shear velocities in the upper part of the lower mantle. We conclude that the data are entirely consistent with the thermal model. As noted above, however, this model ignores the garnet-to-perovskite phase change, which occurs at around 660 km depth with a positive Clapeyron slope [Weidner and Wang, 1998] and can potentially affect the depth and sharpness of the 660 discontinuity [Puster *et al.*, 1996]. Moreover, this correlation has not been observed in global studies of transition zone topographies [Shearer, 1993; Flanagan and Shearer, 1998]. For these reasons, we did not impose the thermal-correlation assumptions on our preferred model.

The last two experiments in Plate 4 were designed to examine the coupling between the upper and lower mantle. In TH2.e, we reduced the prior rms variability of the lower mantle by a factor of 5 ($\bar{\sigma}_{LM} = 0.1\%$), suppressing almost all of the heterogeneity below 660. A good fit was maintained for most of the data by amplifying the upper mantle heterogeneity. The average perturbation beneath Hawaii increased from 0.3% to 1.4%, for example (Figure 9a), as necessary to account for the data from the 1973 earthquake. The largest increase in χ^2 was for the direct S times, which, as we have seen, prefer a high-velocity zone in the lower mantle beneath northern Tonga. The dominance of the 1500-km harmonic pattern in $\delta\beta_{UM}$ remained, however, and the lateral variation in transition zone thickness was again similar to TH2.

In the other experiment (TH2.f), we equalized the prior variance for all isotropic variations in the mantle ($\bar{\sigma}_{UM} = \bar{\sigma}_{TZ} = \bar{\sigma}_{LM} = 1\%$). The rms amplitude of the lower mantle heterogeneity increased correspondingly, reaching 0.8% at 1500 km (compared to 0.4% for TH2), but the pattern of anomalies in both the upper and lower mantle was not substantially altered. Although $\delta\beta_{UM}$ became more positive near the center of the grid and smoother overall, the upper mantle variation remained large in amplitude and constant in phase (Figure 9a). The midmantle heterogeneity in TH2.f is strongest at horizontal wavelengths of the order of 2000-4000 km, corresponding to spherical harmonic degrees 8-15, which should be resolvable in global tomographic studies; however, the amplitudes of comparable features in global models [Su *et al.*, 1994; Masters *et al.*, 1996; Li and Romanowicz, 1996] are smaller by about a factor of 2. Moreover, despite its much larger lower mantle heterogeneity, TH2.f fits the data no better than TH2. We conclude that the amplification of the lower mantle structure in TH2.f simply reflects the poor resolving power of our data in this region and that TH2 is more realistic.

In addition to the inversion tests in Plate 4 and Figure 9, we performed a number of additional experiments (not shown) to test whether the lateral heterogeneity observed in TH2 can be confined only to the shallower part of upper mantle. In all these tests, the prior standard deviation for the isotropic parameters was suppressed to 0.1% below 170 km, and in some of the inversions, it was increased by a factor of 2 above 170 km. The observed trend of the $ScS_n - ScS_m$ times (Figure 3) was poorly satisfied by all the resulting models, although some of them had shallow upper mantle anomalies with more than twice the amplitude of the TH2 anomalies. In addition, the resulting data misfit increased significantly relative to that of TH2, especially for the SSS_v times; these data are particularly sensitive to the depth range between 200 and 450 km. The data thus imply that the upper mantle heterogeneity between Tonga and Hawaii extends well below 200 km.

6. Geodynamical Implications

The combination of data used in this study supplies substantially better horizontal and vertical resolution of upper mantle structure within the Tonga-Hawaii corridor than previous studies. As demonstrated by the series of inversions employing different data subsets and a variety of prior assumptions, the pattern of upper mantle anomalies exemplified in our preferred model TH2 is remarkably robust (Figure 9). The most striking and best resolved feature is an alternating series of highs and lows in $\delta\beta/\beta_0$ extending throughout the upper mantle with a horizontal wavelength of 1500 km and a peak-to-trough amplitude of about 3% (Figure 9a). There are only three basic mechanisms that can give rise to shear velocity heterogeneity of this magnitude: (1) temperature anomalies associated with convection [e.g., Hager and Clayton, 1989], (2) compositional inhomogeneities associated with the depletion of the oceanic upper mantle by basaltic volcanism [Green and Lieberman, 1976; Jordan, 1979; Phipps Morgan *et al.*, 1995], and (3) variations in the alignment of olivine crystals by mantle flow [Nicolas and Christensen, 1987; Ribe, 1989; Zhang and Karato, 1995].

The latter mechanism operates only in the upper 400 km of the mantle where olivine is a stable mineral phase. A detailed investigation by Gaherty *et al.* [1996] has shown that the average radial anisotropy within this corridor is largest in the upper 100 km and decreases to undetectable values (<1%) below about 170 km (Figure 2). Our inversion experiments indicate the presence of significant lateral heterogeneity in the apparent radial anisotropy above this depth (Figure 9b), with a magnitude consistent with the 3-D variations inferred for the Pacific by Ekström and Dziewonski [1998]. Moreover, they show that plausible errors in the magnitude and distribution of this radial anisotropy do not affect the estimates of the variations in isotropic upper mantle shear velocities (compare Figure 9a). The question of how the TH2 tomogram is affected by the unmodeled aspects of anisotropy, such as along-path variations in its azimuthal components, cannot be answered definitively in this 2-D study, but a consideration of this problem by Gaherty *et al.* [1996], based on the seafloor spreading history of the Pacific and some calculations by Kawasaki and Kon'no [1984] and Maupin [1985], suggests that any along-path variations in azimuthal anisotropy will tend to be absorbed into the radial anisotropy, and their effect on the isotropic velocity structure will be correspondingly small. We conclude that at the scales resolved in this study, the anisotropic heterogeneity of the Tonga-

Hawaii corridor is probably concentrated in the lithosphere and upper part of the low-velocity zone and that anisotropic effects associated with olivine alignment cannot account for the isotropic variations in TH2 and the other successful models of Plate 4. We shall therefore focus our discussion on the other two possible mechanisms for shear-wave heterogeneity: thermal convection and basaltic depletion.

6.1 Thermal Convection

Since basaltic depletion is thought to operate only in the mantle above 100-150 km [Ringwood, 1975; Liu and Chase, 1991], it has difficulty accounting for heterogeneities much below this depth. Thermal convection thus provides the most satisfactory explanation for the upper mantle anomaly pattern, which is organized into cell-like features with an aspect ratio near unity extending from the lithosphere to the 660 discontinuity. For a typical value of the thermal coefficient of shear velocity, $\partial\beta/\partial T = -0.5 \text{ m}\cdot\text{s}^{-1}\cdot\text{K}^{-1}$ [e.g., Creager and Jordan, 1986; Kato, 1997], the peak-to-trough temperature difference needed to explain the shear velocity anomalies would be $\sim 250 \text{ K}$, which is about the difference between the upgoing and downgoing limbs of upper mantle convection cells expected from simple boundary layer theory [e.g., Houseman and McKenzie, 1982].

The Tonga-Hawaii corridor is oriented nearly perpendicular to the direction of motion of the Pacific plate (Figure 1). Richter [1973] and Richter and Parsons [1975] have suggested that beneath the fast moving plates, convective instabilities will align themselves as rolls in the direction of absolute plate motion. While our 2-D study cannot constrain the mantle structure outside this corridor, there are some indications that the upper mantle anomalies in TH2 are actually elongated features oriented in the direction of plate motion. For example, the large variation in ScS_n residuals observed along the Tonga-Hawaii corridor is not evident along paths parallel to the Pacific plate motion [Sipkin and Jordan, 1980a]. Additional evidence for this northwestward extension comes from the geoid and topography fields.

6.2 Correlation With Geoid Lineations and Hotspot Swells

The geoid anomalies in the central and eastern Pacific plate show lineated undulations oriented subparallel to the present-day absolute plate motion and perpendicular to our seismic corridor [Wessel *et al.*, 1994]. In the eastern Pacific, these lineations are observed over a wide spectrum of horizontal wavelengths, ranging from 200 to 1500 km [Haxby and Weissel, 1986; Baudry and Kroenke, 1991; Maia and Diamant, 1991; Cazenave *et al.*, 1992; Wessel *et al.*, 1994; Cazenave *et al.*, 1995], and they are positively correlated with residual topography [e.g., Cazenave *et al.*, 1992]. A number of these authors have considered the possibility that these features are an expression of roll-like convection (see also an earlier study by McKenzie *et al.* [1980]), but the paucity of seismic data in the eastern Pacific has thus far precluded a systematic study of their correlation with shear velocity heterogeneity in the upper mantle.

We have compared our shear velocity model with the geoid anomalies in the central Pacific derived from the new geopotential model developed to degree and order 360 by the NASA Goddard Space Flight Center (GSFC) and the U.S. Defense Mapping Agency (DMA) [Lemoine *et al.*, 1996]. Long-wavelength features associated with deep mantle processes dominate the raw geoid and must be suppressed to

exhibit structures at intermediate wavelengths. We removed the geoid components below degree and order 15 and tapered the field between degrees 15 and 20 with a Hanning function (cosine-squared taper) to avoid Gibbs oscillations at the cutoff wavelength, and we similarly tapered the short-wavelength anomalies between degrees 80 and 360. Band-pass filtering of the red geoid spectrum is notoriously sensitive to the filter parameters [e.g., Sandwell and Renkin, 1988], so we experimented carefully with a number of filters. The particular parameters we adopted gave a good correlation between the filtered geoid and the seafloor topography, which has a much whiter spectrum and is not sensitive to the form of the filter. Along the Tonga-Hawaii corridor, these two quantities show a high coherence with an admittance of $3.3 \text{ m}\cdot\text{km}^{-1}$ (Plate 5c), which agrees with values observed previously for intermediate-scale features in this part of the Pacific [Crough and Jarrard, 1981; Sandwell and Renkin, 1988].

The resulting geoid represents the signature of upper mantle mass anomalies with horizontal wavelengths of 500-2000 km. In this band, the dominant features are a series of ridges and troughs oriented subparallel to the absolute plate motion (Plate 5a). Each of the three prominent ridges extends downstream from a major hotspot: the Hawaiian swell [Watts, 1976; Detrick and Crough, 1978], the Marquesas-Line swell [Crough and Jarrard, 1981], and the less conspicuous extension of the Society Islands swell through the Manihiki Plateau into the Phoenix Island region. Between the Tonga trench and Hawaii, where our seismic corridor cuts across these features, we observe a strong positive correlation between geoid height, seafloor topography, and upper mantle shear velocity (Plate 5). The hotspot swells are therefore positioned above high seismic velocities; in a convection scenario, the latter correspond to low-temperature downwellings.

The superposition of swells over apparent downwellings is dynamically puzzling. As shown in Appendix C, the positive correlation between geoid highs and temperature lows can be explained by a dynamic compensation mechanism [Hager and Clayton, 1989], provided the viscosity profile includes an asthenospheric low-viscosity channel (LVC). These calculations account for the finite elastic thickness of the lithosphere, which has a minor effect at these wavelengths (Figure C1), and they provide plausible viscosities for the asthenospheric LVC, $\sim 3 \times 10^{19} \text{ Pa}\cdot\text{s}$ for a lower mantle viscosity of $10^{22} \text{ Pa}\cdot\text{s}$ (Figures C2 and C3). Unfortunately, this dynamic compensation model fails regardless of the viscosity structure, because it always predicts negative dynamic topography over downwellings, while the observed topography for both the Hawaiian and Marquesas-Line swell is distinctly positive, as their names imply (Plate 5c).

An alternative is to delaminate the lithosphere at the hotspot; if η_{LVC} is low enough, the positive buoyancy of the hot replacement mantle can dominate the topographic response [Richards *et al.*, 1988], while the cold delaminated material can contribute to the deeper, high shear velocities. The high temperatures postulated by this mechanism are inconsistent with the high shear velocities found at shallow depths beneath all three swells in TH2, however (Plate 5), and the depth variation expected from this primarily vertical transfer (low velocities over high) is not observed. Given the good vertical and lateral resolving power of the TH2 data set (Appendix A), we must discount this possibility. It therefore appears that while thermal convection can account for the seismic results, it cannot explain the positive topography of the swells, which require a shallow source of buoyancy.

6.3. Need for Basaltic Depletion

The most obvious way to generate a buoyant, high-velocity mantle is by basaltic differentiation. The removal of basaltic constituents lowers the Fe/Mg and Al/Mg ratios of the peridotitic source rock, creating a refractory residuum of lower density [O'Hara, 1975; Green and Liebermann, 1976]. Jordan [1979] quantified this effect for a range of peridotitic compositions and proposed that the buoyancy of this residuum could contribute significantly to the positive topography and geoid of hotspot swells. Sipkin and Jordan [1980b] invoked this chemical differentiation mechanism to explain their observations that multiple-ScS waves on a Hawaii-to-Oahu path were faster (by 3 ± 1 s) and less attenuated ($Q_{s,cS} = 184 \pm 48$ vs. 141 ± 16) than the average for the Tonga-Hawaii corridor. Subsequent studies have shown that the Hawaiian swell does not display the anomalies in either heat flow [Von Herzen et al., 1989] or Rayleigh wave dispersion [Woods et al., 1991; Woods and Okal, 1996] expected if it had a strictly thermal origin [Detrick and Crough, 1978; Crough, 1983]. The weight of this evidence motivated Phipps Morgan et al. [1995] to examine the effects of chemical differentiation from a dynamical perspective, and they demonstrated that the accumulation and subsequent dispersal of basalt-depleted material at the base of the lithosphere could plausibly account for most of the swell topography and geoid.

While basaltic depletion increases the shear velocity of peridotites by only a small amount at ordinary temperatures [Jordan, 1979], this effect could be substantially amplified at temperatures close to the mantle solidus [Sato et al., 1989; Karato, 1995] and thus easily explains the 2-3% velocity anomalies we observe at shallow depths within the Tonga-Hawaii corridor. However, it does not seem possible for this mechanism to operate much below 150-200 km. The calculations of Phipps Morgan et al. [1995] are instructive in this regard. The extra crustal area across the Hawaiian chain is, on average, about 12.5 km thick and 200 km wide; assuming 5% partial melting, the mantle source region would have a cross-sectional area of $\sim 5 \times 10^4$ km². Therefore, distributed over the 1000-km-wide Hawaiian swell, the thickness of the low-density depleted root would be of the order of 50 km. Concentrating the depleted residuum in a narrower zone could increase this depth, perhaps by as much as a factor of 2, but it seems highly unlikely that it could account for the depth of the high-velocity anomalies in the TH2 upper mantle, which peak near 350 km and extend down into the transition zone.

6.4. Relationship to Hotspots

These considerations suggest that neither thermal convection nor chemical differentiation can alone satisfactorily account for the unusual configuration of the upper mantle in this part of the Pacific, and we infer that some combination of the two is probably required [Katzman et al., 1997]. The cell-like pattern of shear velocity anomalies in Plate 5b has a horizontal and vertical scale consistent with a convection system confined to the upper mantle, with its base regulated by the endothermic phase change at 660 km, as discussed by Mathetel and Weber [1991] and several other authors [e.g., Honda et al., 1993; Tackley et al., 1993; Solheim and Peltier, 1994], and/or a viscosity increase at the top of the lower mantle, as proposed by Hager and his colleagues [Hager, 1984; Hager and Richards, 1989; Hager and Clayton, 1989]. The 3-D structure of this convecting system

is likely to be complicated and will have to be clarified by an extension of high-resolution tomographic imaging to three dimensions (which is underway), but several lines of evidence point to the existence of roll-like convection parallel or subparallel to the absolute plate motion, including the theoretical work of Richter and Parsons [1975], the multiple-ScS study of Sipkin and Jordan [1980a], and the geoid lineations evident in Plate 5 and other analyses of the geopotential [Wessel et al., 1994; Cazenave et al., 1995, 1996].

One of the most puzzling aspects of our results is the strong positive correlation of the shear velocity variations with the geoid and topography, which implies that the hotspot swells overlie regions of mantle downwelling, at least along the Tonga-Hawaii corridor. The association of hotspot swells with convective downwellings does not imply that the hotspots themselves are sites of downwelling. Indeed, the high rate of localized, midplate volcanism observed at these Pacific hotspots requires that they be the sites of active mantle upwellings, i.e., plumes. Based on our results along the Tonga-Hawaii corridor, we cannot exclude, for example, the existence of a narrow plume (~ 100 km radius) right beneath Hawaii (3° away from our seismic stations on Oahu). The source depth of these plumes, however, is poorly constrained. If our results are taken at face value, then it would appear that they are features whose locations are controlled by a shallow system of upper mantle flow, rather than instabilities in the lowermost mantle as suggested by Morgan [1972] and others.

We can imagine, for example, a nearly steady state situation where the cooling oceanic thermal boundary layer becomes convectively unstable [Parsons and McKenzie, 1978] and feeds a secondary system of plate-aligned convective rolls, with a unit aspect ratio which are confined above the 660 discontinuity. In this hypothetical picture, the major hotspots of the Hawaiian, Marquesas, and Society Islands occur upstream from the convective downwellings, perhaps above strong plumes. These plumes could be generated by a counterflow in advance of the most intense areas of delamination, where the flow structures are expected to be highly three dimensional. The high-velocity, viscous residuum of hotspot volcanism is transported downstream with the overriding plate and is rafted into the axes of the downwellings by the horizontal flow at the base of the plates, maintaining the swells over downwellings and further stabilizing the roll structures. In this model, the high-velocity anomalies beneath the swells are dictated, at the shallower depths, by the low-density residuum which also supports the swell, and, at the deeper depths, by the cold downwelling.

The upper mantle convection hypothesized here is a secondary system, driven by the flux of negative buoyancy from the cooling Pacific plate, which itself participates in the primary, plate tectonic flow balanced through deep mantle circulation. We note that the part of the Pacific sampled in this study corresponds to Menard's [1984] Darwin Rise, a region of anomalously high residual topography [Davies and Pribac, 1993], where this type of secondary upper mantle flow may have been particularly active since the Cretaceous. Until further seismological investigations confirm the peculiar structural relationships in Plate 5, the dynamical speculations offered here must be viewed with caution. It is unlikely, however, that the location of the Hawaiian, Marquesas, and Society Islands hotspots along the axes of features with a geometry clearly controlled by upper mantle processes is

coincidental, as would be implied from *Morgan's* [1972] hypothesis that they are the surface manifestations of deep mantle plumes. Finally, we wish to emphasize that the conclusions we have drawn from the discussion of these three central Pacific hotspots do not apply to hotspots in general, such as those on slow moving younger oceanic plates.

7. Conclusions

We have derived a high-resolution tomographic model for the average 2-D structure in the plane of the Tonga Hawaii corridor, an oceanic region where previous knowledge of mantle heterogeneity has been limited by its lack of stations and its distance from source regions. The model, TH2 (Plate 3b), was obtained from a new tomographic technique which does not require multiple crossing paths and can deliver high resolving power even for single seismic corridors. It was obtained by satisfying a rich suite of seismological data (Table 2) that included frequency-dependent travel times from *P-SV* and *SH* polarized surface waves, body waves, and guided waves combined with band-limited travel times of zeroth- and first-order *ScS* reverberations. The model includes topography of the 410- and 660-km discontinuities and heterogeneity in radial anisotropy of the uppermost mantle, relative to a PA5 upper mantle (Figure 2) and a PREM lower mantle.

The primary feature of TH2 is a series of highs and lows in the upper mantle shear velocities, between the northern end of the Tonga trench and Hawaii, which generates the impressive trend in the $ScS_n - ScS_m$ differential travel times (Figure 3) but is required independently by the surface and turning wave data (Plate 4a and Figure 10). The robustness of this upper mantle heterogeneity was substantiated by a series of data inversions (Plates 4b-4f and Figure 9), which indicated that uncertainties in lower mantle heterogeneity, transition zone topographies, and radial anisotropy do not significantly affect the estimates of isotropic upper mantle shear velocities. It was shown that some radial anisotropic heterogeneity is concentrated in the uppermost mantle but cannot account for the isotropic variations in TH2. The 410 and 660 discontinuity topographies, albeit being more susceptible to data errors, were predominantly anticorrelated in all the inversion tests (Figure 9c), and the data were surprisingly consistent with an equilibrium-olivine thermal model.

The upper mantle velocity anomalies in TH2, which exhibit a horizontal wavelength of 1500 km and an upper mantle thickness, are strongly correlated with the topography and geoid anomalies associated with three central Pacific hotspot swells (Plate 5). The locations of these midplate hotspots along the axes of linear topography and geoid anomalies, which are also very dominant at wavelengths corresponding to upper mantle convection scale (~1500 km), suggest that they are controlled by upper mantle processes.

This study is the first 2-D application of a new tomographic technique. We believe that the resolving power of this technique will be dramatically increased by incorporating multiple crossing paths into a 3-D inversion. In the Pacific, such a 3-D study should help to clarify the structure outside the Tonga-Hawaii corridor and beneath the Society, Marquesas and Hawaiian islands; it may also provide a more direct evidence for (or against) the relationship between midplate hotspots and upper mantle circulation in the central Pacific.

Appendix A: Resolution Tests

In this appendix, we perform a simple sensitivity analysis by a series of resolution tests; we invert synthetic data calculated for various of test models, using the same procedure and parameterization as in the inversion of the real data, and observe how well these models are reproduced. Gaussian noise with standard deviations similar to our estimates for the real data (up to ~8 s) is added to the synthetic data prior to all the inversions. This procedure does not provide a complete resolution analysis, but it does give some useful basis for interpreting the final model by revealing areas of higher and lower sensitivity and primary model tradeoffs. We emphasize, however, that this type of resolution analysis, commonly used in tomographic studies, does not test inaccuracies in the forward theory, such as nonlinear wave propagation effects; it assumes that the errors in the data are not correlated; and it depends on the prior model parameterization. Plate 6 shows some examples of the input and recovered models, plotted with the same color scale as TH2 and the other models in Plates 3 and 4.

To estimate the effect of random errors on the final model, we invert a series of data sets with random travel time residuals and compare the magnitudes of the anomalies in the resulting models with those in the TH2 model. The models resulted from inversions of several random number realizations showed maximum perturbation of about 0.9%, 0.3%, and 10 km for isotropic velocities, anisotropic velocities, and transition zone topographies, respectively (e.g., Plate 6a). The maximum isotropic velocity perturbations at each depth in Plate 6a are smaller than in TH2 by at least a factor of 3, and the rms variation in the upper mantle is 4 times smaller, implying that isotropic velocities in TH2 are not strongly biased by random errors in the data. The same conclusion holds for radial anisotropic heterogeneity in the uppermost mantle. The transition zone topographies, on the other hand, are more affected by random errors; while the rms variation of the 660 discontinuity topography in Plate 6a is about 3 times smaller than in TH2, the variation on the 410 discontinuity topography is nearly the same. The transition zone topographies in TH2 should therefore be interpreted with caution.

The recovery of actual mantle heterogeneities is assessed through a series of synthetic data inversions. In order to test the potential recovery of different features in TH2 we inverted the data residuals that are predicted by this model (after adding the Gaussian noise). The recovered model is shown in Plate 6b and should be directly compared with Plate 3b. Most of the structural features in TH2 remain in this second inversion. The high- and low-velocity anomalies in the upper mantle between the northern end of Tonga and Hawaii are reconstructed with similar magnitudes and almost no smearing. The other features, however, are not as well reproduced, and their magnitudes are underestimated by up to a factor of 3, as, for example, the radial anisotropic anomalies or some of the lower mantle velocity anomalies.

The same behavior is observed in a series of checkerboard inversions. Plates 6c and 6e show examples of input models with harmonic variation in isotropic shear velocities at two different wavelengths and no perturbation in radial anisotropy or transition zone topographies. The velocity perturbation has peak-to-trough amplitude of 4% in the uppermost mantle

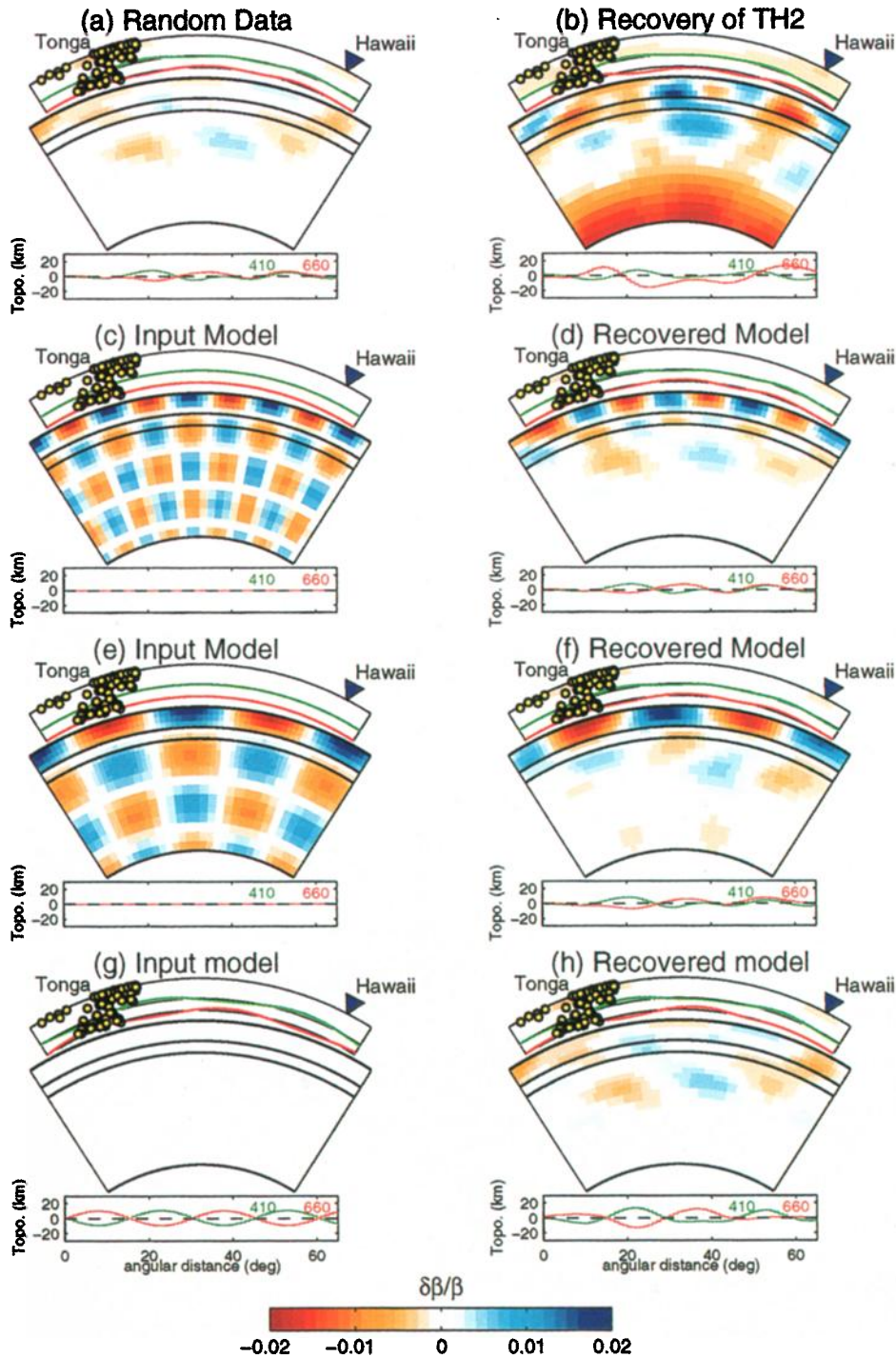


Plate 6. Examples of resolution tests. Each of the models is displayed in the same way as the TH2 model in Plate 3, but an additional panel is used for displaying the topography on the 410 (green line) and 660 (red line) discontinuities. Output models were obtained by a joint inversion, identical to TH2. In all the examples, synthetic data were generated by adding (the same) realistic Gaussian noise to phase delays computed from the input models. (a) Output model obtained by inverting Gaussian noise only. (b) Output model from an inversion of the data residuals predicted by TH2 (Plate 3b). (c) and (e) Input models with harmonic variation in isotropic shear velocities, having a horizontal and vertical wavelengths of 15° and 1500 km (Plate 6c) and 30° and 2000 km (Plate 6e). The perturbation in both models has a peak-to-trough amplitude of 4% in the uppermost mantle, which decays to 2% below 410 km, but no perturbation in radial anisotropy or discontinuity depths. (d) and (f) Output models resulted from inverting the data residuals predicted by the input models in Plates 6c and 6e, respectively. (g) Input model with topographic variations on the 410- and 660-km discontinuities. The perturbation has a horizontal wavelength of 30° and a peak-to-trough amplitude of 10 km but no perturbation in shear velocities. (h) The model recovered by inverting the data residuals predicted by the input model in Plate 6g.

which decays to 2% below the 410 discontinuity. The recovered models for both the short- and the long-wavelength examples (Plates 6d and 6f, respectively) show an excellent resolving power for upper mantle isotropic velocities; in particular, the inversion recovers the reversal in the sign of the anomalies at about 350 km in Plate 6d and at about 500 km in Plate 6f, demonstrating a good vertical resolution. However, the resolution degrades in the upper part of the lower mantle, below the 660 discontinuity; at this depth, only large features can be partially recovered, as seen in Plate 6b. At depths that are below 1200 km or below the turning point of the S waves, most of the lateral resolution is lost because the turning wave data do not sample this region and the ScS reverberations data alone cannot provide sufficient lateral resolution.

The two inversion experiments in Plates 6c-6f also demonstrate that isotropic velocity variation is not mapped into radial anisotropic heterogeneity or into topographic variations. The unwanted topography variation in Plates 6d and 6f is entirely due to the large uncertainties in the data that control the discontinuities (simulated by the large random errors for the first-order reverberations) and does not reflect any trade-offs between velocity and topography parameters. This can be seen from the nearly identical topography variation in Plate 6a, which was obtained by inverting pure Gaussian noise, with the same random-number realization. This conclusion is substantiated in the next example, where we invert the synthetic data computed from a model containing only topography variation, with no perturbation in velocity (Plate 6g). The anticorrelated topography pattern in the input model is well observed in the recovered model (Plate 6h) despite the small magnitude of the input topographies (maximum perturbation of 10 km). The velocity anomalies are small and are mostly due to the random noise that was added to the synthetic data.

We conclude that the upper mantle isotropic velocities are the best resolved parameters in TH2, with horizontal and vertical resolving lengths of about 500 and 200 km or less, respectively. Radial anisotropy in the uppermost mantle is resolvable but may be underestimated by a factor of 2-3. The resolution in the upper part of the lower mantle is quite limited, and only structures with dimensions of 1000 km or more and perturbation larger than 1% can be partially recovered. The transition zone topographies are biased by errors in the data, but long-wavelength patterns are resolvable. Trade-offs between parameters of different type are very small.

Appendix B: Resolving-Power Calculations Using Prior and Posterior Covariance Matrices

The prior correlation matrix $\bar{\rho}$ is a normalized version of the prior covariance matrix \bar{C}_{mm} , and its elements

$$\bar{\rho}(i, j) = \frac{\bar{C}_{mm}(i, j)}{\sqrt{\bar{C}_{mm}(i, i)\bar{C}_{mm}(j, j)}} \quad (\text{B1})$$

specify the correlations between the prior uncertainties of the i th and the j th parameters (15), loosely referred to here as the "smoothness constraint" (for $i \neq j$). Plate 7a shows a color image of $\bar{\rho}$ for the 1375 model parameters of TH2. When interpreting the images in Plate 7, it is important to remember that the serial number of the model parameters increases

fastest horizontally; as a result, the distance between the i th and the j th parameter wraps around every $i - j = N_d$ blocks, where N_d is the number of blocks at each depth layer. The deviation of $\bar{\rho}$ from a unit matrix is entirely due to the smoothness constraint. The width of each individual diagonal feature in Plate 7a is proportional to the horizontal correlation length l_θ in (15), whereas the width of the global pattern is proportional to the vertical correlation length l_v . The correlation lengths are the same for the entire mantle, but the pattern become narrower for the lower mantle below 1200 km because the blocks (parameters with serial numbers 716 to 985) are larger. The zero correlations outside the three squares in Plate 7a imply that no prior correlation was imposed between isotropic and anisotropic velocity parameters or between velocity and topography parameters. Plate 7a also shows that no prior correlation was imposed between the two discontinuities.

Parameters that are well resolved in TH2 will show small posterior uncertainties relative to their prior uncertainties, i.e., large variance reduction. We define the matrix $\tilde{\rho}$ as the posterior covariance matrix (12) normalized by the diagonal terms of the prior covariance matrix, i.e.,

$$\tilde{\rho}(i, j) = \frac{C_{mm}(i, j)}{\sqrt{\bar{C}_{mm}(i, i)\bar{C}_{mm}(j, j)}} \quad (\text{B2})$$

(Plate 7b). The diagonal terms of this matrix, $\tilde{\rho}(i, i) = \sigma^2(i) / \bar{\sigma}^2(i)$, are the ratios between the posterior and prior variances of the model parameters. Plate 7b indicates that the best resolved parameters are the isotropic velocities in the upper mantle and the transition zone ($i \leq 390$) which show $\sigma^2(i) / \bar{\sigma}^2(i)$ of about 0.1 or variance reduction of 0.9. The variances for the upper part of the lower mantle ($391 \leq i \leq 585$) are also significantly reduced to about 30-45% of their prior values. The smallest variance reduction, $1 - \sigma^2(i) / \bar{\sigma}^2(i) = 0.1$, is observed for the lower mantle below 1200 km ($716 \leq i, j \leq 985$). The anisotropic parameters (middle square in Plate 7b), and the 410 and 660 discontinuity topographies (upper right square) show better variance reductions of about 0.35, 0.5, and 0.6, respectively.

Plate 7c shows the posterior correlation matrix ρ (13), which indicates how well two given model parameters are independently resolved by the inversion. A parameter that is independently resolvable will have off-diagonal terms with magnitude close to zero. The posterior correlation matrix, due to the normalization in (13), is +1 along the diagonal and gradually decreases to negative values greater than -1 away from this axis of symmetry. The global pattern associated with the smoothing constraint in Plate 7a is still dominant in Plate 7c, indicating that velocity perturbations on neighboring blocks are strongly affected by the prior smoothing and are not independently resolved by the data. Further examination, however, reveals small posterior correlations (and anticorrelations) between (1) upper mantle and midmantle isotropic velocities (region A), (2) anisotropic and isotropic velocities in the upper mantle (region B), and (3) isotropic velocities and transition zone topographies (region C). In all of these cases, the correlations are of order 0.2 or less, much smaller than the posterior correlations associated with the prior smoothing constraint. Finally, region D indicates that the posterior uncertainties for the 410 and the 660 discontinuities are neither correlated nor anticorrelated, implying that both discontinuities can be independently resolved by the inversion.

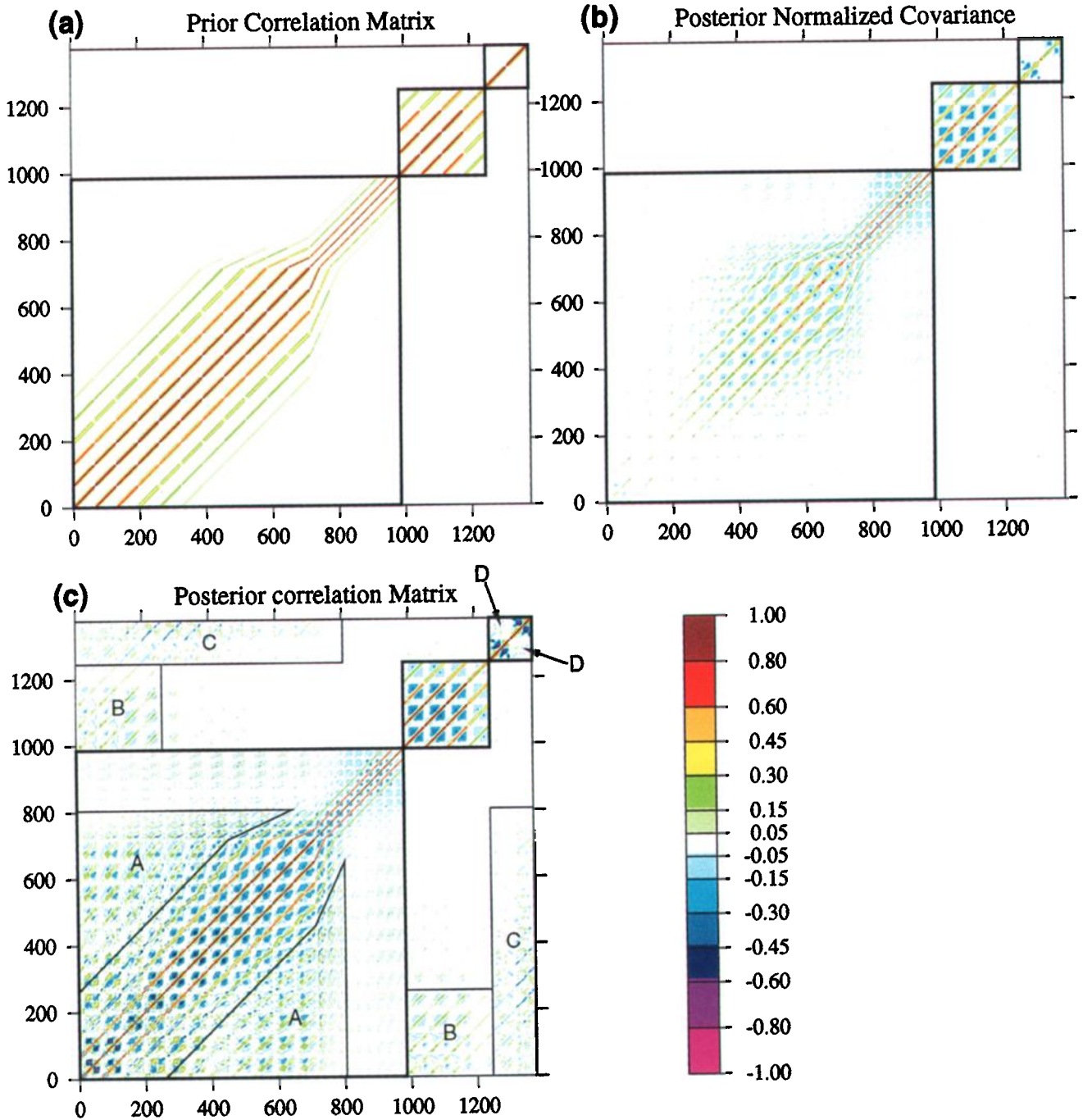


Plate 7. Color image of the elements of (a) the prior correlation matrix $\bar{\rho}(i,j)$, (b) the posterior, normalized covariance matrix $\tilde{\rho}(i,j)$, and (c) the posterior correlation matrix $\rho(i,j)$. The horizontal and vertical axes represent the serial number of the model parameters. The numbering starts from the top left cell and increases fastest horizontally; as a result, the distance between the i th and the j th model parameter wraps around every $i - j = N_d$ cells, where N_d is the number of cells at each depth layer. The global pattern becomes narrower for $716 \leq i, j \leq 985$ because in this interval, each mantle layer is sampled by only 30 instead of 65 cells (compare Plate 3a). The large, bold, lower left square bounds the 985 isotropic velocity parameters. The other two bold squares bound the anisotropy parameters ($i, j \in [986, 1245]$), and the topography parameters ($i, j \in [1246, 1375]$). Note the small values of the posterior, normalized covariance in Plate 7b for the isotropic velocities of the upper mantle and the transition zone ($i, j \leq 390$). The general morphology of these three matrices as well as specific features, like those marked by A, B, C, and D in the posterior correlation matrix, are discussed in the text.

Table B1. Standard Error Analysis for the Regions Shown in Figure B1

Region	Posterior Mean	Standard Deviation		Variance Reduction
		Posterior	Prior	
1	-0.69%	0.41%	1.87%	0.953
2	+1.64%	0.36%	1.84%	0.962
3	-0.45%	0.29%	1.87%	0.976
4	+0.58%	0.38%	1.87%	0.958
5	-1.82%	0.43%	1.84%	0.945
6	+0.49%	0.19%	0.32%	0.635
7	+1.01%	0.31%	0.46%	0.546
8	+0.68%	0.32%	0.44%	0.482
9	+3.63 km	5.26 km	8.37 km	0.604
10	-16.10 km	4.45 km	8.37 km	0.717

We examine the statistical significance of ten specific features in TH2 (Figure B1) by calculating their posterior mean, their prior and posterior uncertainties, and their variance reductions using (14). Table B1 summarizes the results for the 10 regions of Figure B1. As an example, consider the area of high upper mantle shear velocity near the center of the model grid (region 2), which has an integrated amplitude of 1.6%. The uncertainty for this integral computed from the prior distribution is about 1.8%, whereas its posterior uncertainty is less than 0.4%. In other words, the inversion sharpens the estimate from a prior value of 0% ±

1.8% to a posterior value of 1.6% ± 0.4%. An examination of the off-diagonal terms of the posterior correlation matrix (Plate 7c) shows that the cross correlation between this error and those for other regions is small, so that this particular feature is statistically significant at a very high confidence level. A similar conclusion can be drawn for the other four regions of high and low velocity in the upper mantle (regions 1 to 5); each of these regions is significantly different from zero at the 90% confidence level and they all have a variance reduction exceeding 94%. The other features in Plate 7 have lower variance reductions. For example, the area of increased anisotropy in the uppermost mantle near the center of the grid (region 8) shows variance reduction of less than 50%. However, the posterior estimate of this specific feature (0.68% ± 0.32%) indicates that it is statistically significant at the 90% confidence level; the small variance reduction in this case, simply reflects the small prior uncertainty imposed on the anisotropic parameters. In contrast, the region of small positive topography on the 410 discontinuity near the center of the grid (region 9) is not statistically significant at this high confidence level, as indicated by its large posterior uncertainty (5.6 km), which is larger than its mean amplitude (3.6 km).

On the whole, Plate 7 and Table B1 substantiate the conclusions from Appendix A that the best resolved model parameters in TH2 are the isotropic velocities above the 660 discontinuity. Lower mantle velocities below 1200 km are essentially unresolved, and only average quantities can be obtained. Large-scale anomalies in all the other parameters are at least partially resolvable, and coupling between model parameters of different type is weak.

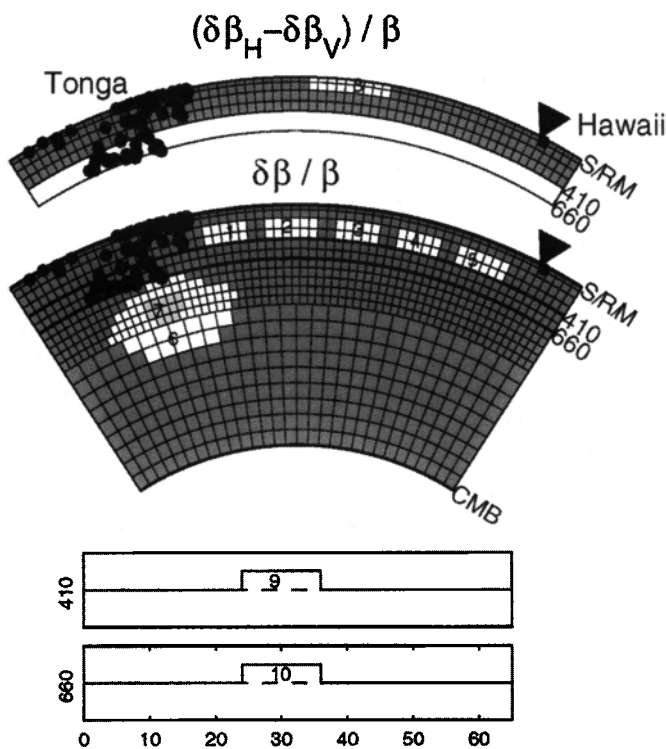


Figure B1. White areas are specific features whose individual prior and posterior standard are shown in Table B1. In TH2 (Plate 3b) regions 1, 3, and 5 represent low-velocity anomalies while regions 2 and 4 represent high-velocity anomalies within the upper mantle. Regions 6 and 7 (shaded area within region 6) represent the high lower mantle velocity anomaly below Tonga; region 8 represents the positive anisotropic anomaly in the middle of the corridor; and regions 9 and 10 represent the topographic high on the 410-km discontinuity and the topographic low on the 660-km discontinuity between angular distances of 24° and 35°.

Appendix C: Dynamic Compensation Models

We demonstrate here that the positive correlation between geoid highs of the swells and temperature lows (which are represented by the high upper mantle seismic velocities in TH2) can be explained by a dynamic compensation mechanism with a viscosity profile that includes a low-viscosity channel (LVC). It is important to emphasize, however, that the thermal convection models invoked in this appendix cannot explain the positive topography of the swells.

C1. Harmonic Analysis of Geoid and Velocity Anomalies

In order to obtain a dynamic model for the mantle which satisfies both the seismological and the gravitational potential data, we analyze the correlation between the seismic

velocities and the geoid anomalies around the dominant wavelength of the former. In all the calculations below, we have excluded the contribution from the 410 and 660 discontinuity topographies mostly because these parameters were more susceptible to errors in the seismic data (it was also found that their combined effect on the geoid is relatively small around the dominant wavelength of the analysis). We start by finding the harmonic degree and the phase that best fit the upper mantle velocity structure of TH2 in the interval $[\theta_1, \theta_2]$, by solving the following least squares problem:

$$\bar{\gamma}(\theta) = A_1 \cos[(l+1/2)\theta + \varphi] + A_2 \theta + A_3; \quad \theta_1 \leq \theta \leq \theta_2, \quad (C1)$$

where θ is the distance along the corridor measured from the station, $\bar{\gamma}(\theta) = \text{avg}(\delta\beta/\beta_0)$ is the relative velocity perturbation averaged over the upper mantle and the transition zone (blue line in Plate 5c), l is the harmonic degree, A_1 and φ are amplitude and phase factors, respectively, and A_2 and A_3 are variables to account for a linear trend and a constant deviation of $\bar{\gamma}$. An harmonic degree of $l=26$ provides the best fit to $\bar{\gamma}$. Using l and φ obtained from (C1) we compute the harmonic coefficients \bar{N}^l , $\bar{\gamma}^l$, and $\gamma^l(r)$ for the average profile of the filtered geoid along the corridor and for the depth-averaged and original velocity perturbations of TH2, respectively:

$$\begin{aligned} \bar{N}^l &= \int_{\theta_1}^{\theta_2} \bar{N}(\theta) b(\theta) d\theta, \\ \bar{\gamma}^l &= \int_{\theta_1}^{\theta_2} \bar{\gamma}(\theta) b(\theta) d\theta, \\ \gamma^l(r) &= \int_{\theta_1}^{\theta_2} \gamma(\theta, r) b(\theta) d\theta, \end{aligned} \quad (C2)$$

where $\bar{N}(\theta)$ is the average profile of the filtered geoid along the corridor (red line in Plate 5c), $\gamma(\theta, r) = \delta\beta/\beta_0$ is the velocity perturbation of TH2 at a distance θ from the station and radius r , and $b(\theta)$ is the basis function:

$$b(\theta) = \frac{\cos[(l+1/2)\theta + \varphi]}{\left[\int_{\theta_1}^{\theta_2} \cos^2[(l+1/2)\theta + \varphi] d\theta \right]^{1/2}}. \quad (C3)$$

The phase term φ both here and in (C1) depends on the fitting interval $[\theta_1, \theta_2]$, which was chosen to be $[5^\circ, 32^\circ]$ measured southwesterly from Hawaii. Using this interval, which avoids the Hawaiian islands and the Tonga subduction zone, we obtain $\bar{N}^l = 0.71$ and $\bar{\gamma}^l = 0.0042$. The correlation between the geoid and the upper mantle velocity perturbation, or the ratio $\bar{N}^l / \bar{\gamma}^l$, is therefore 170 ± 70 m (or 1.7 ± 0.7 m for each 1% of velocity perturbation; see Plate 5c). The uncertainty term was obtained from several tests, where we computed the correlation coefficient assuming different geoid-filter parameters and/or different fitting interval. We emphasize that this correlation was always positive and was unaffected by the parameterization to within an uncertainty of less than 50%.

C2. Dynamic Calculations of the Geoid and Constraints on Viscosity Structure

The surface dynamic topography and geoid anomaly can be calculated for a given wavelength using the corresponding kernels and the harmonic coefficients for the velocity perturbations as a function of depth, after assuming a distribution of viscosity with depth and a scaling relation between the relative density and velocity perturbations [Hager

and Clayton, 1989]. We also include the effect of an elastic lithosphere on the geoid kernels [Hager, 1991] by specifying a lithospheric viscosity that is high enough to prohibit tangential flow close to the surface and by modifying the dynamic topography. The former condition was satisfied by choosing a viscosity factor $\geq 3 \times 10^3$ between the lithosphere and the asthenosphere, whereas the latter condition was incorporated into the nondimensional geoid kernel as follows:

$$G'_e = G^l + H^l \left[\frac{1}{1 + Dk^4/\Delta\rho g} - 1 \right], \quad (C4)$$

where G^l and H^l are the original nondimensional geoid and surface topography kernels respectively [Hager and Clayton, 1989; Panasyuk et al., 1996], $k = (l+1/2)/R$ is the wave number, R is the Earth radius, $\Delta\rho$ is the density difference across the surface, g is the gravitational acceleration at the surface, and $D = ET_c^3/[12(1-\nu^2)]$ is the flexure rigidity of an elastic plate of thickness T_c , Young's modulus E , and Poisson's ratio ν [Turcotte and Schubert, 1982]. Equation (C4) states that the geoid at the surface is affected by the dynamic topography of an elastic lithosphere and not by the dynamic topography of a viscous upper layer with no flexural rigidity.

The harmonic coefficients of the geoid anomaly predicted at the surface from density perturbations $\delta\rho^l(r)$ situated within the upper 660 km of the mantle are

$$\tilde{N}^l = \frac{4\pi\Gamma R}{(2l+1)} \int_{r_{660}}^R \frac{G'_e(r) \delta\rho^l(r)}{g(r)} dr, \quad (C5)$$

where Γ is the gravity constant, r_{660} is the radius of the 660-km discontinuity, and $l=26$ is the harmonic degree of our analysis. The density perturbations are obtained from the relative velocity perturbation in TH2 using a constant scaling $\delta\rho/\rho = C_{\rho\beta} \delta\beta/\beta$. The conversion parameter, $C_{\rho\beta} = 0.2$, was obtained by assuming a thermal expansion coefficient of $3 \times 10^{-5} \text{ K}^{-1}$ and a thermal coefficient of shear velocity, $\partial\beta/\partial T = -0.5 \text{ m} \cdot \text{s}^{-1} \cdot \text{K}^{-1}$ [Creager and Jordan, 1986; Kato, 1997].

The observed geoid anomaly was compared to the geoid predicted from a series of viscosity models. The viscosity profiles were prescribed relative to the viscosity in the transition zone because the gravitational potential depends only on the viscosity contrasts but not on the absolute viscosities [Hager and Clayton, 1989]. As a starting model, we employ a modified version of the Hager and Clayton [1989] preferred viscosity structure (Figure C1a). The 3.5 order of magnitude viscosity jump from the lid to the asthenosphere implies that the lid viscosity in this model is effectively infinite. The high-viscosity lid is assumed to be bounded at its bottom by the sharp G discontinuity of PA5, at 68 km depth [Gaherty et al., 1996]. This viscosity profile also includes a low-viscosity asthenospheric channel with subasthenosphere viscosity, low enough to allow flow, and a high-viscosity lower mantle, which are all required in order to fit the global geoid observations [Hager, 1991]. Placing these viscosity jumps near the phase transitions at 400 and 670 km seems to be geophysically plausible [Sammis et al., 1977].

In a thermal convection model where $C_{\rho\beta} > 0$, the robust observation that the geoid anomaly is positively correlated with the upper mantle velocity perturbations around the dominant wavelength of ~ 1500 km ($l=26$) implies that the geoid kernel at this wavelength should be mostly positive. However, the geoid kernel for our starting viscosity model (solid line in Figure C1b) is, on average, strongly negative

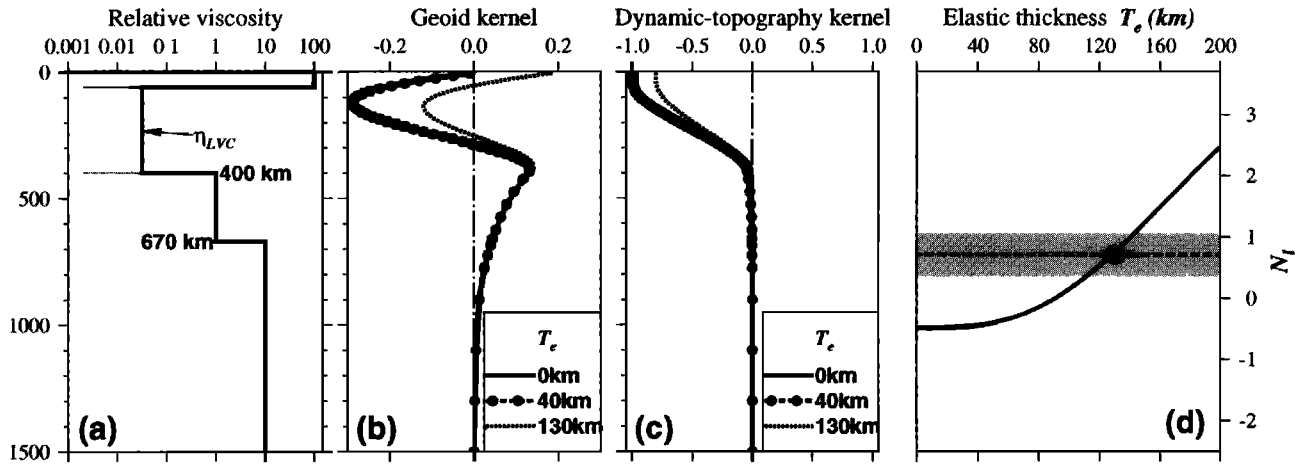


Figure C1. Effect of elastic thickness on the geoid. (a) Our initial viscosity model is modified from the preferred model of *Hager and Clayton* [1989]. It includes a 60-km-thick lid with viscosity a factor of 100 larger than the reference viscosity, an asthenospheric layer with viscosity a factor of 30 smaller than the reference viscosity, between depths of 60 and 400 km, and a lower mantle viscosity a factor of 10 larger than the reference viscosity. (b) and (c) Three geoid kernels and three dynamic topography kernels, respectively, which are calculated for $l=26$, using the viscosity model in Figure C1a, with a lithospheric elastic thickness of 0 km (heavy solid lines), 40 km (heavy dashed lines with dots), and 130 km (heavy dashed lines). The kernels for the lithospheric elastic thickness of 40 km (heavy dashed lines with dots) are almost identical to those with no elastic plate (heavy solid lines), suggesting that at this wavelength (~ 1500 km), the original kernel, which is strongly negative in the upper mantle, is not affected by adding an elastic plate of 40 km thick. (d) Solid line is the harmonic coefficient of the calculated geoid, \bar{N}'_l , for $l=26$, as a function of the elastic plate thickness; dashed line is the observed value, \bar{N}'_l , derived from the harmonic analysis described in the text; shaded zone represents the 50% uncertainty of the observed value. Note that a minimum elastic thickness of 90 km is needed in order to flip the sign of \bar{N}'_l and a thickness of ~ 130 km (dot) is required to fit the observed value.

because the gravitational effect from the surface boundary deformation (Figure C1c) overwhelms the effect from the driving density contrast. This geoid kernel predicts a negative geoid anomaly over the cold downwellings, i.e., $\bar{N}'_l < 0$,

which does not match the observed value of $\bar{N}'_l = 0.71$. One way to flip the sign of \bar{N}'_l is by adding the gravitational effect from the flexural rigidity of the lithosphere, which tends to decrease the surface dynamic topography and to make the

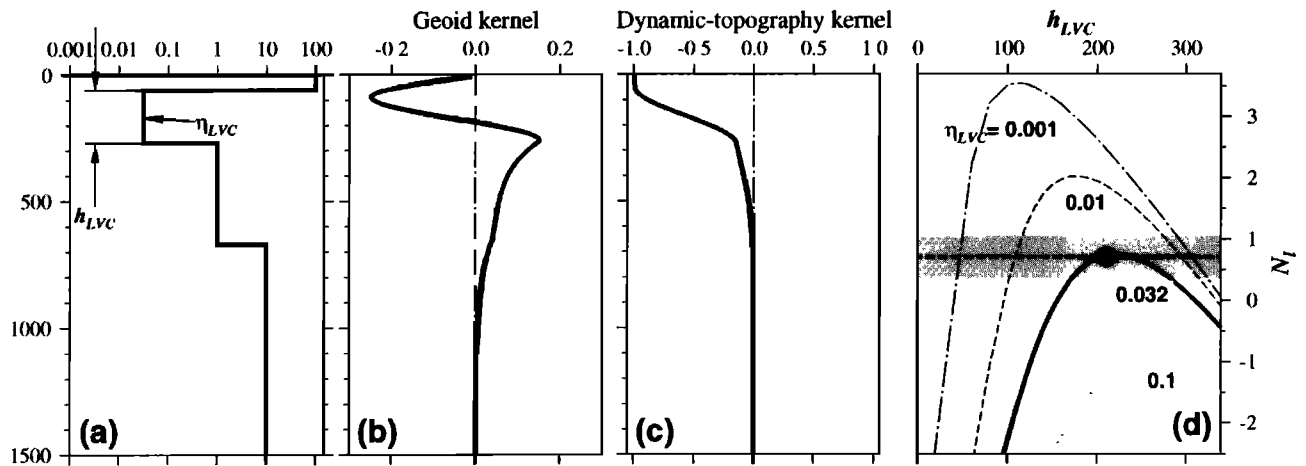


Figure C2. Effect of a low-viscosity channel (LVC) on the geoid. (a) A profile with viscosities similar to those in Figure C1a but with an asthenospheric LVC thickness of 210 km (instead of 340 km); the geoid computed with this viscosity profile fits the observed geoid around $l=26$. (b) and (c) Geoid and dynamic topography kernels, respectively, calculated for $l=26$, using the viscosity structure in Figure C2a. (d) Light lines and heavy solid line are the harmonic coefficient of the calculated geoid, \bar{N}'_l , for $l=26$, as a function of η_{LVC} and h_{LVC} defined in Figure C2a; heavy dashed line is the observed value, \bar{N}'_l , derived from the harmonic analysis described in the text; shaded zone represents the 50% uncertainty of the observed value. The intersection between the heavy solid line ($\eta_{LVC} = 0.32$) and the dashed line (dot) is the viscosity model shown in Figure C2a.

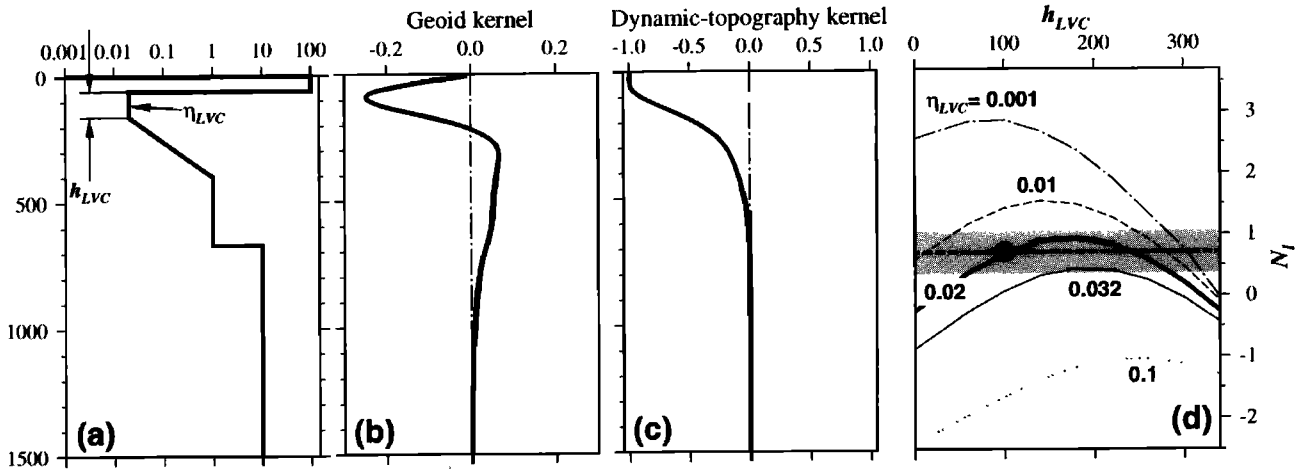


Figure C3. Effect of a LVC with gradational bottom on the geoid. (a) A viscosity profile, which mimics PA5 (Figure 2), with a low-viscosity asthenospheric channel below the seismic G discontinuity, bottomed by a linear increase in the logarithms of the viscosity that extends along the seismic high-gradient zone of PA5; the geoid computed with this viscosity profile fits the observed geoid around $l = 26$. (b) and (c) Geoid and dynamic topography kernels, respectively, calculated for $l = 26$, using the viscosity structure in Figure C3a. (d) Light lines and heavy solid line are the harmonic coefficient of the calculated geoid, N_l , for $l = 26$ as a function of η_{LVC} and h_{LVC} defined in Figure C3a; heavy dashed line is the observed value, N_l , derived from the harmonic analysis described in the text; shaded zone represents the 50% uncertainty of the observed value. The intersection between the heavy solid line ($\eta_{LVC} = 0.02$) and the dashed line (dot) is the viscosity model shown in Figure C3a.

overall geoid kernel more positive (C4). However, at wavelength of 1500 km, a 100 Ma lithosphere with an elastic plate thickness, T_e , of 30-40 km [Watts *et al.*, 1980; Watts and ten Brink, 1989] reduces the dynamic topography by less than 1% (dashed line with dots in Figure C1c) so that the change in the geoid kernel is negligible (Figure C1b). Figure C1d shows that we can flip the sign of N_l and fit the observed value only by choosing T_e of 90 and 130 km, respectively. Since these elastic thicknesses are 3-5 times larger than those expected for the Tonga-Hawaii corridor [Calmant, 1987], these particular models are ruled out.

An alternative way to fit the positive correlation between the geoid anomalies and the density distribution is by modifying the viscosity structure of the upper mantle (e.g., Figures C2a and C3a). It is easy to see that in order to obtain a geoid kernel which is mostly positive, one needs to invoke an LVC beneath the high-viscosity lid. The geoid kernels for a constant viscosity structure are always negative for all wavelengths because the gravitational effect from the boundary deformation overwhelms the effect from the driving density contrasts; adding a high-viscosity lid, which can support a larger surface deformation, will only make these kernels more negative [Hager and Clayton, 1989]. An LVC below the lid, on the other hand, decreases the coupling of the flow to the surface and increases the coupling to the CMB. The gravitational effect from the driving density contrast, in this case, becomes more dominant, and the resulting geoid kernel is less negative and can change sign (e.g., Figures C2b, and C3b). The geoid anomaly sign at a given wavelength (which is strongly influenced by the depth at which the kernel change its sign) is controlled by the viscosity, η_{LVC} , of the LVC and by its thickness, h_{LVC} (Figures C2d and C3d). If h_{LVC} is smaller than the thickness of the thermal boundary layer of the convecting cell, then the geoid kernel will be negative and not much affected by the channel [Robinson *et al.*, 1987]; on the

other hand, if h_{LVC} is too large, the kernel shape would tend to that of a conducting lid over a constant viscosity mantle and would become mostly negative again.

Following this rationale, the positive correlation between the geoid and density anomalies can be achieved, with the same viscosities as in the initial model, by decreasing LVC thickness to the range of $170 \text{ km} < h_{LVC} < 280 \text{ km}$ (bold line in Figure C2d; these calculations and the ones below included the negligibly small contribution from a 40-km thick elastic lithosphere). In this model, η_{LVC} is 2.5 orders of magnitudes smaller than the viscosity of the lower mantle implying a reasonable asthenospheric viscosity of $\eta_{LVC} \approx 3.2 \times 10^{19}$ for a lower-mantle viscosity of 10^{22} Pa·s. When η_{LVC} is allowed to vary, a range of allowable viscosities and thicknesses is obtained (Figure C2d). An alternative viscosity model, which fits the observation but does not include the sharp viscosity jump in the middle of the upper mantle, can be obtained by decreasing the viscosity of the asthenosphere by less than a factor of 2 and by placing a gradational viscosity increase from the LVC to the reference viscosity at 400 km depth (Figure C3a). This viscosity structure, which mimics the seismic structure of PA5 (Figure 2), is more plausible for a mantle viscosity that is pressure and temperature dependent. Figure C3d provides some plausible bounds for h_{LVC} and η_{LVC} for models of this type.

As a final comment on these dynamic compensation models, we note that the effect of the 410 and 660 discontinuity topographies on the geoid can be very significant at low harmonic degrees [Thoraval *et al.*, 1995]. This effect is smaller, however, around the harmonic degree of our analysis ($l = 26$), because the geoid kernels at both depths are quite small, especially around the 660 discontinuity (see Figures C1b, C2b, and C3b). Moreover, the 410 and the 660 discontinuities are anticorrelated in the TH2 model, whereas the sign of the geoid kernels is the same at both depths;

therefore the combined contribution from the two discontinuities tends to cancel. For the viscosity structure of Figure C2a, for example, the density contrast associated with the deflection of the two discontinuities can explain only about 7% of the geoid at $l = 26$.

Although these thermal convection models can explain the seismic results and the geoid anomalies observed along the Tonga-Hawaii corridor, they fail to predict the positive topography of the swells above the high-velocity, "cold" regions. These models will always predict negative dynamic topography over the cold downwelling (note that the surface topography kernels are negative at all depths, e.g., Figures C1c, C2c, and C3c). Therefore we are forced to incorporate a shallow source of buoyancy with high seismic velocities beneath the swells to explain the observations. Compositional inhomogeneities associated with basaltic volcanism seem to provide the necessary mechanism.

Acknowledgments. We thank J. Gaherty for his help throughout the course of this study, B. Hager and L. Panasyuk for providing the software for the dynamic compensation calculations, and J. Revenaugh for his ray-tracing code. We also thank A. Cazenave for sending us her new high-resolution sea surface map; G. Ekström, Y. Wang, and M. Flanagan for making their preprints available to us; and P. Shearer, H.-C. Nataf, and an anonymous reviewer for helpful reviews. We acknowledge the IRIS-DMC for the seismological data and Harvard for their CMT solutions. Some of the figures were generated using the GMT software freely distributed by *Wessel and Smith* [1991]. This research was supported by the National Science Foundation under grant EAR-9628351.

References

- Backus, G. E., and F. Gilbert, Numerical application of a formalism for geophysical inverse problems, *Geophys. J. R. Astron. Soc.*, **13**, 247–276, 1967.
- Baudry, N., and L. Kroenke, Intermediate-wavelength (400–600 km), south Pacific geoidal undulations: Their relationship to linear volcanic chains, *Earth Planet. Sci. Lett.*, **102**, 430–443, 1991.
- Bina, C., and G. Helffrich, Phase transition Clapeyron slopes and transition zone seismic discontinuity topography, *J. Geophys. Res.*, **99**, 15,853–15,860, 1994.
- Butler, R., The 1973 Hawaii earthquake: A double earthquake beneath the volcano Mauna Kea, *Geophys. J. R. Astron. Soc.*, **69**, 173–186, 1982.
- Calmant, S., The elastic thickness of the lithosphere in the Pacific Ocean, *Earth Planet. Sci. Lett.*, **85**, 277–288, 1987.
- Cara, M., and J. J. Lévesque, Anisotropy of the asthenosphere: The higher mode data of the Pacific revisited, *Geophys. Res. Lett.*, **15**, 205–208, 1988.
- Cazenave, A., S. Houry, and K. Dominh, Geosat-derived geoid anomalies at medium wavelengths, *J. Geophys. Res.*, **97**, 7081–7095, 1992.
- Cazenave, A., B. Parsons, and P. Calcagno, Geoid lineations of 1000 km wavelength over the central Pacific, *Geophys. Res. Lett.*, **22**, 97–100, 1995.
- Cazenave, A., P. Schaeffer, M. Berge, C. Brossier, K. Dominh, and M. C. Gennero, High-resolution mean sea surface computed with data of ERS-1 (geodetic mission) and the TOPEX-POSEIDON, *Geophys. J. Int.*, **125**, 696–704, 1996.
- Červený, V., and J. E. P. Soares, Fresnel volume ray tracing, *Geophysics*, **57**, 902–915, 1992.
- Creager, K. C., and T. H. Jordan, Slab penetration into the lower mantle beneath the Mariana and other island arcs of the northwest Pacific, *J. Geophys. Res.*, **91**, 3573–3589, 1986.
- Crough, S. T., Hotspot swells, *Annu. Rev. Earth Planet. Sci.*, **11**, 165–193, 1983.
- Crough, S. T., and R. D. Jarrard, The Marquesas-Line swell, *J. Geophys. Res.*, **86**, 11,763–11,771, 1981.
- Davies, G. F., and F. Pribac, Mesozoic seafloor subsidence and the Darwin Rise, past and present, in *The Mesozoic Pacific: Geology, Tectonics, and Volcanism*, *Geophys. Monogr., Ser.*, vol. 77, edited by M. S. Pringle et al., pp. 39–52, AGU, Washington, D.C., 1993.
- Detrick, R. S., and S. T. Crough, Island subsidence, hot spots, and lithospheric thinning, *J. Geophys. Res.*, **83**, 1236–1244, 1978.
- Dziewonski, A. M., and D. L. Anderson, Preliminary reference Earth model, *Phys. Earth Planet. Inter.*, **25**, 297–356, 1981.
- Dziewonski, A. M., G. A. Ekström, and X.-F. Liu, Structure at the top and bottom of the mantle, in *Monitoring a Comprehensive Test Ban Treaty*, edited by E. S. Husebye and A. M. Dainty, pp. 521–550, Kluwer Acad., Norwell, Mass., 1996.
- Ekström, G. A., and A. M. Dziewonski, The unique anisotropy of the Pacific upper mantle, *Nature*, in press, 1998.
- Fischer, K. M., K. C. Creager, and T. H. Jordan, Mapping the Tonga slab, *J. Geophys. Res.*, **96**, 14,403–14,427, 1991.
- Flanagan, M. P., and P. M. Shearer, Global mapping of topography on transition zone velocity discontinuities by stacking SS precursors, *J. Geophys. Res.*, **103**, 2673–2692, 1998.
- Forsyth, D. W., The early structural evolution and anisotropy of the oceanic upper mantle, *Geophys. J. R. Astron. Soc.*, **43**, 103–162, 1975.
- Forte, A. M., A. M. Dziewonski, and R. L. Woodward, Aspherical structure of the mantle, tectonic plate motions, nonhydrostatic geoid, and topography of the core-mantle boundary, in *Dynamics of Earth's Deep Interior and Earth Rotation*, *Geophys. Monogr. Ser.*, vol. 72, edited by J.-L. Le Mouél, D. E. Smylie, and T. Herring, pp. 135–166, 1993.
- Gaherty, J. B., and T. H. Jordan, Lehmann discontinuity as the base of an anisotropic layer beneath continents, *Science*, **268**, 1468–1471, 1995.
- Gaherty, J. B., T. H. Jordan, and L. S. Gee, Seismic structure of the upper mantle in a western Pacific corridor, *J. Geophys. Res.*, **101**, 22,291–22,309, 1996.
- Garnero, E. J., and D. V. Helmberger, Seismic detection of a thin laterally varying layer at the base of the mantle beneath the central-Pacific, *Geophys. Res. Lett.*, **23**, 977–980, 1996.
- Gee, L. S., and T. H. Jordan, Generalized seismological data functionals, *Geophys. J. Int.*, **111**, 363–390, 1992.
- Gee, L. S., and B. Romanowicz, Attenuation and differential travel times in the western Pacific, *Eos, Trans. AGU*, **73**(43), Fall Meet. Suppl., 384, 1992.
- Gilbert, F., and D. V. Helmberger, Generalized ray theory for a layered sphere, *Philos. Trans. R. Soc. London, Ser. A*, **278**, 187–269, 1972.
- Grand, S. P., Tomographic inversion for shear velocity beneath the North American plate, *J. Geophys. Res.*, **92**, 14,065–14,090, 1987.
- Grand, S. P., Mantle shear structure beneath the Americas and surrounding oceans, *J. Geophys. Res.*, **99**, 11,591–11,621, 1994.
- Grand, S. P., and D. V. Helmberger, Upper mantle shear structure of North America, *Geophys. J. R. Astron. Soc.*, **76**, 399–438, 1984.
- Grand, S. P., R. van der Hilst, and S. Widiyantoro, Global seismic tomography: A snapshot of convection in the Earth, *GSA Today*, **7**, 1–7, 1997.
- Green, D. H., and R. C. Liberman, Phase equilibria and elastic properties of a pyrolite model for the oceanic upper mantle, *Tectonophysics*, **32**, 61–92, 1976.
- Gripp, A. E., and R. G. Gordon, Current plate velocities relative to the hotspots incorporating the NUVEL-1 global plate motion model, *Geophys. Res. Lett.*, **17**, 1109–1112, 1990.
- Hager, B. H., Subducted slabs and the geoid: Constraints on mantle rheology and flow, *J. Geophys. Res.*, **89**, 6003–6015, 1984.
- Hager, B. H., Mantle viscosity: A comparison of models from postglacial rebound and from geoid, plate driving forces, and advected heat flux, in *Glacial Isostasy, Sea Level and Mantle Rheology*, edited by R. Sabadini, K. Lambeck, and E. Boschi, pp. 493–513, Kluwer Acad., Norwell, Mass., 1991.
- Hager, B. H., and R. W. Clayton, Constraints on the structure of mantle convection using seismic observations, flow models, and the geoid, in *Mantle Convection: Plate Tectonics and Global Dynamics*, edited by W. R. Peltier, pp. 658–763, Gordon and Breach, Newark, N.J., 1989.

- Hager, B. H., and M. A. Richards, Long-wavelength variations in Earth's geoid: Physical models and dynamical implications, *Philos. Trans. R. Soc. London, Ser. A*, 328, 309–327, 1989.
- Haxby, W. F., and J. K. Weissel, Evidence for small-scale mantle convection from Seasat altimeter data, *J. Geophys. Res.*, 91, 3507–3520, 1986.
- HelMBERGER, D. V., Theory and application of synthetic seismograms, in *Earthquakes: Observation, Theory, and Interpretation*, edited by H. Kanamori and E. Boschi, pp. 174–217, North-Holland, New York, 1983.
- HelMBERGER, D. V., and R. A. Wiggins, Upper-mantle structure of midwestern United States, *J. Geophys. Res.*, 76, 3229–3245, 1971.
- Honda, S., D. A. Yuen, S. Balachandrar, and D. Reuteler, Three-dimensional instabilities of mantle convection with multiple phase transition, *Science*, 259, 1308–1311, 1993.
- Hong, T.-L., and D. V. HelMBERGER, Glorified optics and wave propagation in nonplanar structure, *Bull. Seismol. Soc. Am.*, 68, 1313–1358, 1978.
- Houseman, G., and D. P. McKenzie, Numerical experiments on the onset of convective instabilities in the Earth's mantle, *Geophys. J. R. Astron. Soc.*, 68, 133–164, 1982.
- Hron, F., Criteria for selection of phases in synthetic seismograms for layered media, *Bull. Seismol. Soc. Am.*, 61, 765–779, 1971.
- Hron, F., Numerical method for ray generation in multilayered media, *Methods Comput. Phys.*, 12, 1–34, 1972.
- Jordan, T. H., Mineralogies, densities and seismic velocities of garnet lherzolites and their geophysical implications, in *Mantle Sample: Inclusions in Kimberlites and Other Volcanics*, edited by F. R. Boyd and H. O. A. Meyer, pp. 1–13, AGU, Washington, D.C., 1979.
- Jordan, T. H., and S. A. Sipkin, Estimation of the attenuation operator for multiple ScS waves, *Geophys. Res. Lett.*, 4, 167–170, 1977.
- Karato, S., Importance of anelasticity in the interpretation of seismic tomography, *Geophys. Res. Lett.*, 20, 1623–1626, 1993.
- Karato, S.-I., Effects of water on seismic wave velocities in the upper mantle, *Proc. Jpn. Acad., Ser. B*, 71, 61–66, 1995.
- Kato, M., An analysis of the temperature derivative of shear-wave velocity in the oceanic lithosphere of the Pacific Basin, *J. Phys. Earth*, 45, 67–71, 1997.
- Katzman, R., L. Zhao, and T. H. Jordan, Image of small-scale convection in the Pacific upper mantle: Implications for the Hawaii, Marquesas and Society hotspots, *Eos Trans. AGU*, 78(17), Spring Meet. Suppl., S322, 1997.
- Kawasaki, I., and F. Kon'no, Azimuthal anisotropy of surface waves and the possible type of the seismic anisotropy due to preferred orientation of olivine in the uppermost mantle beneath the Pacific Ocean, *J. Phys. Earth*, 32, 229–244, 1984.
- Lay, T., and T. C. Wallace, Multiple ScS travel times and attenuation beneath Mexico and Central America, *Geophys. Res. Lett.*, 10, 301–304, 1983.
- Lemoine, F. G., et al., The NASA and DMA Joint Geopotential Model, *Eos Trans. AGU*, 77(46), Fall Meet. Suppl., F136, 1996.
- Lerner-Lam, A., and T. H. Jordan, Earth structure from fundamental and higher-mode waveform analysis, *Geophys. J. R. Astron. Soc.*, 75, 759–797, 1983.
- Li, X.-D., and B. Romanowicz, Comparison of global waveform inversions with and without considering cross-branch model coupling, *Geophys. J. Int.*, 121, 695–709, 1995.
- Li, X.-D., and B. Romanowicz, Global mantle shear velocity model developed using nonlinear asymptotic coupling theory, *J. Geophys. Res.*, 101, 22,245–22,272, 1996.
- Li, X.-D., and T. Tanimoto, Waveforms of long-period waves in a slightly aspherical earth model, *Geophys. J. Int.*, 112, 92–102, 1993.
- Liu, M., and C. G. Chase, Evolution of Hawaiian basalts: A hotspot melting model, *Earth Planet. Sci. Lett.*, 104, 151–165, 1991.
- Machetel, P., and P. Weber, Intermittent layered convection in a model mantle with an endothermic phase change at 670 km, *Nature*, 350, 55–57, 1991.
- Maia, M., and M. Diament, An analysis of the altimetric geoid in various wavebands in the central Pacific Ocean: Constraints on the origin of intraplate features, *Tectonophysics*, 190, 133–153, 1991.
- Marquering, H., and R. Snieder, Surface-wave mode coupling for efficient forward modeling and inversion of body-wave phases, *Geophys. J. Int.*, 120, 186–208, 1995.
- Marquering, H., R. Snieder, and G. Nolet, Waveform inversions and the significance of surface-wave mode coupling, *Geophys. J. Int.*, 124, 258–278, 1996.
- Masters, G., S. Johnson, G. Laske, and H. Bolton, A shear velocity model of the mantle, *Philos. Trans. R. Soc. London, Ser. A*, 354, 1385–1411, 1996.
- Maupin, V., Partial derivatives of surface-wave phase velocities for flat anisotropic models, *Geophys. J. R. Astron. Soc.*, 83, 379–398, 1985.
- McKenzie, D., A. Watts, B. Parsons, and M. Roufousse, Platform of mantle convection beneath the Pacific Ocean, *Nature*, 288, 442–446, 1980.
- Menard, H. W., Darwin reprise, *J. Geophys. Res.*, 89, 9960–9968, 1984.
- Montagner, J.-P., and T. Tanimoto, Global upper mantle tomography of seismic velocities and anisotropy, *J. Geophys. Res.*, 96, 20,337–20,351, 1991.
- Morgan, W. J., Deep mantle convection plumes and plate motion, *Am. Assoc. Pet. Geol. Bull.*, 56, 203–213, 1972.
- Mueller, R. D., W. R. Roest, J.-Y. Royer, L. M. Gahagan, and J. G. Sclater, A digital age map of the ocean floor, *SIO Ref. Ser.*, 93–30, 1993.
- Nakanishi, I., Attenuation of multiple ScS beneath the Japanese arc, *Phys. Earth. Planet. Inter.*, 19, 337–347, 1979.
- Nicolas, A., and N. I. Christensen, Formation of anisotropy in upper mantle peridotites: A review, in *Composition, Structure, and Dynamics of Lithosphere-Asthenosphere System*, *Geodyn. Ser.*, vol. 16, edited by K. Fuchs and C. Froidevaux, pp. 111–123, AGU, Washington, D.C., 1987.
- Nishimura, C. E., and D. W. Forsyth, The anisotropic structure of the upper mantle in the Pacific, *Geophys. J. Int.*, 96, 203–229, 1989.
- Nolet, G., Partitioned waveform inversion and two-dimensional structure under the network of autonomously recording seismographs, *J. Geophys. Res.*, 95, 8499–8512, 1990.
- Nolet, G., S. P. Grand, and B. L. N. Kennett, Seismic heterogeneity in the upper mantle, *J. Geophys. Res.*, 99, 23,753–23,766, 1994.
- O'Hara, M. J., Is there an Icelandic mantle plume?, *Nature*, 253, 708–710, 1975.
- Panasjuk, S. V., B. H. Hager, and A. M. Forte, Understanding the effects of mantle compressibility on geoid kernels, *Geophys. J. Int.*, 124, 121–133, 1996.
- Parsons, B., and D. McKenzie, Mantle convection and the thermal structure of the plates, *J. Geophys. Res.*, 83, 4485–4496, 1978.
- Pavlis, G. L., and J. R. Booker, The mixed discrete-continuous inverse problem: Application to the simultaneous determination of earthquake hypocenters and velocity structure, *J. Geophys. Res.*, 85, 4801–4810, 1980.
- Phipps Morgan, J., and P. Shearer, Seismic constraints on mantle flow and topography of the 660-km discontinuity: Evidence for whole mantle convection, *Nature*, 365, 506–511, 1993.
- Phipps Morgan, J., W. J. Morgan, and E. Price, Hotspots melting generates both hotspot volcanism and hotspot swell, *J. Geophys. Res.*, 100, 8045–8062, 1995.
- Puster, P., and T. H. Jordan, How stratified is mantle convection?, *J. Geophys. Res.*, 102, 7625–7646, 1997.
- Puster, P., J. B. Gaherty, T. H. Jordan, and D. J. Weidner, Fine-scale structure of the 660-km discontinuity region, *Eos Trans. AGU*, 77(46), Fall Meet. Suppl., F472, 1996.
- Regan, J., and D. L. Anderson, Anisotropy models of the upper mantle, *Phys. Earth Planet. Inter.*, 35, 227–263, 1984.
- Revenaugh, J., and T. H. Jordan, Observations of first-order mantle reverberations, *Bull. Seism. Soc. Am.*, 77, 1704–1717, 1987.
- Revenaugh, J., and T. H. Jordan, A study of mantle layering beneath the western Pacific, *J. Geophys. Res.*, 94, 5787–5813, 1989.
- Revenaugh, J., and T. H. Jordan, Mantle layering from ScS reverberations, 1, Waveform inversion of zeroth-order reverberations, *J. Geophys. Res.*, 96, 19,749–19,762, 1991a.
- Revenaugh, J., and T. H. Jordan, Mantle layering from ScS

- reverberations, 2, The transition zone, *J. Geophys. Res.*, *96*, 19,763–19,780, 1991b.
- Revenaugh, J., and T. H. Jordan, Mantle layering from ScS reverberations, 3, The upper mantle, *J. Geophys. Res.*, *96*, 19,781–19,810, 1991c.
- Revenaugh, J., and T. H. Jordan, Mantle layering from ScS reverberations, 4, The lower mantle and core-mantle boundary, *J. Geophys. Res.*, *96*, 19,781–19,810, 1991d.
- Revenaugh, J., and S. A. Sipkin, Mantle discontinuity structure beneath China, *J. Geophys. Res.*, *99*, 21,911–21,927, 1994a.
- Revenaugh, J., and S. A. Sipkin, Seismic evidence for silicate melt atop the 410-km mantle discontinuity, *Nature*, *369*, 474–476, 1994b.
- Ribe, M. N., Seismic anisotropy and mantle flow, *J. Geophys. Res.*, *94*, 4213–4223, 1989.
- Richards, M. A., B. H. Hager, and N. H. Sleep, Dynamically supported geoid highs over hotspots: Observation and theory, *J. Geophys. Res.*, *93*, 7690–7708, 1988.
- Richter, F., Convection and large-scale circulation of the mantle, *J. Geophys. Res.*, *78*, 8735–8745, 1973.
- Richter, F., Focal mechanism and seismic energy release of deep and intermediate earthquakes in the Tonga-Kermadec region and their bearing on the depth extent of mantle flow, *J. Geophys. Res.*, *84*, 6783–6795, 1979.
- Richter, F., and B. Parsons, On the interaction of two scales of convection in the mantle, *J. Geophys. Res.*, *80*, 2529–2541, 1975.
- Ringwood, A. E., *Composition and Petrology of the Earth's Mantle*, 604 pp., McGraw-Hill, New York, 1975.
- Robinson, E. M., B. Parsons, and S. F. Daly, The effect of a shallow low viscosity zone on the apparent compensation of mid-plate swells, *Earth Planet. Sci. Lett.*, *82*, 335–348, 1987.
- Sammis, C. G., J. C. Smith, G. Schubert, and D. A. Yuen, Viscosity-depth profile of the Earth's mantle: Effects of polymorphic phase transition, *J. Geophys. Res.*, *82*, 3747–3761, 1977.
- Sandwell, D. T., and M. Renkin, Compensation of swells and plateaus in the North Pacific: No direct evidence for mantle convection, *J. Geophys. Res.*, *93*, 2775–2783, 1988.
- Sato, H., I. S. Sacks, and T. Murase, The use of laboratory velocity for estimating temperature and partial melt fraction in the low-velocity zone: Comparison with heat flow and electrical conductivity studies, *J. Geophys. Res.*, *94*, 5689–5704, 1989.
- Shearer, P. M., Constraints on upper mantle discontinuities from observations of long-period reflected and converted phases, *J. Geophys. Res.*, *96*, 20,353–20,364, 1991.
- Shearer, P. M., Global mapping of upper mantle reflectors from long-period SS precursors, *Geophys. J. Int.*, *115*, 878–904, 1993.
- Silver, P. G., Seismic anisotropy beneath continents: Probing the depths of geology, *Annu. Rev. Earth Planet. Sci.*, *24*, 385–432, 1996.
- Sipkin, S. A., and T. H. Jordan, Lateral heterogeneity of upper mantle determined from the travel times of multiple ScS, *J. Geophys. Res.*, *81*, 6307–6320, 1976.
- Sipkin, S. A., and T. H. Jordan, Frequency dependence of Q_{ScS} , *Bull. Seismol. Soc. Am.*, *69*, 1055–1079, 1979.
- Sipkin, S. A., and T. H. Jordan, Multiple ScS travel times in the western Pacific: Implications for mantle heterogeneity, *J. Geophys. Res.*, *85*, 853–861, 1980a.
- Sipkin, S. A., and T. H. Jordan, Regional variation of Q_{ScS} , *Bull. Seismol. Soc. Am.*, *70*, 1071–1102, 1980b.
- Solheim, L. P., and W. R. Peltier, Avalanche effects in phase transition modulated thermal convection: A model of Earth's mantle, *J. Geophys. Res.*, *99*, 6997–7018, 1994.
- Spencer, C., and D. Gubbins, Travel-time inversion for simultaneous earthquake location and velocity structure determination in laterally varying media, *Geophys. J. R. Astron. Soc.*, *63*, 95–116, 1980.
- Su, W.-J., R. L. Woodward, and A. M. Dziewonski, Degree 12 model of shear velocity heterogeneity in the mantle, *J. Geophys. Res.*, *99*, 6945–6980, 1994.
- Tackley, P. J., D. J. Stevenson, G. A. Glatzmair, and G. Schubert, Effect of an endothermic phase transition at 670 km depth in spherical model of convection in the Earth mantle, *Nature*, *361*, 699–703, 1993.
- Tanimoto, T., and D. L. Anderson, Lateral heterogeneity and azimuthal anisotropy in the upper mantle: Love and Rayleigh waves 100–250 s, *J. Geophys. Res.*, *90*, 1842–1858, 1985.
- Tarantola, A., *Inverse Problems Theory*, 613 pp., Elsevier, New York, 1987.
- Tarantola, A., and A. Necessian, Three-dimensional inversion without blocks, *Geophys. J. R. Astron. Soc.*, *76*, 299–306, 1984.
- Tarantola, A., and B. Valette, Generalized nonlinear inverse problem solved using the least squares criterion, *Rev. Geophys.*, *20*, 219–232, 1982.
- Thatcher, W., and J. N. Brune, Higher mode interference and observed anomalous apparent Love wave phase velocities, *J. Geophys. Res.*, *74*, 6603–6611, 1969.
- Thoraval, C., P. Machellet, and A. Cazenave, Locally layered convection inferred from dynamic models of the Earth's mantle, *Nature*, *375*, 777–780, 1995.
- Turcotte, D. L., and G. Schubert, *Geodynamics, Applications of Continental Physics to Geological Problems*, 450 pp., John Wiley, New York, 1982.
- van der Hilst, R., Complex morphology of subducted lithosphere in the mantle beneath the Tonga trench, *Nature*, *374*, 154–157, 1995.
- van der Hilst, R., S. Widiyantoro, and E. R. Engdahl, Evidence for deep mantle circulation from global tomography, *Nature*, *386*, 578–584, 1997.
- van der Lee, S., and G. Nolet, The upper-mantle S velocity structure of North America, *J. Geophys. Res.*, *102*, 22,815–22,838, 1997.
- Vasco, D. W., J. John, E. Peterson, and E. L. Majer, Beyond ray tomography: Wavepath and Fresnel volumes, *Geophysics*, *60*, 1790–1804, 1995.
- Von Herzen, R. P., M. J. Cordery, R. S. Detrick, and C. Fang, Heat flow and thermal origin of hotspot swells: The Hawaiian swell revisited, *J. Geophys. Res.*, *94*, 13,783–13,799, 1989.
- Watts, A. B., Gravity and bathymetry in the central Pacific Ocean, *J. Geophys. Res.*, *81*, 1533–1553, 1976.
- Watts, A. B., and U. S. ten Brink, Crustal structure, flexure, and subsidence history of the Hawaiian swell, *J. Geophys. Res.*, *94*, 10,473–10,500, 1989.
- Watts, A. B., J. H. Bodine, and N. M. Ribe, Observations of flexure and the geological evolution of the Pacific Ocean, *Nature*, *283*, 532–537, 1980.
- Weidner, D. J., and Y. Wang, Chemical and Clapeyron induced buoyancy at the 660-km discontinuity, *J. Geophys. Res.*, in press, 1998.
- Wessel, P., and W. H. F. Smith, Free software helps map and display data, *Eos Trans. AGU*, *72*, 441, 445–446, 1991.
- Wessel, P., D. Bercovici, and L. W. Kroenke, The possible reflection of mantle discontinuities in Pacific geoid and bathymetry, *Geophys. Res. Lett.*, *21*, 1943–1946, 1994.
- Woodhouse, J. H., The coupling and attenuation of nearly resonant multiplets in the Earth's free oscillation spectrum, *Geophys. J. R. Astron. Soc.*, *61*, 261–283, 1980.
- Woodhouse, J. H., The joint inversion of seismic waveforms for lateral variations in Earth structure and earthquake source parameters, *Proc. Int. Sch. Phys. Enrico Fermi*, *85*, 366–397, 1983.
- Woodhouse, J. H., and A. M. Dziewonski, Mapping the upper mantle: Three-dimensional modeling of Earth structure by inversion of seismic waves, *J. Geophys. Res.*, *89*, 5953–5986, 1984.
- Woods, M. T., and E. A. Okal, Rayleigh-wave dispersion along the Hawaiian swell: A test of lithospheric thinning by thermal rejuvenation, *Geophys. J. Int.*, *125*, 325–339, 1996.
- Woods, M. T., E. A. Okal, and M. Cara, Two-station measurements of Rayleigh wave group velocity along the Hawaiian swell, *Geophys. Res. Lett.*, *18*, 105–108, 1991.
- Wyssession, M. E., Large-scale structure at the core-mantle boundary from diffracted waves, *Nature*, *382*, 244–248, 1996.
- Zhang, S., and S.-I. Karato, Lattice preferred orientation of olivine aggregates deformed in simple shear, *Nature*, *375*, 774–777, 1995.
- Zhang, Y.-S., and T. Tanimoto, Three-dimensional modeling of upper mantle structure under the Pacific ocean and surrounding area, *Geophys. J. R. Astron. Soc.*, *98*, 255–269, 1989.
- Zhao, L., and T. H. Jordan, Sensitivity of frequency-dependent travel

- times to laterally-heterogeneous, anisotropic Earth structure, *Geophys. J. Int.*, 133, 683-704, 1998.
- Zielhuis, A., and G. Nolet, Shear-wave velocity variations in the upper mantle beneath central Europe, *Geophys. J. Int.*, 117, 695-715, 1994.
- Zielhuis, A., and R. van der Hilst, Upper-mantle shear velocity beneath eastern Australia from inversion of waveform SKIPPY portable arrays, *Geophys. J. Int.*, 127, 1-16, 1996.

T.H. Jordan, R. Katzman, and L. Zhao, Department of Earth, Atmospheric and Planetary Sciences, Massachusetts Institute of Technology, Cambridge, MA02139. (e-mail: thj@mit.edu; rafi@quake.mit.edu; li@caustic.mit.edu)

(Received September 11, 1997; revised December 30, 1997; accepted January 16, 1998.)